Validation of the MOPITT-A Instrument Through Radiative Transfer Modelling and Laboratory Calibration

A Thesis
Submitted to the Faculty of Graduate Studies and Research
in Partial Fulfillment of the Requirements
for the Degree of
Master of Science
in the Department of Physics and Engineering Physics

by
Kirk D.W. Lamont
Saskatoon, Saskatchewan

In presenting this thesis in partial fulfillment of the requirements for a Postgraduate degree from the University of Saskatchewan, the author agrees that the Libraries of this University may make it freely available for inspection. The author further agrees that permission for copying of this thesis in any manner, in whole or in part, for scholarly purposes may be granted by the professor who supervised this thesis work or, in his absence, by the Head of the Department or the Dean of the College in which this thesis work was done. It is understood that any copying or publication or use of this thesis or parts thereof for financial gain shall not be allowed without written approval from the author. It is also understood that due recognition shall be given to the author and to the University of Saskatchewan in any scholarly use which may be made of any material in this thesis.

Requests for permission to copy or to make other use of material in this thesis in whole or in part should be addressed to:

Head of the Department of Physics and Engineering Physics
116 Science Place
University of Saskatchewan
Saskatoon, Saskatchewan
Canada
S7N 5E2

To my wife and daughter, Kari and Klaire

Abstract

This thesis presents the characterization and calibration of the MOPITT-A instrument which uses the technique of correlation spectroscopy to measure carbon monoxide in the atmosphere. A theoretical model is developed for the instrument and compared to MOPITT-A measurements collected under controlled laboratory conditions, which were designed to emulate atmospheric signals. It is shown that the model and measurements are in very good agreement with each other and that the MOPITT-A instrument behaves as expected. It was found that the gain of the instrument varies with time. The cause of the gain variation is not known but it is suggested that frosting inside the detector nest would be consistent with the observed nature of the variation.

Acknowledgements

I would like to express my thanks for the opportunity to work as a member of the Institute of Space and Atmospheric Studies at the University of Saskatchewan. The funding received during my studies was appreciated greatly.

I would like to express my thanks to members of the Institute: Adam Bourassa and Truitt Wiensz. They were amazing individuals to work alongside and never hesitated in helping with a problem. Their helpful comments and conversations were invaluable throughout this process. I would like to thank Dr. Ted Llewellyn for his support through my time as a member of the Institute, as he never failed to lend an ear when needed. A special thanks to Dr. Nick Lloyd for his help from beginning to end of my work. Whether it was in the laboratory or in the office he was always willing to offer support and help. Nick's dedication to MOPITT-A is very appreciated. Tremendous thanks must be given to my supervisor, Dr. Doug Degenstein, for allowing me the opportunity to further my education through this wonderful experience. His unwavering support of this project over the years was amazing. His dedication to his students is second to none.

Finally, I wish to thank my family, especially my wife Kari and my daughter Klaire, for their unwavering support over the years.

Contents

List of Figures

Glossary of Terms

anthropogenic	Effects or processes derived from human activities.
B	The Planck function.
biogenic	A substance produced by a natural life process such as secretion from plants or animals.
c_2	A HITRAN constant which is equal to 1.4388 cmK.
CaF_2	Calcium flouride.
CH_4	Methane.
CO	Carbon monoxide.
CO_2	Carbon dioxide.
D	The Difference signal used in correlation spectroscopy found by subtracting the Low and High signals.
δ	The air broadened pressure shift.
DN	Digital number.
E_{kl}	Represents the upper and lower transitional energy states of a molecule.
ENSO	El Niño Southern Oscillation.
f	The MOPITT-A detector filter shape.
f(ν,T,p)	The collision broadened line shape.
F_D	The instrument difference filter, found through subtraction of the Short Filter and the Long Filter.

F_L	This represents the instrument filter when the LMC is in a pathlong state.
F_S	This represents the instrument filter when the LMC is in a pathshort state.
g	The lower state statistical weight used to calculate the partition ratio.
γ	The collision broadening coefficient.
γ_{air}	The air broadened spectral line halfwidths.
γ_{self}	The self broadened spectral line halfwidths.
h	Planck's constant.
HITRAN	HIgh-resolution TRANsmission.
Hg	Mercury.
I	The intensity found at any particular location.
InSb	Indium antimonide.
ISAS	Institute for Space and Atmospheric Studies.
k	The gain of any MOPITT-A detector pixel.
L	The Long signal used in correlation spectroscopy found by subtracting L_O and L_C.
L_C	This represents the instrument state when the onboard chopper is closed and the LMC is in a pathlong state.
L_O	This represents the instrument state when the onboard chopper is open and the LMC is in a pathlong state.
LMC	The onboard instrument gas-cell called the length modulated cell.
LN_2	Liquid Nitrogen.
MOPITT-A	Measurement Of Pollution In The Troposphere - Aircraft.
MSIS-E-90	Mass Spectrometer Incoherent Scatter.
n	The molecular density.

N_2	Nitrogen gas.
ν	Represents a wavenumber in a molecular spectrum.
O	Data measured by MOPITT-A refereed to as the observed or measured data.
O_3	Ozone.
OH	Hydroxyl.
P	Represents the probability of a photon interacting with a molecule over some differential path.
p	Represents the atmospheric or laboratory pressure of a gas of interest.
pathlong	The LMC state when the rotor is out of the optical path resulting in the longest possible path length.
pathshort	The LMC state when the rotor is in the optical path resulting in the shortest possible path length.
ϕ	The instrument response.
pyrogenic	Effects or processes produced under conditions involving intense heat.
Q	The partition ratio.
R	The reflectivity of a black body.
R^2	The coefficient of determination.
S	The Short signal used in correlation spectroscopy found by subtracting S_O and S_C.
S_C	This represents the instrument state when the onboard chopper is closed and the LMC is in a pathshort state.
S_O	This represents the instrument state when the onboard chopper is open and the LMC is in a pathshort state.
S	The spectral line intensity.

SAFARI-2000	Southern African Regional Science Initiative that took place in the year 2000.
σ	The apparent cross sectional area of a molecule.
stratosphere	The layer of Earth's atmosphere between approximately 15 km and 50 km from the surface.
T	The temperature at any given position.
τ	The optical depth.
tropopause	The boundary in Earth's atmosphere that separates the troposphere and the stratosphere.
troposphere	The layer of Earth's atmosphere between the surface and approximately 15 km.

Chapter 1

Introduction

1.1 Atmospheric Pollutants

Atmospheric pollution is an important issue in today's society. With many parts of the world coming together to acknowledge the problem and trying to deal with it by measuring and reducing emissions, it is very important to understand how these emissions act in the atmosphere. One of the first steps in understanding these pollutants is measuring their presence in the atmosphere.

Two of the largest tropospheric pollutants are carbon monoxide (CO) and carbon dioxide (CO_2). They are both by-products of processes such as combustion, biomass burning, and natural vegetation. Carbon monoxide mixes well in the lower atmosphere and therefore is a fairly long lived molecule. As it is produced almost exclusively with carbon dioxide it can act as a tracer of CO_2 production. The properties of CO make it an ideal candidate for measurement to further our understanding of pollution in the lower atmosphere.

1.2 The MOPITT-A Instrument

The Measurement Of Pollution In The Troposphere - Aircraft, MOPITT-A, instrument was built as the Engineering Qualification Model for the satellite based MOPITT instrument. MOPITT-A is a 4 channel instrument built for measuring carbon monoxide and methane in the lower atmosphere of Earth. Each channel consists of a 4 pixel, linear array, indium antimonide (InSb) photo-sensor. The detector measures light at wavelengths in the infrared region of the spectrum.

The measurements collected by MOPITT-A must be validated to ensure that it continues to be an effective measurement tool. Validation experiments were conducted for this instrument in the Optics Laboratory in the Institute for Space and Atmospheric Studies, University of Saskatchewan. This thesis will discuss the optical system, theoretical background and data reduction techniques employed by MOPITT-A.

1.3 Outline

This work will begin with a background on carbon monoxide in the atmosphere. This will be followed by a detailed description of the MOPITT-A internal and external hardware. Information will be given on the construction, specifications, and use of each piece of equipment. In addition, a brief description of several historical MOPITT-A missions is presented.

Radiative transfer theory is discussed in Chapter 3. This chapter will develop the optical transmission properties of single and multiple absorbing layers at infrared wavelengths. Chapter 4 will develop the theory of correlation spectroscopy, as employed by MOPITT-A, and demonstrate how this technique can be used to retrieve concentrations of carbon monoxide in the atmosphere.

Chapter 5 provides a description of the laboratory setup used in the characterization of the MOPITT-A optical system. It will discuss all the equipment used in the laboratory experiments along with the determination of the detector positioning and field-of-view.

A comparison of a theoretical model with controlled laboratory measurements is presented in Chapter 6. This includes discussion of the detector gain, instrument response and atmospheric response. The final chapter of this work discusses the conclusions and the recommendations for future work based on the experimental outcome.

Chapter 2

Background

The majority of the general public know of carbon monoxide as a silent killer, a toxic gas produced as a byproduct of combustion within our furnaces and automobiles. Several hundred people are killed each year in North America from accidental CO poisoning. However, scientific measurements of carbon monoxide within the atmosphere are proving most useful and this simple little molecule is substantially increasing our understanding of tropospheric pollution, tropospheric greenhouse gases and tropospheric dynamics.

Many atmospheric pollutants, including CO, are created at or near the surface of the Earth where they are injected into the lower troposphere. After injection, tropospheric dynamics and convective overturning both move the pollutant around the globe and mix the species with the rest of the troposphere. Short lived pollutants, like anthropogenic tropospheric ozone (O_3) for example, stay close to the source of production while long lived pollutants, CO_2 for example, become thoroughly mixed throughout the atmosphere.

Carbon monoxide falls in between these two limits and has an atmospheric lifetime of approximately three months (Drummond et al., 2003) that is neither short nor long. This is sufficiently long that the distribution of CO will undergo global scale transport effects, but short enough that it does not completely mix. Continuous global measurements of CO permit tracing of dynamical effects within the troposphere as well as detection of tropospheric sources of CO. Carbon monoxide is primarily created through combustion and biomass burning (Houghton, 1992; Holloway, 2000), and is usually accompanied by the creation of CO_2. Hence monitoring the global distribution of CO production sources is a direct proxy for monitoring

worldwide sources of CO_2 production.

Carbon monoxide is removed from the atmosphere through reaction with the hydroxyl (OH) radical,

$$CO + OH \longrightarrow CO_2 + H. \tag{2.1}$$

This is the main sink of atmospheric CO (Houghton, 1992). The hydroxyl radical is an important atmospheric molecule, and is occasionally referred to as the *tropospheric vacuum cleaner* (Thompson, 1992) as it is responsible for cleaning up many atmospheric pollutants. An over-abundance of CO will cause increased destruction of OH and a possible increase in other atmospheric pollutants may occur. Measurements of CO and in particular, CO destruction, provide valuable information about the global distribution of OH, and are particularly useful as direct measurements of OH are extremely difficult due to its inherent high reactivity (Summers et al., 1997).

High concentrations of CO are found in areas of the Earth where combustion and biomass burning are greatest, such as South America and Africa. The MOPITT instrument has gathered information on tropospheric CO for a number of years which has significantly increased our understanding of the creation and transport of CO within the atmosphere. The transport of pollutants emitted by biomass burning over West Africa during spring 2001 was analyzed by Pradier et al. (2006), who utilized CO data from MOPITT. Their results showed that the main source of CO comes from low levels (surface to 80 kPa pressure regions) due to biomass burning (about 18-31%) and inflow (52-55%). They also determined that more than 70% of CO present at these levels is transported upwards and outwards into the free troposphere. Therefore, most CO emitted over Western Africa during these months is transported to the Atlantic through mid tropospheric transport, and east and west through upper tropospheric transport. The western transports are known causes of increase to the South American chemical budget, while the eastern transport adds to the Asian chemical budget.

Edwards et al. (2006), has shown correlation between southern hemisphere annual peak CO loading and the dry season biomass burning in South America, southern Africa, Indonesia and Malaysia, and Australia. This CO loading is then burnt off in later months due to increased photolysis. It is also shown that the largest CO variability in the southern hemisphere is due to fire activity from the maritime areas of Indonesia, Malaysia, etc. and northern Australia. Creation and transport of CO from region to region is shown to be facilitated by the El Niño Southern

Oscillation (ENSO) conditions, when present. Therefore, the southern hemisphere biomass burnings account for the primary source of CO emissions, and a direct link was shown between fires, fire frequency and intensity, vegetation drying and the ENSO. Edwards et al. (2006) has also shown southern hemisphere locations where three large anticyclonic circulations serve as trapping mechanisms for trace gases and aerosols, leading to an observed build up of pollutants. Emissions from South America are shown to exit the continent to the southeast across the Atlantic. Most African emissions were found to transport into the Indian Ocean, where strong plumes were found to transport to Australia in 8-13 days. These emissions are then enhanced by Australian fires before continued transport across the Pacific. It is also shown how this transport of CO in the troposphere impacts the clean atmosphere over New Zealand. MOPITT data was also used to investigate vertical transport of CO over regions of biomass burning, which showed a large increase in the mixing ratio.

Bowman (2006), has used MOPITT data to show seasonal variations in CO levels. Figure 2.1 shows a global picture of CO levels from October of 2002, southern hemisphere spring, and from March of 2003, northern hemisphere spring. Three distinct plumes of CO are seen in South America, Africa, and the maritime continent during the southern hemisphere spring. As time progresses and the northern hemisphere moves to spring the southern hemisphere plumes are no longer visible in the same locations. Also discussed are the levels of CO in the northern hemisphere, and how they are typically higher in the colder season due to low levels of OH. This leads to a longer life time for CO as its destruction through the reaction in equation 2 does not happen as readily.

While MOPITT data have been used to study CO transport from large production regions like Africa, it has also been used to study CO distribution in the northern hemisphere as well. Yurganov et al. (2005) used data from MOPITT to verify northern hemisphere increase in CO abundance in the summer and autumn of 2002 and 2003. It was found that an increase in CO abundance was due, most likely, to strong wild fires. Lamarque et al. (2003) used data from August 2000 to identify regions affected by large forest fires that occurred in Idaho, Montana, and Wyoming, and to model the transport of CO released by these fires. It was found that the CO released by the fires was transported to the northeast coast of Canada, as well as south towards Florida and the Eastern United States. Figure 2.2 shows MOPITT data taken over this time period.

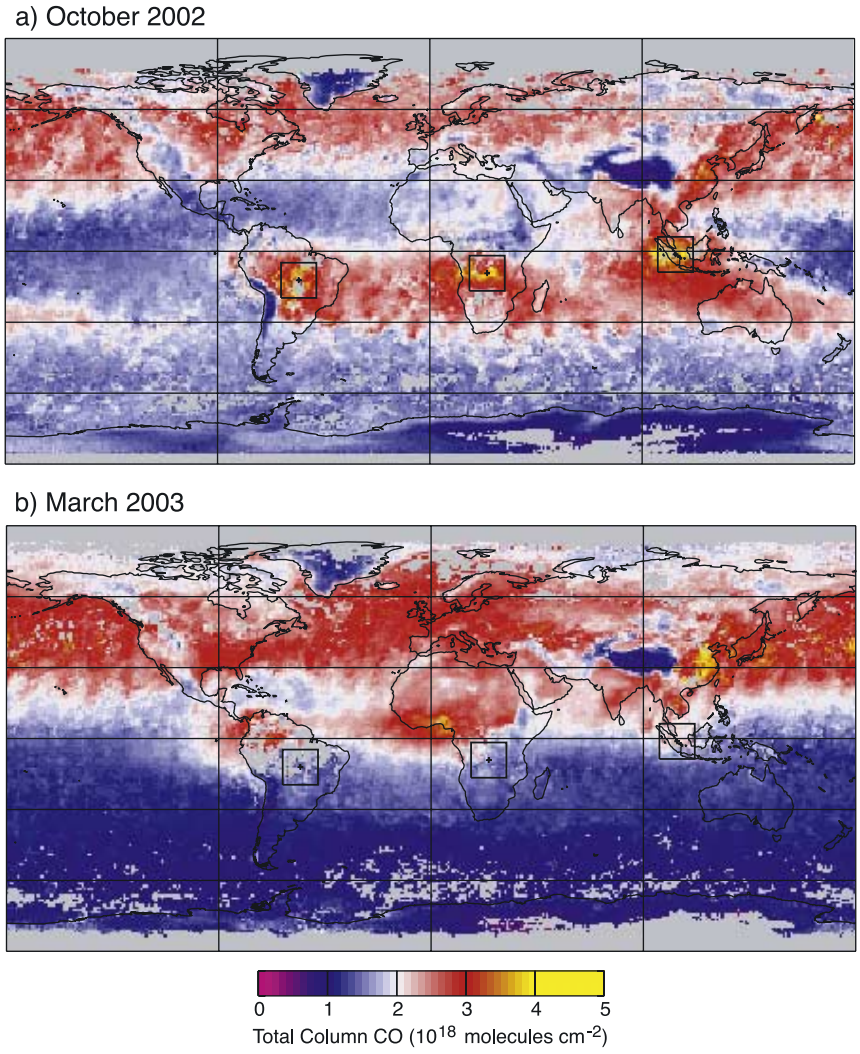

Figure 2.1: Variation in global CO concentrations from Southern Hemisphere spring in 2002 (top) and Northern Hemisphere spring in 2003 (bottom). (Bowman, 2006)

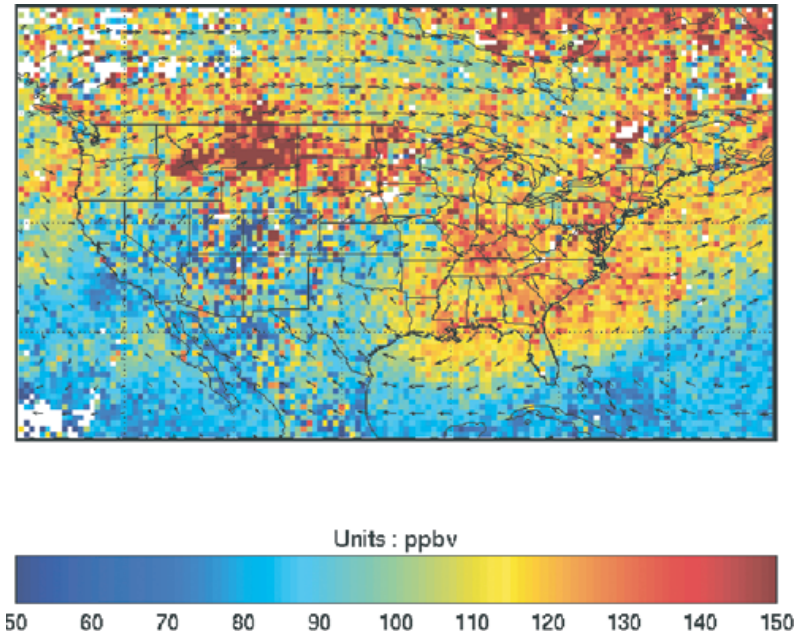

Figure 2.2: Forest fires in Idaho and Montana in August 2000 showing CO emission and transport north east and south east (Lamarque et at., 2003)

Data gathered from the boreal forest area was used to determine temporal profiles of fire events by Hyer et al. (2007). It was found using data from MOPITT, as well as other sources, that atmospheric measurements of high-frequency variability of surface sources are not necessarily sensitive.

The information gathered on the transport and creation of CO by MOPITT is a valuable resource to the understanding of pollution in the atmosphere. Measurements from tropospheric satellite sensors will play an increasingly important role in explaining chemistry and transport processes in the lower atmosphere.

2.1 MOPITT-A

The MOPITT-A instrument was built in 1995 and delivered to the University of Toronto for testing as the Engineering Qualification Model for the MOPITT satellite instrument. It was used to validate that the flight model could supply high quality measurements. The Engineering Qualification Model was built as a 4 channel instrument with a 4 pixel detector array for each channel with the ability to measure both CO and methane (CH_4). Measurements taken with the Engineering Qualification Model allowed changes to be made to the flight model before launch.

In 1997 the Engineering Qualification Model made measurements that were used as a base line comparison for the flight model. Afterwards it was decided to upgrade the Engineering Qualification Model to an aircraft version of the flight model, called MOPITT-A. The necessary changes were made so it could be secured in a special pod attached to a wing of a NASA ER-2 plane.

MOPITT-A has been on one flight mission, known as SAFARI-2000, in Southern Africa. The flight mission was conducted by a science team that included, amongst others, members from the University of Toronto and University of Saskatchewan. The Southern African Fire-Atmosphere Regional Science Initiative (SAFARI-2000) was an international regional science initiative in Southern Africa to study and find linkages between land and atmospheric processes. The relationship of biogenic, pyrogenic and anthropogenic emissions and the consequences they have on Southern Africa were studied. This initiative was part of the Southern Tropical Atlantic Research Experiment (STARE) and was conducted by a number of scientific instruments including MOPITT-A. There were six separate instruments on the ER-2 and three other airborne instruments. This suite of instrumentation measured a range of data, from aerosols and clouds to upward and downward solar flux. Information on the SAFARI-2000 mission is briefly outlined in Andreae et al. (1996).

MOPITT-A collected data during the SAFARI campaign throughout Mozambique, Malawi, South Africa and the coast of the Indian Ocean on various flight paths. These flight paths took MOPITT-A over industrial sites, power plants, and large areas of biomass burning. The data were analyzed at the University of Toronto upon return from the campaign. It was found that the MOPITT-A internal blackbodies, which are used to produce a 3-point calibration, were not properly insulated. This caused a non-linear trend to occur, resulting in significant calibration issues. Even with these limitations, the campaign was a success. Apart from the scientific return, a great deal was learned about how to improve the instrument for future campaigns (Jounot et al., 2002).

2.2 MOPITT-A Instrument Description

The MOPITT and MOPITT-A instruments both use the technique of correlation spectroscopy to infer CO and CH_4 concentrations in the atmosphere. Briefly, the technique measures upwelling radiation from the surface that is modified by both absorption and emission from any CO or CH_4 that is present in the atmosphere. This radiation contains the spectroscopic signature of any CO or CH_4 between the instrument and the ground. The key to the technique is to direct the atmospheric radiation through a gas-cell filled with the target species, either CO or CH_4, and another identical gas-cell which is empty. The spectroscopic signature in the atmospheric signal is aligned with the absorption features of the target species in the filled gas-cell while no spectral alignment occurs in the empty cell. The difference between the signal emerging from each cell permits the spectroscopic signature originally present in the atmospheric radiation to be determined. Inversion schemes can then be applied to derive concentrations of CO and CH_4 in the atmosphere.

The MOPITT instrument uses 8 spectral windows to measure CO and CH_4 while MOPITT-A only uses 4 channels, which are identical to the upper 4 channels (5, 6, 7, 8) of MOPITT. In reality, the full and empty gas-cells in each spectral window are made from one physical gas-cell, of which there are two types. The first type of gas-cell is a length modulated cell (LMC) that physically rotates around an axis to introduce long and short optical path lengths into the radiation beam. The second type of cell is a pressure modulated cell (PMC) that uses a small piston to modulate the pressure of gas inside the cell. The change in pressure introduces a change in number density which, in turn, provides long and short optical path lengths. A schematic of the 4 channels used in MOPITT-A is shown in Figure 2.3. In this work we focus on channel 5 which uses a length modulated cell to measure CO at 4.7μ.

In practice, MOPITT-A is a complicated piece of hardware. A photograph of the instrument is shown in Figure 2.4. It is readily evident that MOPITT-A is composed of many parts, both internal and external. However there are five major sub-systems (i) gas-cells, (ii) optical chopper, (iii) black body sources, (iv) detector nest and (v) electronics. In addition, a 28 VDC, 33 A power supply, processing computer and vacuum pumping station are required to operate the instrument.

The optical path through one channel of the instrument is depicted in Figure 2.5. Radiation enters the instrument from one of four different sources, either from the atmosphere or one of three onboard black body calibration sources. The source of

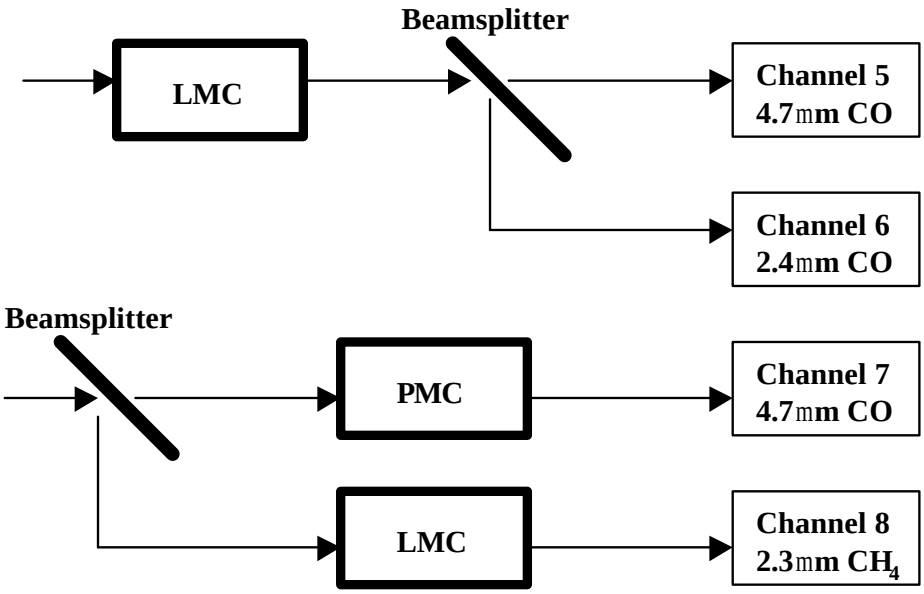

Figure 2.3: Channels 5 through 8 of MOPITT-A which consist of 3 CO channels (channels 5-7) and one methane channel (channel 8). Channels 5 and 6 receive radiance from one optical path while channels 7 and 8 receive radiance from the other.

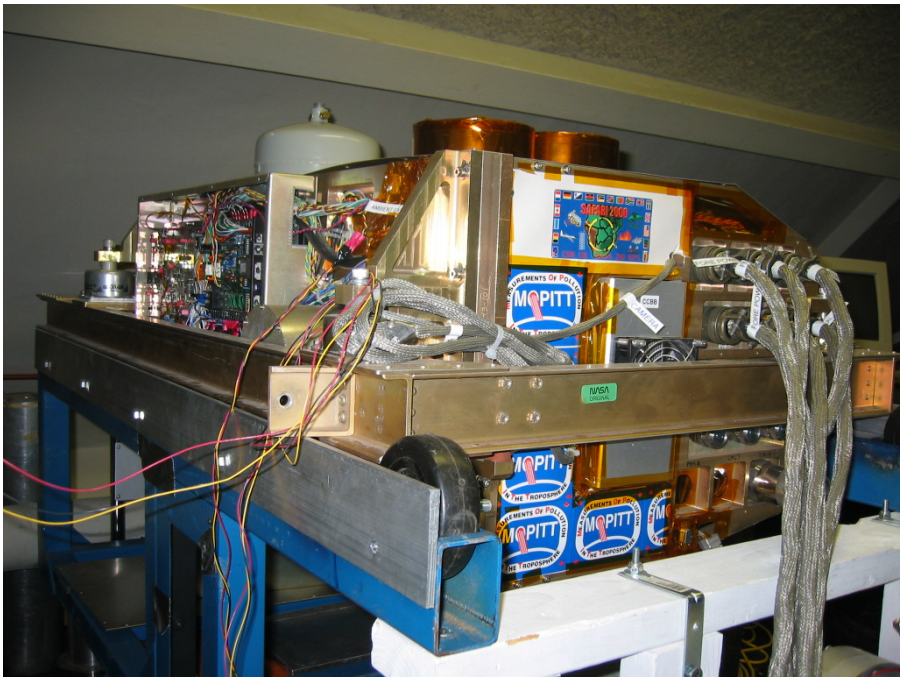

Figure 2.4: MOPITT-A stationed in the ISAS Optics Laboratory. This figure shows the power/data connections on the right, the hot black bodies (in copper) on the top and the liquid nitrogen dewar (in grey).

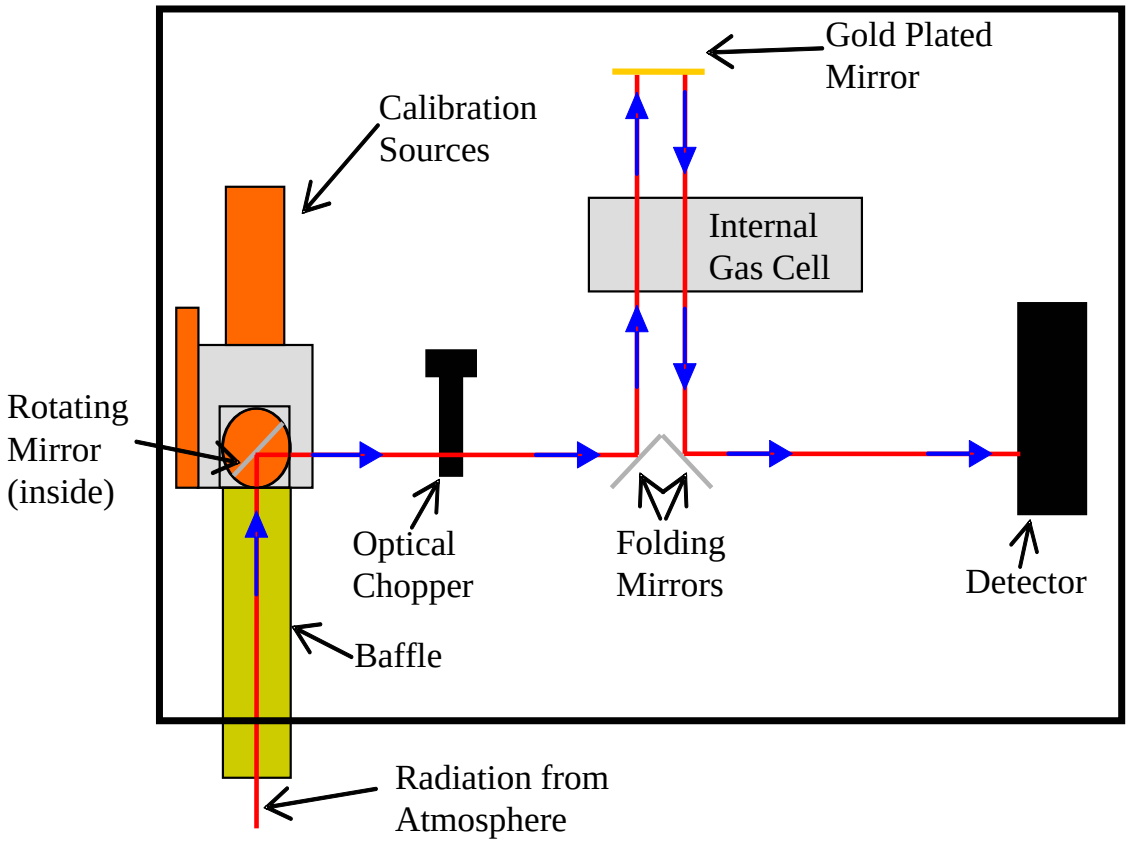

Figure 2.5: Simplified optical path through MOPITT-A showing the multiple input radiance sources, the optical chopper and the double pass system of the internal gas-cell.

radiation is selected by turning a stepping mirror, found at the top of the baffles, to the appropriate location. The incoming radiation passes through an optical chopper and onwards to the gas-cell. The radiation is directed through the gas-cell where, upon emerging, it is reflected back through the gas-cell, doubling the effective optical depth. Finally, the radiation is directed towards the detector nest and digitized.

Length Modulated Cell

The length modulated cell (LMC) is composed of four main parts as shown in Figure 2.6 and Figure 2.7. These are the gas-cell, optical windows, rotor and compensator (Drummond et al., 1993).

The gas-cell is a sealed unit with a thickness of 10 mm, measured from the inside of the front to the back wall. Its purpose is to contain the gas of the target species, CO or CH_4, as well as house the rotor assembly. Germanium optical windows of

negligible thickness are located on the front and back of the gas-cell, and allow the atmospheric radiation to enter and exit the gas-cell. The gas-cell is sealed and filled with gas to a specified pressure. The cell used for channel 5 of MOPITT-A was constructed and tested at the University of Toronto (Tolton et al., 1997) to sustain an internal pressure of 80 kPa (0.7895 atm), which is much higher then a traditional correlation gas-cell pressure of 10 kPa (Drummond et al., 1993). In the case of MOPITT-A the gas-cell is filled with CO, as this is the gas of interest.

The rotor is a piece of calcium fluoride (CaF_2) glass which is 8 mm thick and shaped like a bow-tie. The rotor is sealed within the gas-cell and is fastened to the cell by a magnetic coupling, allowing it to be driven by an external motor. The rotational position of the rotor dictates the amount of gas in the optical path. When the glass bow-tie segment of the rotor is in the optical path it displaces the gas and produces a signal equivalent to an empty cell. Conversely, when the rotor is out of the optical path, the signal is equivalent to a full cell. The rotor spins at constant frequency and the optical path alternates between full and empty states. The rotor has the ability to rotate at a maximum frequency of 10 revolutions per second. In reality, the glass rotor only occupies 8 mm of the 10 mm of the space in the gas-cell. Thus the empty condition is not truly empty but has 2 mm of gas remaining in the optical path. This rotor state is called the *short path* position because it is the state with the shortest path length. Likewise, the state, when the rotor is out of the optical path and the entire 10 mm space is filled with gas, is called the *long path* state.

The compensator is located outside the gas-cell on the back end of the cell. Its physical makeup is exactly the same as rotor, being an 8 mm thick piece of CaF_2. The compensator is fastened to the outside of the gas-cell by a magnetic coupling but is exactly 90° out of phase with the rotor. The rotor/compensator tandem rotate together at a constant frequency. This allows the compensator to mimic the optical absorption and emission properties of the primary rotor during the *long path* state, ensuring both *long path* and *short path* states are optically identical apart from the gas in the gas-cell.

The physical makeup of the LMC has several desirable attributes. First, it can rotate continuously at a relatively fast rate. This produces advantages mechanically, electrically and scientifically. Second, it can tolerate higher pressures than other gas-cell designs. This is important for retrieving CO distributions from higher pressure

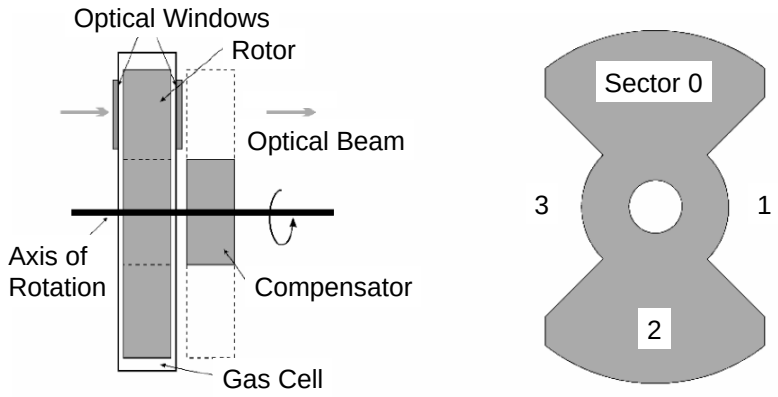

Figure 2.6: Side View of Length Modulated Cell and Front View of the Calcium Fluoride Rotor/Compensator.

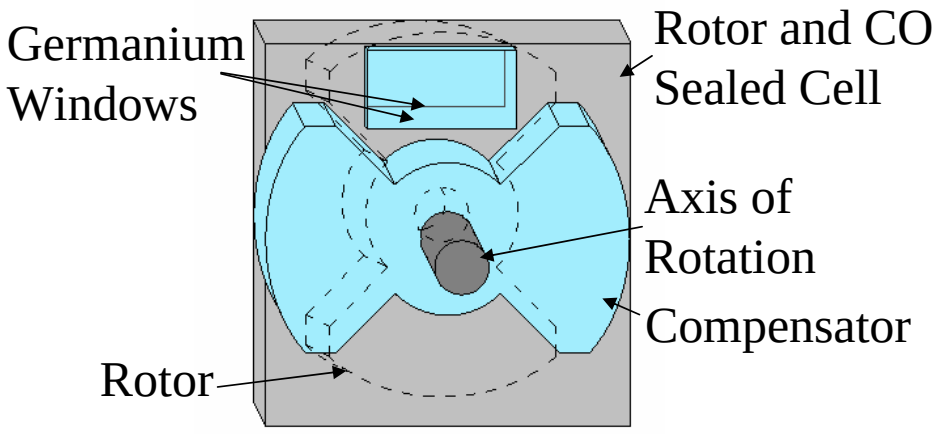

Figure 2.7: 3-D Model of the MOPITT-A Length Modulated Cell as seen from the back (not to scale).

altitudes lower in the atmosphere.

Optical Chopper

The chopper is a rotating slotted blade that either blocks or passes the incoming radiation from the rest of the optical train. The signal collected in the blocked position allow contaminant background signal to be removed from the primary signal measured in the open position. The MOPITT-A chopper is a modified New Focus Optical Chopper Model 3501, as shown in Figure 2.8. The chopper blade is comprised of 21 evenly spaced slots. Choppers have been traditionally used for AM modulation in IR measurements, where the impact of broad-band noise is limited by selecting

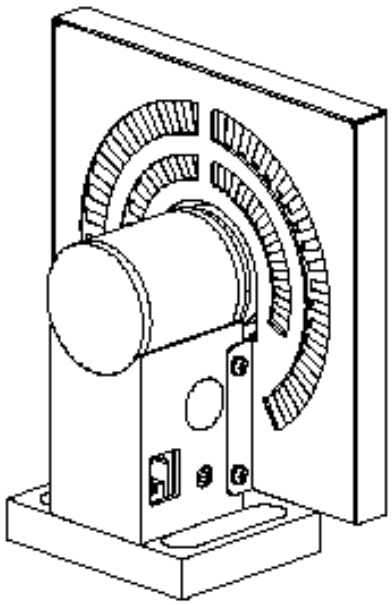

Figure 2.8: The New Focus Optical Chopper Model 3501 used in MOPITT-A (New Focus: Model 3501 User's Manual Optical Chopper Rev. B).

a narrow, notched, region in the frequency domain to increase the signal to noise ratio. However, MOPITT-A does not need to implement this technique as the signal to noise ratio is sufficient if the detector nest is kept at low temperatures.

The Onboard Black Body Sources

The MOPITT-A system has a total of 5 black body sources that were intended for continuous calibration of the instrument. Each spectral channel has access to three black body sources: a hot (500K max), warm (300 K max) and a cold source (250K min). The original intent was to frequently calibrate atmospheric signals using a three point fit to the three black body signals. The black body sources are located very close to the front-end optics. This eliminates a considerable amount of systematic error due to stray glow. The radiation from the sources traverses a path almost identical to that travelled by the external atmospheric radiation.

The onboard black body system illustrated in Figure 2.9 (Bailak et al., 1999) was built by Bomem for the MOPITT-A instrument. The black bodies were built to reach thermal stability in approximately 30 minutes, which is the ascent time of the aircraft during flight missions. The temperature of each black body source is controlled

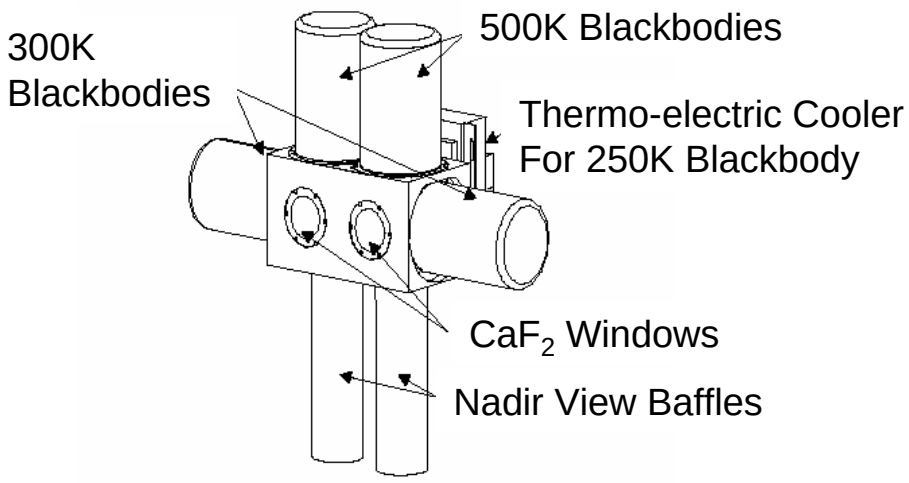

Figure 2.9: The MOPITT-A Onboard Calibration Sources.

through an interface in the signal processing module. Each individual black body is insulated to provide thermal stability and assist in its thermal isolation from the rest of the system. However, it was found during the SAFARI-2000 mission that the thermal insulation was insufficient and the black body sources showed significant drift throughout the mission.

The Detector Nest

The MOPITT-A instrument has 4 spectral channels and each channel employs a 4x1 linear array InSb photo-sensor to detect the radiation. Incident radiation creates an electric signal in the InSb detector via the photoelectromagnetic effect. Briefly, electron-hole pairs are produced near the surface when an InSb crystal is exposed to radiation with a frequency close to its fundamental absorption edge. Placing the crystal in an external magnetic field forces the electron-hole pairs to separate and drift in opposite directions to the unilluminated sides of the crystal (Young, 1960). The process is illustrated in Figure 2.10 (Houghton, 1966). The separation of charge causes an electromagnetic field to be produced whose magnitude is proportional to the number of electron-hole pairs created and therefore the number of photons striking the crystal surface. The quantum efficiency of an InSb detector is approximately 80% and can be even higher when cooled to the proper temperature.

The 4 detectors are encased within a sealed dewar system that keeps the detectors at low temperature. The dewar is filled with liquid nitrogen (LN_2) which cools the

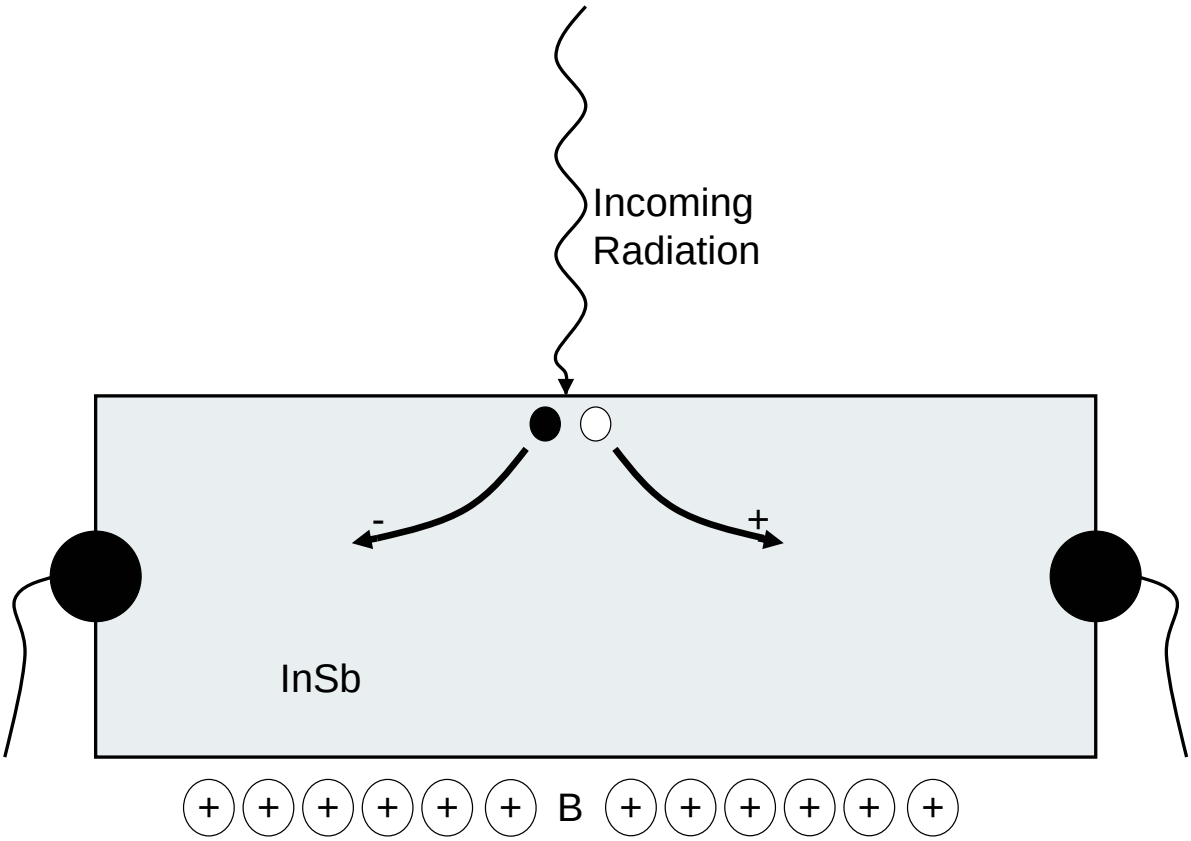

Figure 2.10: The separation of the electron-hole pair created through the photoelectromagnetic effect in a InSb crystal.

detectors to approximately 95 K. This cooling not only minimizes thermal noise but also exceeds the operating threshold of 120K for the InSb. The dewar is evacuated to a pressure between 10^{-4} mbar and 10^{-6} mbar. This eliminates problems with frosting on the detector surface and significantly improves the evaporation lifetime of the LN_2. The LN_2 will normally last for about three days before a refill is required.

Each detector contains two, nominally identical filters used to select the spectral region of interest for the spectral channel. One of the filters is used for the inner pixels(2,3) of the linear array and the other for the outer pixels (1,0). The filters were constructed at the University of Toronto. The spectral response of the two filters used for channel 5 of MOPITT-A are shown in Figure 2.11.

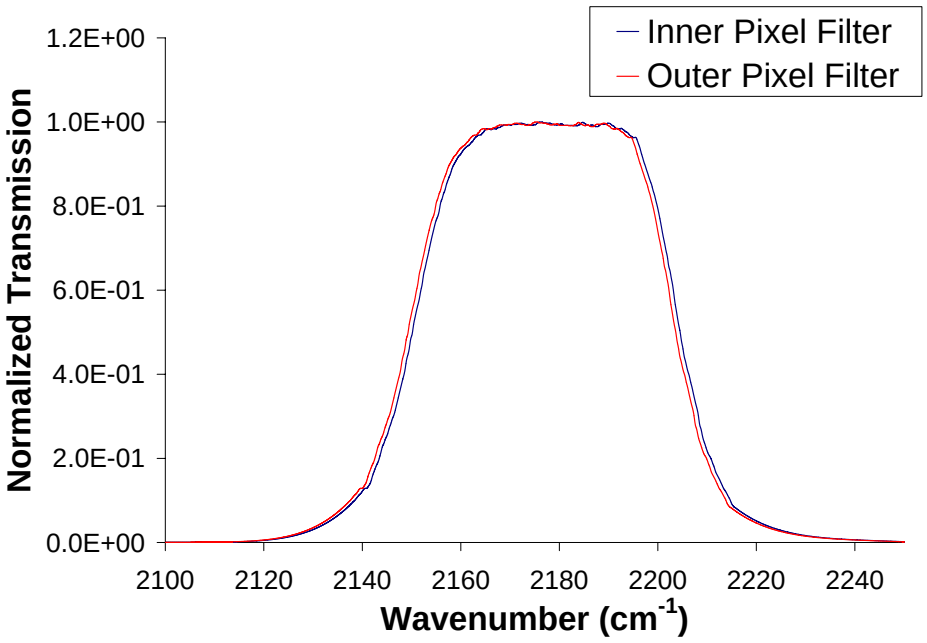

Figure 2.11: Filters for the inner pixels (2,3), in blue, and outer pixels (1,0), in red, for channel 5 of MOPITT-A.

2.2.1 Optics

All of the lenses used in the construction of MOPITT-A were built from germanium or calcium fluoride as they had to operate in the infra-red. Likewise, all of the mirrored surfaces were gold-plated for optimal infra-red performance. All of the optics between the chopper and the gas-cell are encased in a sealed black box while the double pass optics are contained inside the gas-cell casing. Alignment of the optics is a straight-forward but time-consuming process. Consequently, we were very careful not to disturb the optics.

2.2.2 Timing Control Unit

The collection of data with MOPITT-A requires precise synchronization between the chopper, gas-cell rotor and detector nest. The timing of this coordination is the responsibility of the Timing Control Unit. The chopper and the gas-cell rotor are both controlled by phase-locked loop circuitry that ensures a high degree of synchronicity between the two rotating parts. The Timing Control Unit emits a reference clock that is accurately synchronized to the rotation of the chopper and gas-cell rotor.

The reference clock is used to define intervals of time when the gas-cell rotor is either fully inserted into the optical path or completely removed. In practice, the system breaks each rotation of the gas-cell rotor into 4 sections, allowing the analysis to identify which half of the rotor is in the optical path. The system ignores periods when the rotor is partially inserted into the optical path. The system also inspects the status of the chopper blade which generates open and closed segments an order of magnitude faster than the gas-cell rotor. Similar to the gas-cell rotor, the system only considers periods of time when the chopper blade either completely blocks the optical path or allows it to pass unhindered. The system ignores periods of time when the chopper blade partially obstructs the optical path.

The timing diagram for a typical data process cycle is shown in Figure 2.12. The top line shows the chopper state index derived from a photo-sensor attached to the chopper blade. The chopper open state is longer than the closed state, mimicking the physical width of the slots on the chopper blade. The second line is the chopper processing clock and, when high, permits the detector nest to acquire measurements. Regardless of chopper state, measurements are only collected when the chopper blade is in its proper position; transitional periods are ignored. The yellow bars in Figure 2.12 indicate data acquisition periods with the chopper open and the blue bars indicate data acquisition periods with chopper closed.

The third line in Figure 2.12 represents the rotational position of the gas-cell rotor expressed as a binary number. The actual system uses two digital signals as the rotor will be in one of four quadrants. The bottom line is the LMC processing clock. Similar to the chopper processing clock, the detector nest is only allowed to acquire data when this latter signal is high.

2.2.3 External Hardware

The external dimensions of the MOPITT-A instrument are 140x68x54 cm and it has a mass of approximately 65 kg, a size and mass consistent with the ER-2 constraints (Bailak et al., 1999). However, this excludes two, 19" rack mounted, boxes that are used for instrument operation and control. These two boxes can be seen to the center right of Figure 2.13. The first box is the MOPITT-A Airborne Power Supply Box which converts an external 28 VDC source to the various internal voltages required by MOPITT-A and distributes them to the instrument. The 28 Volts is the only external power source required to operate the MOPITT-A instrument. The ER-

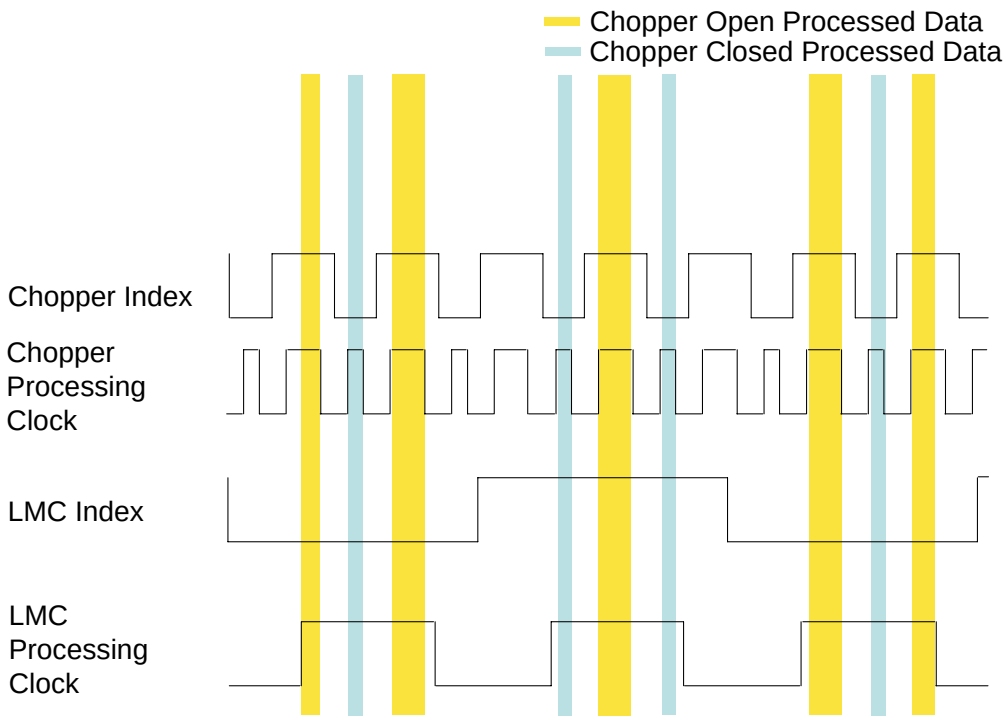

Figure 2.12: Timing diagram of the data processing cycle for MOPITT-A. Processed data with the chopper open is seen in yellow, while processed data with the chopper closed in seen in blue. This diagram is not to proper scale.

Figure 2.13: The MOPITT-A Airborne Power Supply Box and Airborne Electronics Box in the University of Saskatchewan ISAS Optics Laboratory.

2 aircraft supplies the 28 Volts during flights and a Sorensen 1000W Power Supply Model DCS 33-33 is used when MOPITT-A is on the ground. The maximum current used by MOPITT-A is approximately 10 A.

The second rack mounted box is the MOPITT-A Airborne Electronics Box which contains the Instrument Control Computer as well as various circuitry to govern timing, data transfer and housekeeping sensors. The combined size of the two boxes is 62x43x48 cm. Both boxes are connected to MOPITT-A and each other through several military specification, Amphenol connectors.

The Instrument Control Computer runs a custom program, mopitta.exe, under the DOS operating system. The program coordinates all of the instrument activities and records all data onto a local hard drive. The hard drive is physically removed from the system at the end of a flight or measurement session and the information transferred to a normal PC computer for analysis.

Data are transferred from the MOPITT-A instrument to the Instrument Control Computer in 32-bit packets. The layout of the 32-bit packets is shown in Table 2.1 (Drummond, 2000).

The Instrument Control Computer stores the packet data on disk in a SCI file format. A new file is generated every 12 minutes to avoid loss of data if the system

Bit numbers (0=LSB)	Size	Function
31	1	Unused
29-30	2	Channel (0-3)
27-28	2	Pixel (0-3)
25-26	2	LMC Sector (0-3)
24	1	Chopper State
0-23	24	Data

Table 2.1: Breakdown of the 32 bit data packets collected by MOPITT-A.

crashes or is otherwise powered off. Data and housekeeping information collected by the Instrument Control Computer are displayed on a monitor, although the monitor is removed for flights.

After the raw SCI, proprietary, files have been transferred to a normal PC they are converted and merged into standard HDF files. The HDF data files are generated according to spectral channel, detector pixel, LMC sector, and chopper state. An example for one file would be channel 5, pixel 1, chopper open, LMC sector 1. One spectral channel can generate up to 32 separate data files as there are four detector pixels, four LMC sectors and two chopper states.

2.2.4 MOPITT-A at University Of Saskatchewan

The MOPITT-A instrument was built and commissioned for the University of Toronto for the purposes of validating the MOPITT instrument. After this exercise was completed, the instrument was delivered to University of Saskatchewan in the summer of 2001. The instrument was examined upon its arrival at ISAS, University of Saskatchewan. A few minor problems were identified and repaired. The channel 5, chopper electronics board was not synchronizing properly; it was replaced with the channel 8 board. The channel 5, gas-cell, pressure transducer was not accurate; it was replaced with an external pressure transducer. Finally, a few loose wires were found and fixed or replaced.

In August of 2002, the MOPITT-A instrument was taken on a field campaign by the Infra-Red Group at the University of Saskatchewan to a hang gliding launch platform located near the summit of Mount 7, Golden, British Columbia. This site was specifically chosen as its altitude, 1560 m above sea level, is one of the highest

Figure 2.14: Panoramic display of the Mount 7 observing site, provided by Google Earth.

in the Rockies accessible by road (see Figure 2.14).

A mounting plate was constructed for MOPITT-A and the instrument was installed in the rear of a covered pick-up truck for transport to and from the observing site. The instrument and various other equipment were secured with nylon rope to the truck to ensure minimal movement, especially over the last few kilometers of steep mountain road. Upon arrival at the observing site, the pick-up truck was positioned near the edge of the site so the instrument could look down the mountain towards the town of Golden. A tarp system was setup to protect both MOPITT-A and the computer systems from the elements. Photographs of the deployed system are shown in Figures 2.15 and 2.16.

The system was powered with a gasoline generator as no electrical power is available at the site. This required the instrument to be shut down for 5 to 15 minutes every 8 hours so the generator could be be refueled. Data were also transferred from the Instrument Control Computer to PC computers at this time, to permit further on-site analysis at the hotel. The gas generator was placed approximately 60 feet

Figure 2.15: The MOPITT-A instrument and flight computers set up in the half-ton truck on Mount 7 in Golden, B.C.

Figure 2.16: The tarp setup used on Mount 7 to ensure the instrumentation remained protected from the elements.

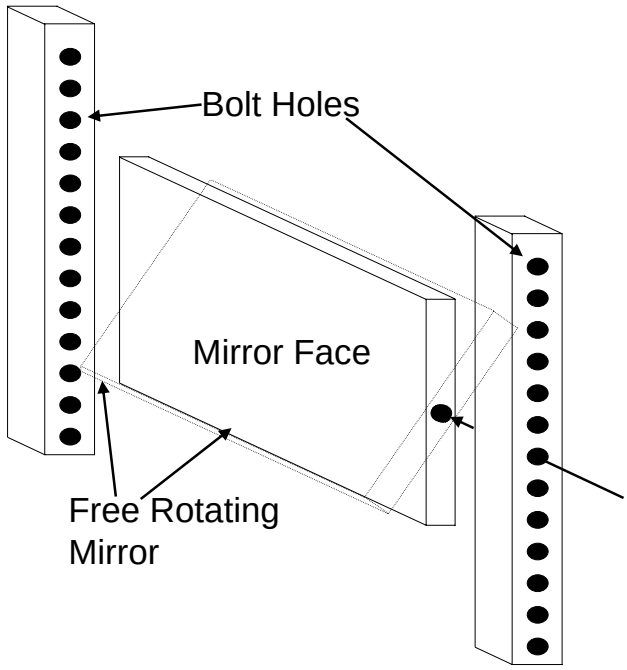

Figure 2.17: The external mirror system used for the MOPITT-A instrument to allow for a multi-angular look direction.

away from the instrument to minimize contamination from the generator exhaust.

The channel 5 gas-cell was filled with CO at the University of Saskatchewan prior to departure and its pressure monitored during the campaign. The pressure in the gas-cell was stable for the entire duration of the mission. The detector nest dewar was filled with liquid nitrogen at the start of observations and was replenished daily without issue.

MOPITT-A is a nadir viewing instrument and thus required an external mirror system to look out of the back of the pick-up truck. A silvered mirror was placed on two adjustable bars directly below the baffles of MOPITT-A. The mirror was attached by two allan screws which allowed the mirror to be adjusted to the required angle, see Figure 2.17. The mirror was aligned with the side of the mountain by eye. The mirror was rotated until an observer, standing approximately 50 feet down the mountain, could see the center of the instrument's input baffles. It was readily evident to another observer collocated with the mirror, looking at the eyes of the observer down the mountain, that this alignment placed the instrument's field of view over the town of Golden. The view from the MOPITT-A instrument is shown in Figure 2.18.

The instrument was operated almost continuously for 41 hours from 14:15 LT

Figure 2.18: The view from the MOPITT-A instrument over Golden B.C. from atop Mount 7.

2002-08-20 to 07:30 LT 2002-08-22. The weather was extremely cooperative and provided us with continuous clear sky conditions. The instrument was manned by at least two people at all times during the campaign. During the daytime the observing site was frequented by several hang gliders and paragliders. Apart from offering some spectacular entertainment, the gliders would occasionally stray in front of the MOPITT-A field of view, blocking measurements for a few minutes while they prepared to launch.

Nine hours of measurements from mid afternoon to late evening for channel 5, pixel 1, gas-cell rotor position 0 are shown in Figure 2.19. The sharp decline in signal in the first half hour of measurements is due to the cooling of the instrument by the liquid nitrogen. After this time, the instrument is much more stable and a steady systematic difference between the chopper open and closed signals is readily evident. Both measurements display a slow downward trend which we attribute to the instrument cooling as nighttime and cooler temperatures set in. The gaps in the data are places where the generator was refueled.

Figure 2.20 shows the result of removing the background, chopper closed signal from the chopper open signal for two positions of the gas-cell rotor. Differences

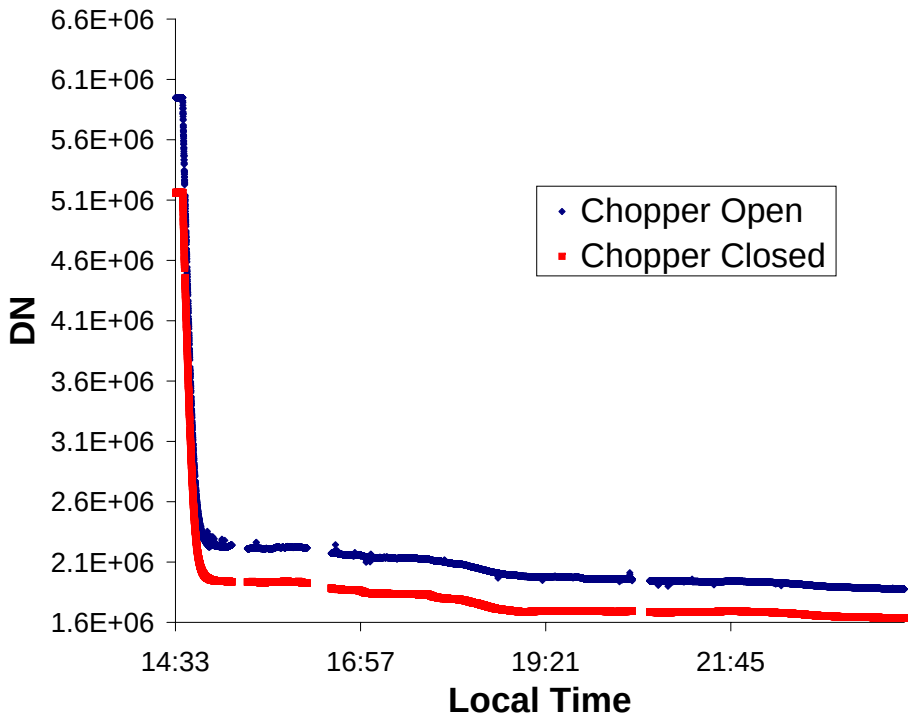

Figure 2.19: Data set gathered from 14:30 to 23:59 LT during the Golden B.C. mission. This compares the chopper open signal (blue) and the chopper closed signal (red) from pixel 1, gas-cell state 0 of channel 5.

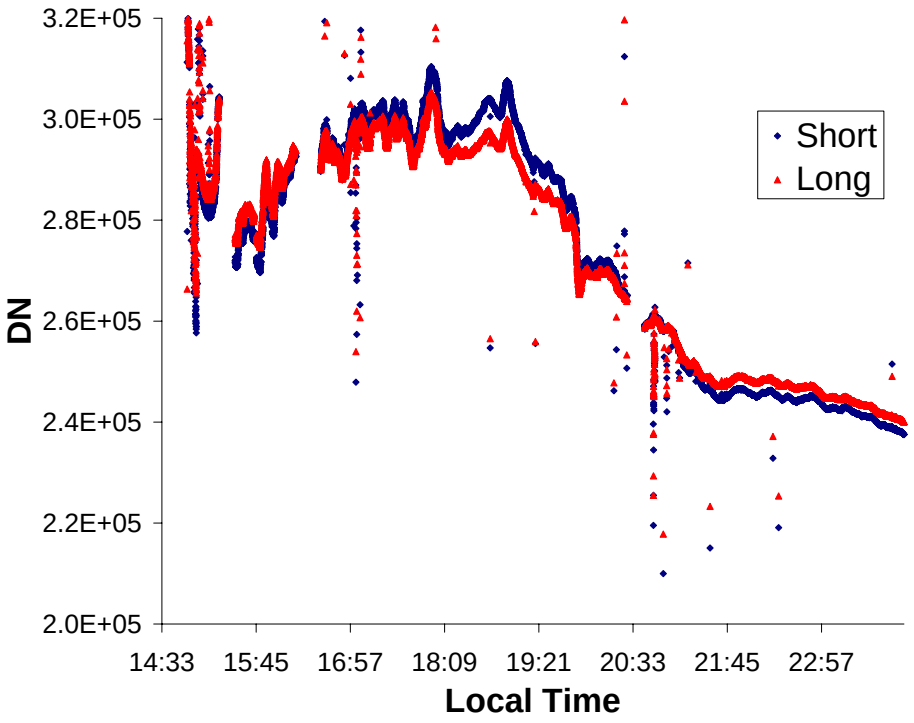

Figure 2.20: Data set gathered from 14:30 to 23:59 LT during the Golden B.C. mission. This compares the difference in chopper states for the short gas-cell path length (blue) and the difference in chopper states for the long gas-cell path length (red).

between the *short path* and *long path* are evident indicating that the CO in the gas-cell during the *long path* is absorbing some of the radiation passing through the cell. The short lived spikes are mostly due to hand gliders blocking the field of view.

Figure 2.21 shows the difference between the *short path* and *long path* signals, indicating the degree of absorption that occurs in the *long path* gas-cell. It is quite apparent that there is a time dependency to this signal and it would appear that the MOPITT-A had detected CO over Golden BC. However, before we make this claim we must develop and apply the theory of correlative spectroscopy and radiative transfer as well as consider all of the possible systematic effects that could occur.

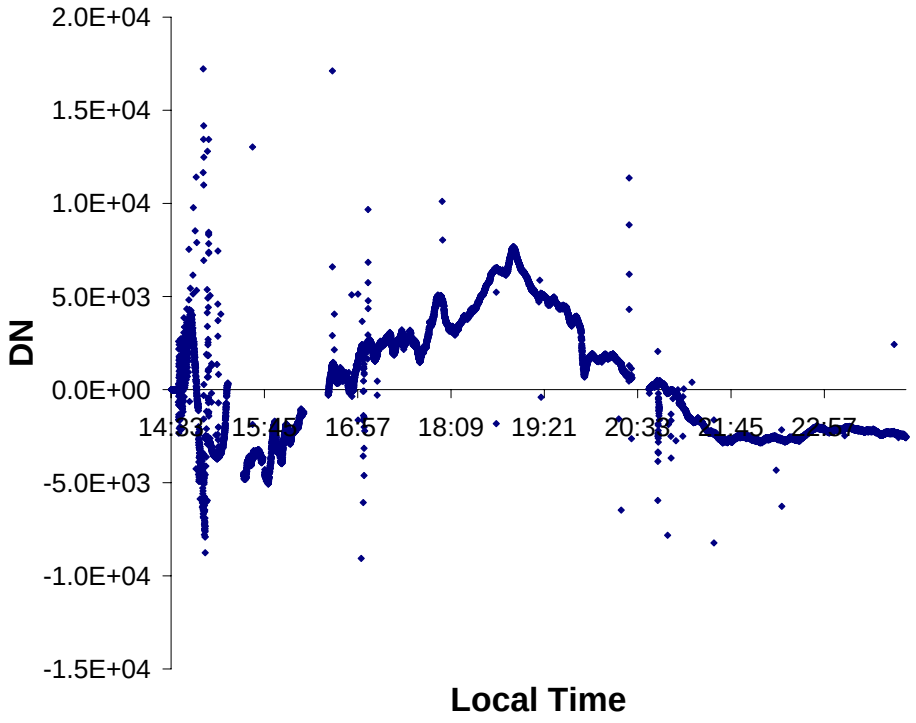

Figure 2.21: Data set gathered from 14:30 to 23:59 LT during the Golden B.C. mission. This depicts the difference in the two states shown in Figure 2.20, known as the Difference signal.

Chapter 3

Radiative Transfer of MOPITT-A

3.1 Introduction

Radiative transfer studies the propagation of radiation through a medium and its interactions with the surrounding environment. The propagation of radiation in a planetary atmosphere is affected by the distribution of atomic and molecular species. In general, molecules affect the propagation of radiation via three mechanisms: (i) absorption of radiation, (ii) thermal emission of radiation and (iii) scattering of radiation. Any molecules that actively participate in the propagation of radiation impart their own signature onto the radiation field and subsequent analysis permits retrieval of the molecular species. In addition, the atmospheric state parameters of temperature and pressure play a significant role in atmospheric radiative transfer.

Absorption is the physical process by which photons are removed from the radiation field. If an atmospheric layer has a number density of molecules, n, and each of these molecules presents an effective cross sectional area, σ, to the ray of light propagating through the medium, then the probability of a photon being absorbed by one of these molecules along the differential path, ds, is given as,

$$P = n\sigma \, \mathrm{d}s. \tag{3.1}$$

This equation is known as Beer's Law, which states that the radiation coming into a gas will be changed due to absorption of the radiation from particles that make up the gas (Hanel et al., 1992). If this probability of interaction is multiplied by the incoming intensity this term is the amount of radiation absorbed by the molecules in the layer.

Thermal emission is the physical process by which new photons are added to a radiation field. The thermal emission of a gas in thermal equilibrium is given by the Planck function,

$$B(\nu, T) = \frac{2hc^2\nu^3}{\exp[\frac{hc\nu}{kT}] - 1} \text{ erg/s/cm}^2/\mu\text{m/ster}, \tag{3.2}$$

where h is Planck's constant, c is the speed of light, ν is the wavenumber, T is the temperature of the source and k represents the Boltzmann constant.

The principle of detailed balance states that for a gas in thermal equilibrium, the emission and absorption will be equal at all wavenumbers. This provides the mechanism to calculate the thermal emission of a gas under local thermal equilibrium (Reif, 1965). The total intensity resulting from thermal emissions in the atmosphere is acquired by multiplying the Planck function by the probability from equation 3.1.

The third physical process involved in radiative transfer is scattering. Elastic scattering is the physical process by which photons are redirected in the atmosphere without loss of photon energy. Elastic scattering is usually dominated in a planetary atmosphere by Rayleigh and Mie processes. Inelastic, Raman scattering can also occur and, in this case, energy is transferred between the photon and scattering molecule, changing the frequency of the radiation. All scattering processes only make minor contribution to the infra-red signal observed by the MOPITT-A and are not considered any further here (Hanel et al., 1992).

3.2 Molecular Cross Section

The molecular cross section σ, is the apparent mean cross sectional area that a single molecule presents to an incident beam of radiation. The magnitude of the cross section is governed by quantum mechanical phenomena that change with both temperature and pressure and is, therefore, not constant throughout the atmosphere.

The cross-section has been calculated in this work using the parameters contained in the HITRAN (HIgh-resolution TRANsmission) database provided by Rothmann et al. (1998). Briefly, the molecular cross section is given by,

$$\sigma = S(T)f(\nu, T, p), \tag{3.3}$$

where *S(T)* is the spectral line intensity and *f(ν,T,p)* is the pressure broadened line shape. The HITRAN database contains values of line intensities at a reference

temperature and pressure. The line intensity at other temperatures and pressures are derived using the formula provided by Rothman et al. (1998),

$$S_{kl}(T) = S_{kl}(T_{ref})\frac{Q(T_{ref})}{Q(T)}\frac{e^{-c_2 E_k/T}}{e^{-c_2 E_k/T_{ref}}}\frac{[1-e^{-c_2\nu_o/T}]}{[1-e^{-c_2\nu_o/T_{ref}}]}, \tag{3.4}$$

where T_{ref} is the HITRAN reference temperature of 296 K, $S_{kl}(T_{ref})$ is the line intensity at the reference temperature, k is the lower energy state of the molecule, l is the upper energy state of the molecule, Q(T) is the partition function, $\nu_\circ$ is the central wavenumber of the spectral line and c_2 is a constant equal to

$$c_2 = \frac{hc}{k} = 1.4388\,\mathrm{cm\,K}. \tag{3.5}$$

The partition function depends on temperature and is given as

$$Q(T) = \sum g_\eta \exp(\frac{-c_2 E_\eta}{T}), \tag{3.6}$$

where g_η is the lower state statistical weight and E_η is the lower state energy. The partition function is difficult to tabulate for each species so a parametrization based on a cubic polynomial is used. The equation is given as

$$Q(T) = a_0 + a_1 T + a_2 T^2 + a_3 T^3, \tag{3.7}$$

where a_0, a_1, a_2, and a_3 are empirical coefficients that depend on the molecule and temperature. The coefficients for each molecule are tabulated for a limited temperature range and therefore many sets of coefficients exist for each molecule. All of the parameters required for equation 3.4 are contained in HITRAN.

Line broadening is represented in equation 3.3 as $f(\nu, T, p)$. This is another effect that governs the molecular cross section at a specific wavelength. There are two types of line broadening. These are known as Collision broadening and Doppler broadening.

Collision broadening can be understood as a quantum mechanical effect that results from the finite time between molecular collisions. The uncertainty principle states that if the energy of a quantum mechanical process is precisely known then the time at which this process occurred is infinitely uncertain, and vice versa. Because molecular transitions must occur between collisions the average maximum time of a transition is known. Therefore, the energy, or wavelength, of the transition has some uncertainty. This uncertainty in wavelength causes the broadening of the spectral line. This broadening follows a Lorentzian distribution. Collision broadening plays

a very important role at lower altitudes because the larger number densities result in more frequent molecular collisions. As the collision frequency increases due to the abundance of molecules the wavelength uncertainty increases.

The second type of line broadening is Doppler broadening. This is caused by random thermal motion in a group of molecules. As molecules are moving away and towards an observer the wavelength of an emitted photon changes. As molecules move away from an observer the wavelength becomes longer and as they move toward the observer the wavelengths become shorter. This is similar to astronomers viewing red shifts and blue shifts in stars moving away and toward Earth, respectively. This random thermal velocity follows a Gaussian distribution.

The true line shape, which is the convolution of Collision broadening and Doppler broadening, is the Voigt profile. At tropospheric altitudes the line width due to molecular collisions far outweighs the Doppler line width and tropospheric models need only consider the Collision broadening for the line shape, which is given by Rothman et al. (1998) as,

$$f(\nu, \nu_o, T, p) = \frac{1}{\pi} \frac{\gamma(p,T)}{\gamma(p,T)^2 + [\nu - (\nu_o - \delta(p_{ref})p)]^2}, \tag{3.8}$$

where ν_o is the central wavenumber of the spectral line under analysis, $\delta(p_{ref})$ is the air broadened pressure shift, which is zero for CO, and γ is the collision broadening coefficient. The collision broadening coefficient is given by Rothman et al., 1998 as

$$\gamma(p,T) = \left(\frac{T_{ref}}{T}\right)^n [\gamma_{air}(p - p_{part}) + \gamma_{self} p_{part}], \tag{3.9}$$

where γ_{air} and γ_{self} are the air and self broadened halfwidths respectively, and n is the coefficient of temperature dependence of air broadened halfwidth. All of the parameters in the above equations are contained in HITRAN.

The integrated spectral line intensity, $S(T)$, for any transition is a function of only temperature, not pressure, as shown in equation 3.4. However, the line shape is a function of both the pressure and temperature, as shown in equation 3.8. So, if a system were created where the temperature remained constant and the pressure changed one would expect to observe a change in the line shape, but not in the integrated line intensity. The maximum intensity may change but the intensity integrated over the entire broadening of the line does not. In a system where the pressure remained constant and the temperature changed one would expect to observe a change in both the line intensity and line shape. However, the change in the

line intensity is not always positively correlated to the change in the temperature. When the temperature of a closed system increases the molecules in that system will have enough energy to populate higher energy states. Therefore, the intensity of some lines will increase while others will decrease because of the redistribution of the molecules throughout the energy levels. Even though the individual line intensities will change the integrated intensity of the entire spectrum remains the same.

Figure 3.1 shows a CO line at three different pressures but a constant temperature. The shapes of the lines were calculated using equations 3.3, 3.4 and 3.8. It is seen that the maximum intensity of the line changes. However, the integrated intensity of each line remains the same. The reason the maximum intensity changes is because of the increased line broadening that occurs. For the broadening to increase and the integrated intensity to remain the same, the maximum intensity must decrease. As the pressure of the system is decreased the broadening of the line decreases. This is expected as a decease in pressure will increase the time between collisions in the system, and therefore decrease the uncertainty of the transitional energy.

Figure 3.2 shows a single line from a system where there is a constant pressure but a changing temperature. These lines were calculated using using equations 3.3, 3.4 and 3.8. The change in line shape due to pressure broadening is negligible and only the intensity changes. Equation 3.4 shows that a spectral line intensity will change in a dynamic temperature field. However the change is not always positively correlated. Figure 3.3 shows a different modelled spectral line of the same CO spectrum as that of Figure 3.2. The difference between the two figures is the relative intensities of the lines at each temperature. Figure 3.3 shows the line at 300 K to be the least intense while Figure 3.2 shows the line at 300 K to be the most intense. This difference is due to the change in molecular population of the energy states when the temperature of the system was changed. The total number of molecules in the system does not change, therefore as the population of some energy states increase, the populations of other energy states must decrease.

Viewing the entire spectrum leads to a more complete understanding of how changing temperatures in a system affect the energy state populations. Figure 3.4 shows the CO vibrational transition 0-1 spectrum at 200 K. This spectrum shows the majority of the spectral lines to be located between 2050 and 2230 cm^{-1}. Figure 3.5 is the entire CO vibrational transition 0-1 spectrum at 300 K, and this spectrum

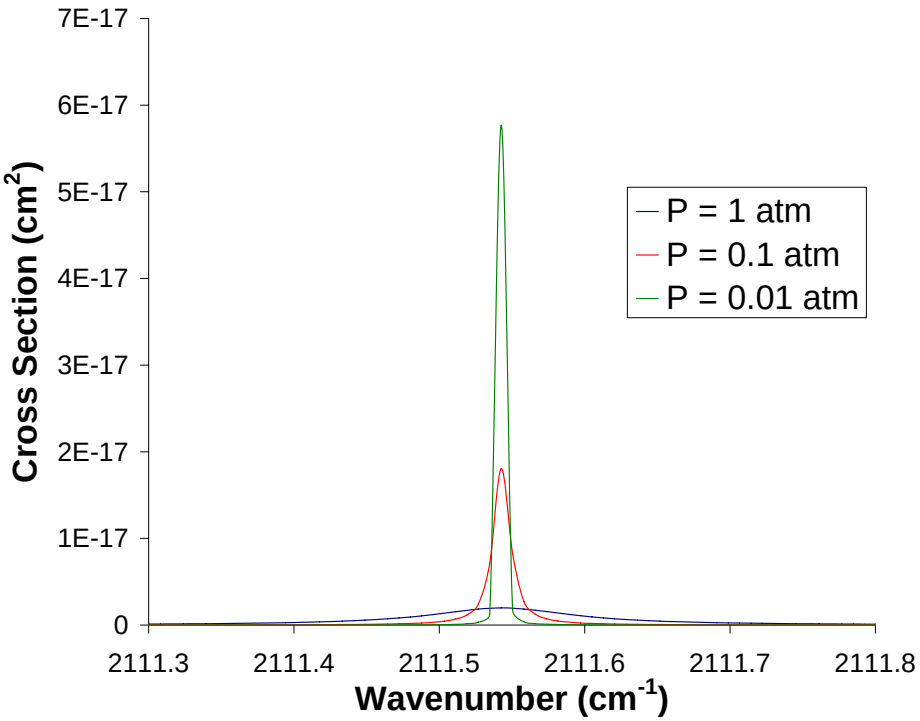

Figure 3.1: A single spectral line of CO centralized at 2111.54 cm^{-1} measured at a temperature of 300 K and a pressure of 1 atm (blue), 0.1 atm (red) and 0.01 atm (green).

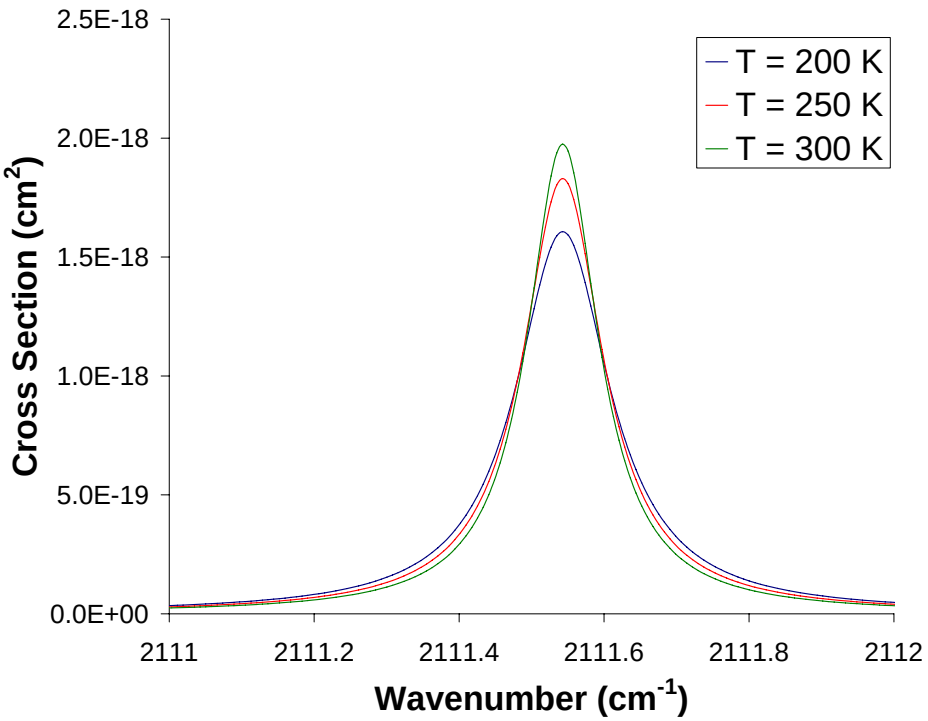

Figure 3.2: A spectral line centralized at 2111.54 cm^{-1} and measured at a pressure of 1 atm and a temperature of 200 K (blue), 250 K (red) and 300 K (green).

shows a relatively higher population of the upper energy states than the spectrum of Figure 3.4. This is seen through the relatively more intense wings that are present in the higher temperature spectrum. As higher energy states are being populated the distribution of the molecules over the spectral range changes. The intensity of the lines in the middle of the 300 K spectrum has actually decreased because there are less molecules populating the energy states associated with these lines.

If the temperature of a closed system remains constant while the pressure is increased the broadening of the spectral lines is expected to increase, but the integrated line intensity will remain the same from pressure to pressure. If the pressure of this system remains constant and the temperature is increased the broadening is expected to change slightly and the individual integrated line intensities are expected to change due to change in distribution of the molecules across the energy states. However, the integrated line intensities of the entire spectrum will remain constant.

In summary, the HITRAN database provides information to calculate the absorption cross section for CO at all atmospheric temperatures and pressures.

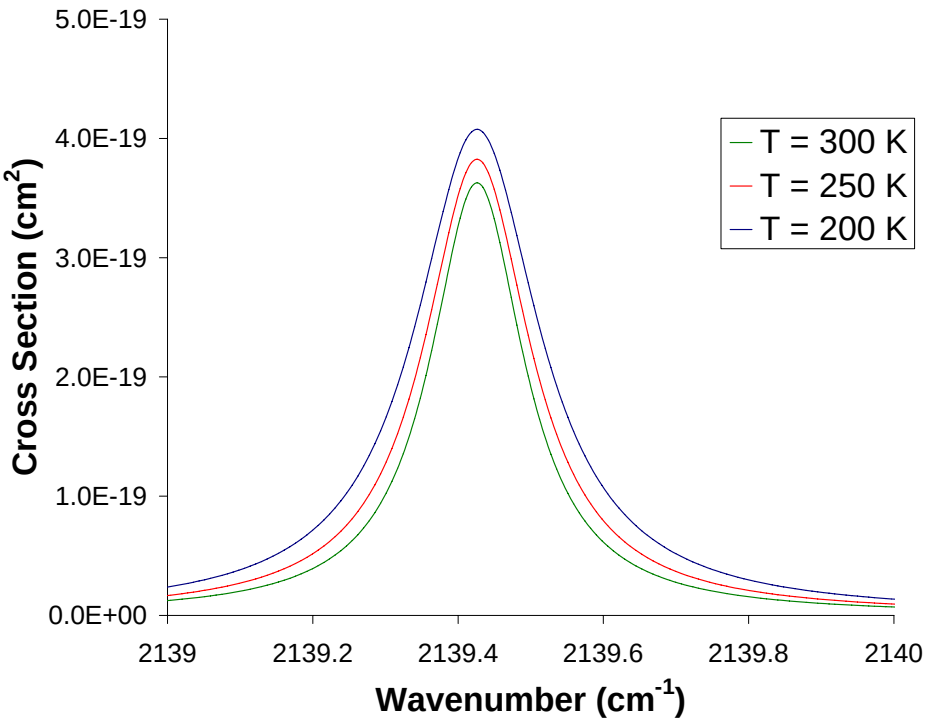

Figure 3.3: A spectral line centralized at 2139.43 cm^{-1} and measured at a pressure of 1 atm and a temperature of 200 K (blue), 250 K (red) and 300 K (green).

3.3 Radiative Transfer in a Single Layer

MOPITT-A is an aircraft-borne optical instrument that looks downward and measures terrestrial thermal emissions in the range 2100 - 2250 cm^{-1}, which spans one rotational band of CO. The measurements are used to infer the column concentrations of CO below the instrument during its flight.

The MOPITT-A geometry, to first order, is a nadir viewing instrument observing the thermal, black body radiation spectrum emanating from the Earth's surface. The upwelling radiation is modified by both absorption and emission from any CO that might be present in the atmosphere. In this section we shall develop the Schwarzschild model (Chamberlain et al., 1987; Fleagle et al., 1980; Janssen, 1993; Hanel et al., 1992), which is used to model radiative transfer in a thin, homogenous layer. This single layer theory is then applied to the real atmosphere by building a discrete multi-layer system model.

Figure 3.6 illustrates a single homogeneous layer where I_0 is the intensity of incident monochromatic radiation and I_f is the intensity of the outgoing radiation from the layer. The layer has temperature (T), pressure (p), partial pressure (p_{part})

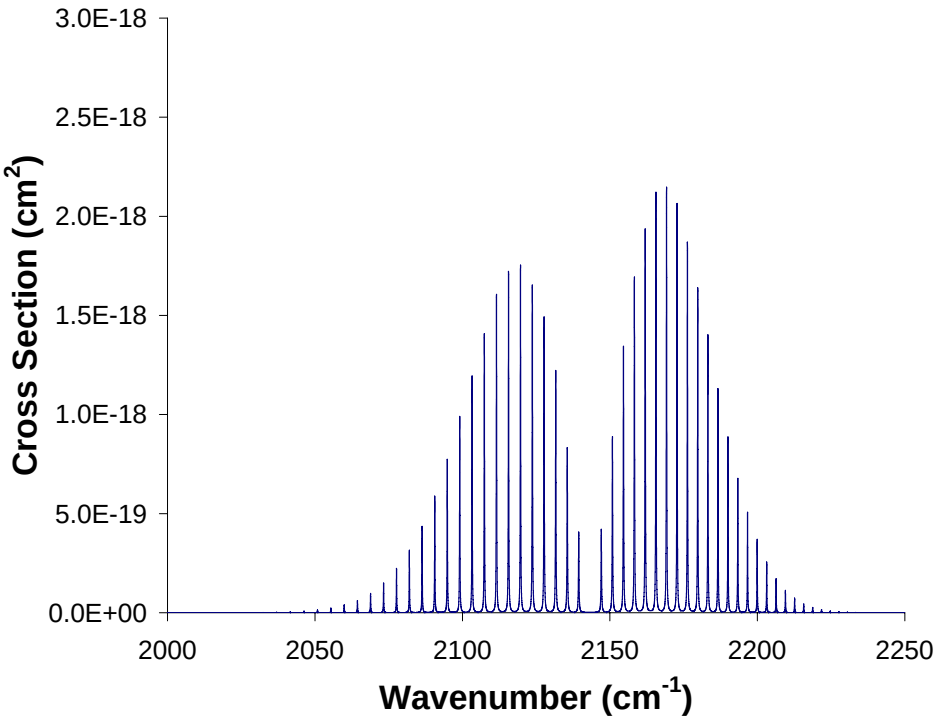

Figure 3.4: A CO R-branch fundamental band (vibrational transition 0-1) cross section spectrum measured at a pressure of 1 atm and a temperature of 200 K. This shows populated rotational states between 2050 and 2230 cm^{-1}.

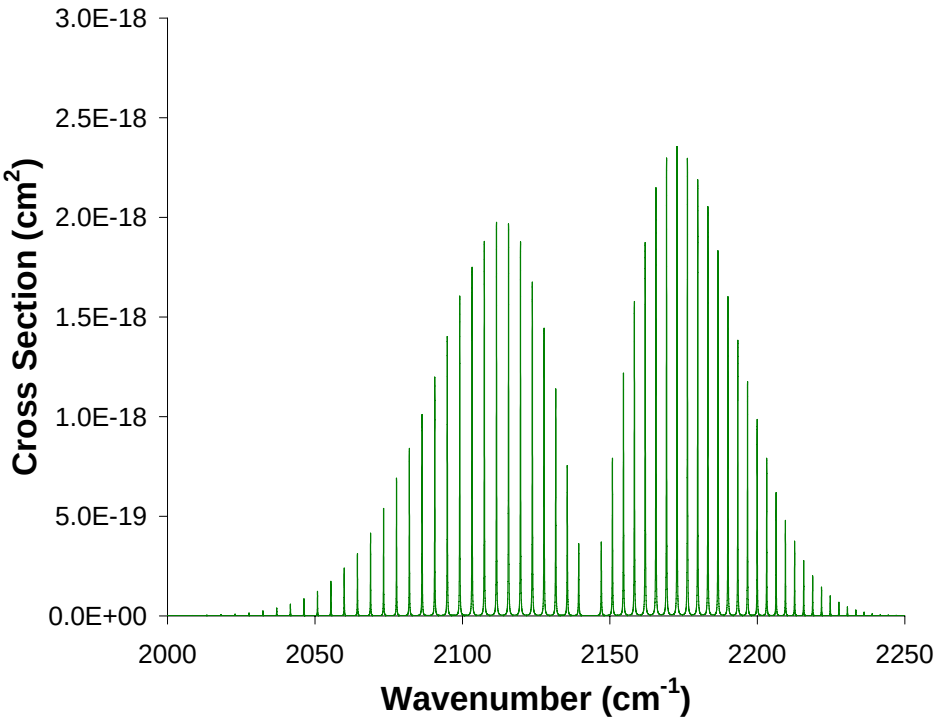

Figure 3.5: A CO R-branch fundamental band (vibrational transition 0-1) cross section spectrum measured at a pressure of 1 atm and a temperature of 300 K. This shows populated rotational states between 2025 and 2250 cm^{-1}.

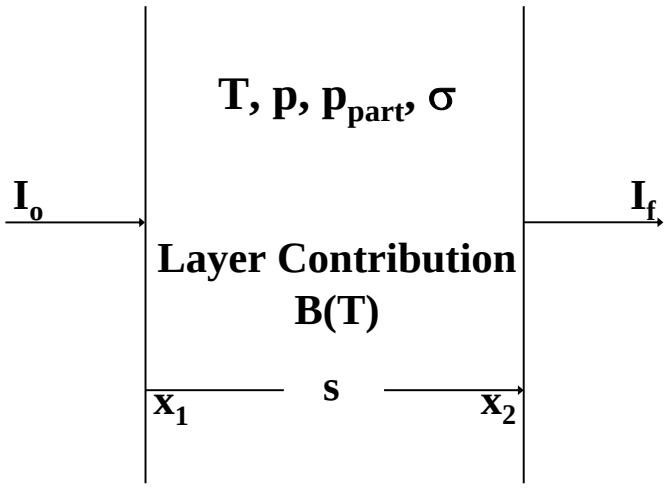

Figure 3.6: A simple diagram of a single homogeneous layer of atmosphere and the variables within the layer that assist in changing the incoming radiance.

due to any minor absorbing species and a thickness Δx. We only consider radiation in one direction as we are ignoring scattering processes.

The total change in the radiation as it traverses is given by the balance of absorption, from Beer's Law and thermal emission, assuming Planck's function and local thermal equilibrium. For an infinitesimal distance, ds, the change in intensity, dI, is given by,

$$\mathrm{d}I = -I\sigma n\mathrm{d}s + B\sigma n\mathrm{d}s. \tag{3.10}$$

Equation 3.10 is known as the Schwarzschild equation. The equation can be integrated for a homogeneous layer,

$$\int_{I_o}^{I_f} \frac{\mathrm{d}I}{I-B} = -\int_{x_1}^{x_2} \sigma n\mathrm{d}s \tag{3.11}$$

$$\ln\left(\frac{I_f - B}{I_o - B}\right) = -\sigma n(x_2 - x_1) = -\sigma n\Delta x = -\tau \tag{3.12}$$

$$I_f = I_o e^{-\tau} + (1 - e^{-\tau})B, \tag{3.13}$$

where τ is known as the optical depth of the layer. Equation 3.13 provides the intensity emerging from a finite, homogenous layer for incoming monochromatic radiation. We have only considered one species in this derivation but additional species are readily included by calculating the total optical depth from the summation of the optical depth of each species.

A computer model was created to produce intensities coming from a single homogenous layer. This model uses as input an arbitrary incident intensity spectrum $I_0(\nu)$, a temperature for the layer, a layer pressure, and species concentration in the layer. The model then uses this information and that contained in the HITRAN database to calculate the outgoing intensity spectrum, $I_f(\nu)$, from the layer at any wavelength resolution. The spectra shown in this section were created with the model where the incident intensity, $I_0(\nu)$, is a Planck function for an arbitrary temperature.

As emission and absorption are occurring simultaneously in the layer the spectrum of the outgoing intensity can appear as an emission or absorption spectrum. Analysis of equation 3.13 indicates that if the layer temperature is equal to the source temperature, or $I_0(T_{source}) = B(T_{layer})$, then $I_f = B = I_0$ at all wavelengths. Also, if $B(T_{layer}) > I_0(T)$ then I_f is always greater than I_0 and similarly if $B(T_{layer}) < I_0(T)$ then I_f is always less than I_0. That is, if the source temperature is greater than the layer temperature radiation is removed from the incident beam and the result appears as an absorption spectrum, and if the source temperature is less than the layer temperature then radiation is added to the beam by the emitting molecules and the outgoing spectrum appears like an emission spectrum.

Figure 3.7 shows both the outgoing absorption spectrum and the incoming source intensity where $T_{layer} = 250$ K and $T_{source} = 300$ K. For this example a small optical depth was used. It is evident that the outgoing spectrum is less intense than the incident spectrum at all wavenumbers and absorption dominates for all transitions. Conversely, Figure 3.8 shows the modelled result where $T_{layer} = 300$ K and $T_{source} = 270$ K. In this figure it is apparent that emission dominates and all transitions add to the intensity of the incident radiation.

A boundary forms in the outgoing intensity when the layer becomes optically thick as τ becomes sufficiently large that $e^{-\tau}$ approaches zero. A lower boundary forms for an absorption spectrum and an upper boundary forms for an emission spectrum. This is seen in equation 3.13 where $e^{-\tau}$ approaches 0 and $I_f = B(T_{layer})$. Figures 3.9 through 3.12 show both the emission and absorption boundaries for the entire spectrum and select lines. Note that the layer is only optically thick at the line centers.

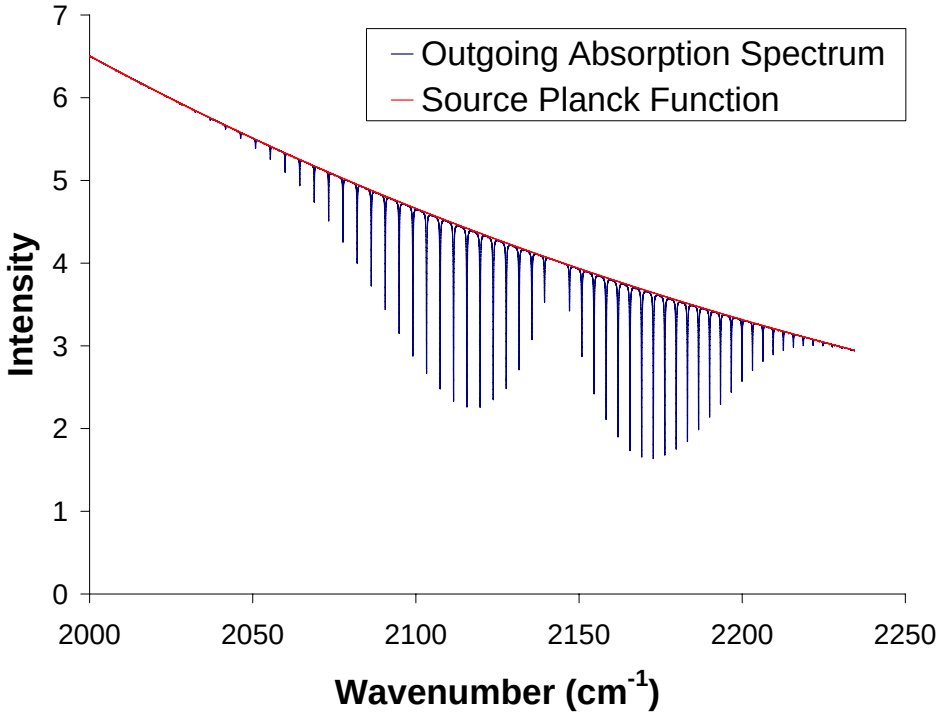

Figure 3.7: An outgoing CO absorption spectrum measured from a surface with temperature of 300 K through a single homogeneous layer with a temperature of 250 K (blue), a pressure of 1 atm and path length of 1.5 km. The Planck function for the surface temperature acts as the upper boundary (red). The intensity along the y-axis has units of ergs/s/cm^2/μm/ster.

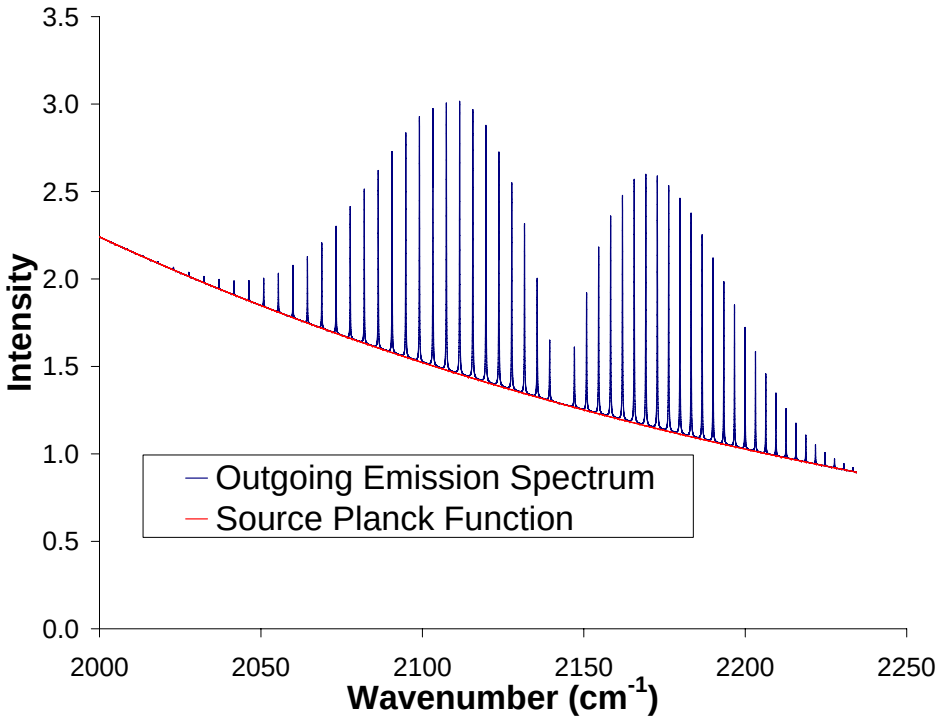

Figure 3.8: An outgoing CO emission spectrum measured from a surface with temperature of 270 K through a single homogeneous layer with a temperature of 300 K (blue), a pressure of 1 atm and a path length of 1.5 km. The Planck function for the surface temperature acts as the lower boundary (red). The intensity along the y-axis has units of ergs/s/cm^2/μm/ster.

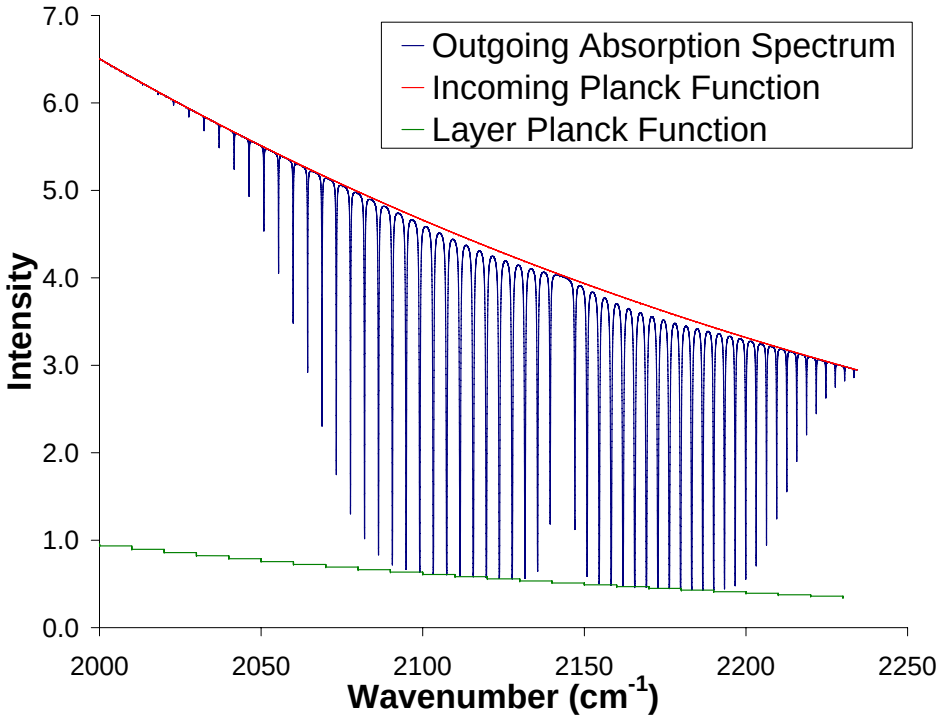

Figure 3.9: An outgoing CO absorption spectrum measured from a surface with temperature of 300 K through a single optically thick layer with a temperature of 250 K (blue), a pressure of 1 atm and a path length of 15km. The Planck function for the surface temperature acts as the upper boundary (red), while the Planck function for the layer temperature acts as the lower boundary (green). The intensity along the y-axis has units of ergs/s/cm^2/μm/ster.

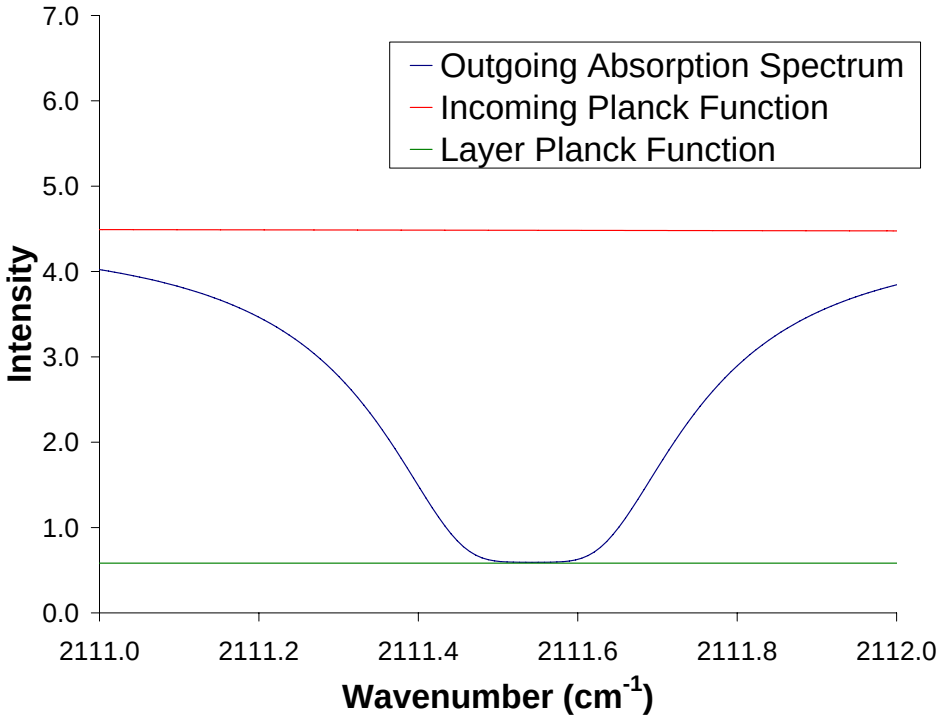

Figure 3.10: An outgoing CO absorption spectral line measured from a surface with temperature of 300 K through a single optically thick layer with a temperature of 250 K (blue), a pressure of 1 atm and a path length of 15 km. The Planck function for the surface temperature acts as the upper boundary (red), while the Planck function for the layer temperature acts as the lower boundary (green). The intensity along the y-axis has units of ergs/s/cm^2/μm/ster.

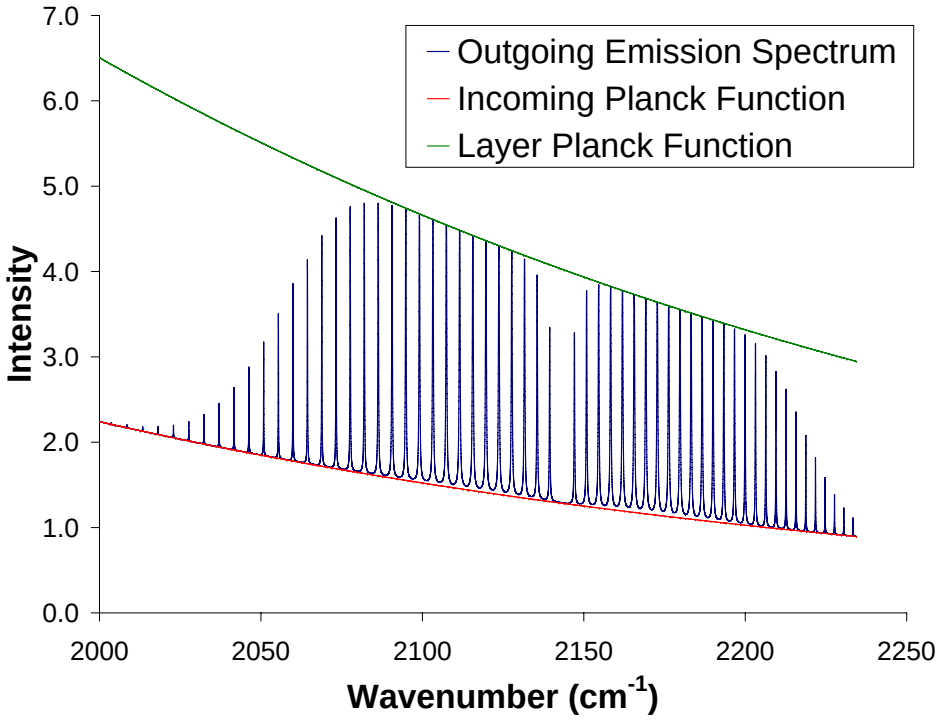

Figure 3.11: An outgoing CO emission spectrum measured from a surface with temperature of 270 K through a single optically thick layer with a temperature of 300 K (blue), a pressure of 1 atm and a path length of 15 km. The Planck function for the surface temperature acts as the lower boundary (red), while the Planck function for the layer temperature acts as the upper boundary (green). The intensity along the y-axis has units of ergs/s/cm^2/μm/ster.

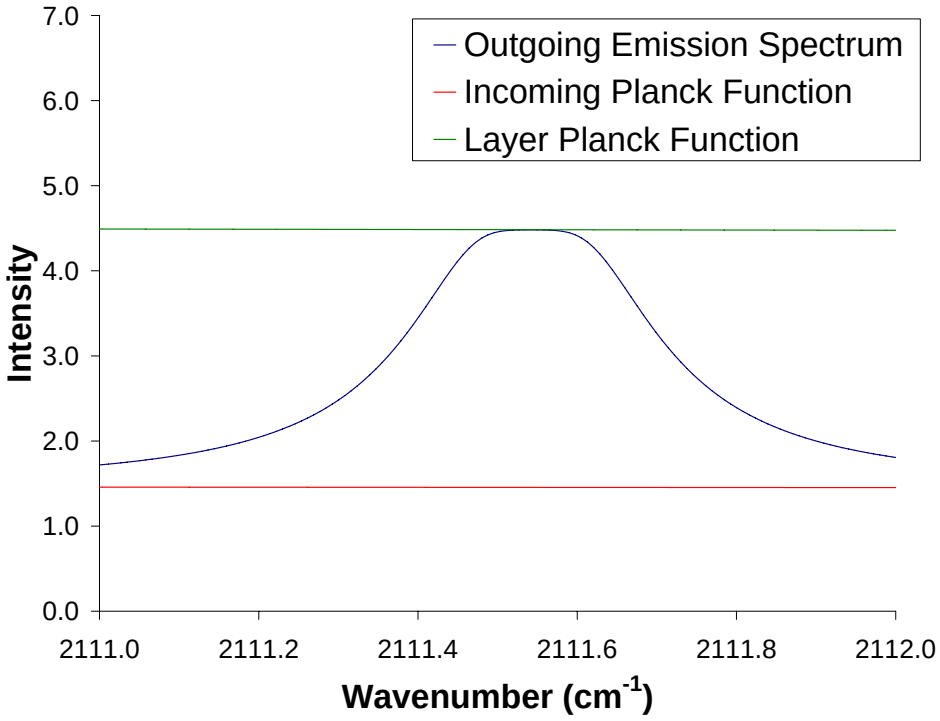

Figure 3.12: An outgoing CO emission spectral line measured from a surface with temperature of 270 K through a single optically thick layer with a temperature of 300 K (blue), a pressure of 1 atm and a path length of 15 km. The Planck function for the surface temperature acts as the lower boundary (red), while the Planck function for the layer temperature acts as the upper boundary (green). The intensity along the y-axis has units of ergs/s/cm^2/μm/ster.

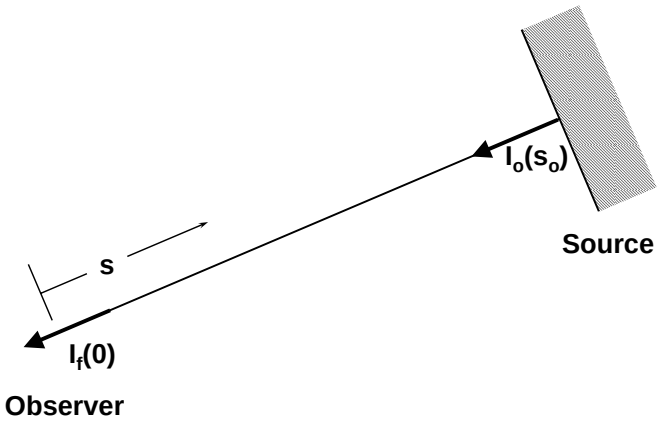

Figure 3.13: This figure describes the geometry used to derive a continuous theorem from the Schwarzschild equation.

3.4 Radiative Transfer in Non-homogenous Media

In the previous work the Schwarzschild equation was integrated to give the intensity emerging from a single homogeneous layer, equation 3.13. However, a vertical profile of the entire troposphere cannot be considered to be homogeneous and this issue must be dealt with.

It is straight forward to integrate the Schwarzschild differential equation for a non-homogenous media. Figure 3.13 shows the geometry used. A black body source at s_0 is glowing at temperature T. The radiation is transmitted through a non-homogeneous atmosphere from s_0 to an observer located at position, $s = 0$. The Schwarzschild equation can be integrated for a continuous atmosphere as,

$$\begin{aligned} \mathrm{d}I &= I(s)\, n(s)\sigma(s)\mathrm{d}s - B(s)n(s)\sigma(s)\, \mathrm{d}s \\ \mathrm{d}I\, e^{-\tau(s)} &= I(s)n(s)\sigma(s)\, \mathrm{d}s\, e^{-\tau(s)} - B(s)n(s)\sigma(s)\mathrm{d}s\, e^{-\tau(s)} \\ I(0) &= I(s_0)\, e^{-\tau(s_0)} + \int_0^{s_0} B(s)n(s)\sigma(s)\, e^{-\tau(s)}\mathrm{d}s. \end{aligned} \tag{3.14}$$

The final equation describes the outgoing intensity through a continuous, non-homogenous medium. The first term on the right hand side represents the attenuation of the radiation from the incoming black body source after it has propagated through an optical depth $\tau(s_0)$. The second term represents the sum of the thermal emissions from each

elemental volume along path appropriately attenuated by the optical depth, $\tau(s)$, as they propagate to the observer.

An alternative approach to solving the radiative transfer in a non-homogenous atmosphere is to break the atmosphere into a stacked series of homogenous layers. The homogenous theory, developed earlier, is then applied to each layer where the output of one layer acts as the input to the next. It is readily demonstrated that a discrete stack of homogenous layers accurately represents the continuous system described above. The outgoing intensity from the first of i layers in a multiple layer system is given by equation 3.13. The intensity through the first layer of a multiple layer system can be written as

$$I_1 = I_0 e^{-\tau_1} + (1 - e^{-\tau_1}) B_1. \tag{3.15}$$

I_1 represents the outgoing intensity from the first layer. This intensity is the incoming intensity to the second layer. Therefore, the outgoing intensity from layer 2 can be written as

$$\begin{aligned} I_2 &= I_1 e^{-\tau_2} + (1 - e^{-\tau_2}) B_2 \\ &= I_0 e^{-\tau_1 - \tau_2} + (1 - e^{-\tau_1}) B_1 e^{-\tau_2} + (1 - e^{-\tau_2}) B_2. \end{aligned} \tag{3.16}$$

Using the same method the outgoing intensity from layer 2 becomes the incoming intensity for layer 3. The result for a three layer system is

$$I_3 = I_0 e^{-\tau_1 - \tau_2 - \tau_3} + (1 - e^{-\tau_1}) B_1 e^{-\tau_2} e^{-\tau_3} + (1 - e^{-\tau_2}) B_2 e^{-\tau_3} + (1 - e^{-\tau_3}) B_3. \tag{3.17}$$

Examination of the above derivation reveals a trend, which leads to a discrete representation of the outgoing intensity from i layers. This representation is given by

$$I_i = I_0 e^{-\sum_{j=1}^{i} \tau_j} + \sum_{j=1}^{i} (1 - e^{-\tau_j}) B_j e^{-\sum_{k=j+1}^{i} \tau_k}. \tag{3.18}$$

The discrete model in equation 3.18 was formulated using the discrete single layer model derived from the Schwarzschild equation. Through a short analysis it can be seen that equation 3.18 is actually a discrete form of the theoretical continuous formula derived from equation 3.14. Comparing the first terms of the two equations,

$$I(s_0) e^{-\tau(s_0)} \Rightarrow I_0 e^{-\sum_{j=1}^{i} \tau_j}, \tag{3.19}$$

the transition to the discrete form is easily recognized. The summation represents the total optical depth from the surface through the top layer. Comparing the second

terms, seen as

$$\int_0^x B(s)\sigma n e^{-\tau(s)}\mathrm{d}s \Rightarrow \sum_{j=1}^{i}(1-e^{-\tau_j})B_j e^{-\sum_{k=j+1}^{i}\tau_k}, \tag{3.20}$$

requires some manipulation to identify the similarity. For path lengths Δx the optical depth is small and

$$(1-e^{-\tau}) = 1-(1-\tau+\frac{\tau^2}{2}-\frac{\tau^3}{6}+...) \approx \tau = \sigma n \mathrm{d}s. \tag{3.21}$$

This is because the higher order terms are comparably very small and may be discarded. This allows the comparison in equation 3.20 to be rewritten as

$$\int_0^x \sigma n \mathrm{d}s B(s) e^{-\tau(s)} \Rightarrow \sum_{j=1}^{i}\sigma_j n_j \Delta x B_j e^{-\sum_{k=j+1}^{i}\tau_k}. \tag{3.22}$$

The two summations indicate that the radiation originating from each layer is attenuated from that layer through to the top of the atmosphere. Therefore, equation 3.18 represents a discrete form of the continuous theory derived from the Schwarzschild equation.

In this work we use the stacked series of homogenous layers to perform all radiative transfer calculations.

3.5 Modelling MOPITT-A Observations

The geometry used for the MOPITT-A instrument is shown in Figure 3.14. The instrument looks downward through a series of homogenous layers at the glowing Earth. Each layer has its own set of parameters apart from the layer thickness, which is the same for all layers. The HITRAN database is used to calculate the absorption cross-section of each species in each layer. The atmospheric state at all altitudes is specified by the MSIS-E-90 climatological database (Picone et al., 2002). The MSIS-E-90 database returns the climatological temperature and pressure at a given latitude, longitude and altitude at any time of year.

A computer model was built that implemented the stacked series of homogenous layers. Input to the model required specification of the the Earth's black body source temperature, as well as temperature, pressure and partial pressure of each species at each level. Once the inputs are specified the model calculates the brightness, $I(s)$, of the Earth's surface and uses successive applications of the single layer theory to calculate the signal observed at the instrument.

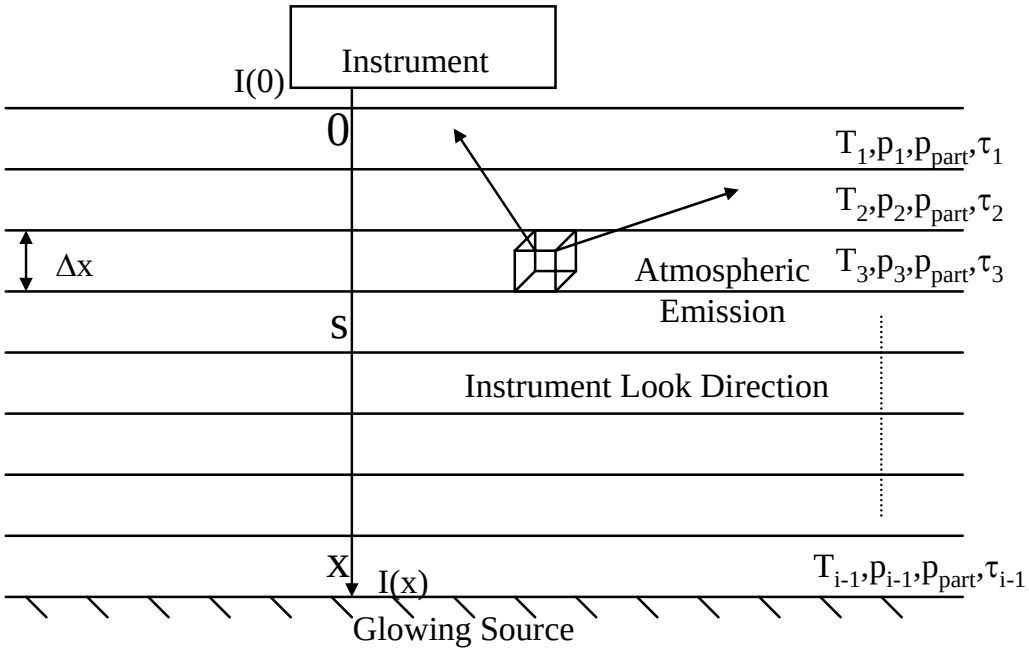

Figure 3.14: Diagram of the MOPITT-A system geometry showing multiple homogeneous layers, emissions from these layers, and absorption of the glowing sources by each layer.

Figure 3.15 shows the calculated signal that would be observed by the instrument. The Earth's surface temperature is greater than the temperature of each atmospheric layer and, as expected, the output spectrum is an absorption spectrum. The upper boundary of this absorption spectrum follows the Planck function for the temperature of the Earth while the lower boundary of the absorption is dictated by the Planck function where the atmosphere becomes optically thick. The lower boundary can be seen explicitly in Figure 3.16.

The radiative transfer theory developed in this section provides a suitable framework to numerically model the radiation field observed by MOPITT-A. The model implements a stacked series of homogenous layers that fully account for absorption and emission within each layer. All scattering processes are ignored as minor.

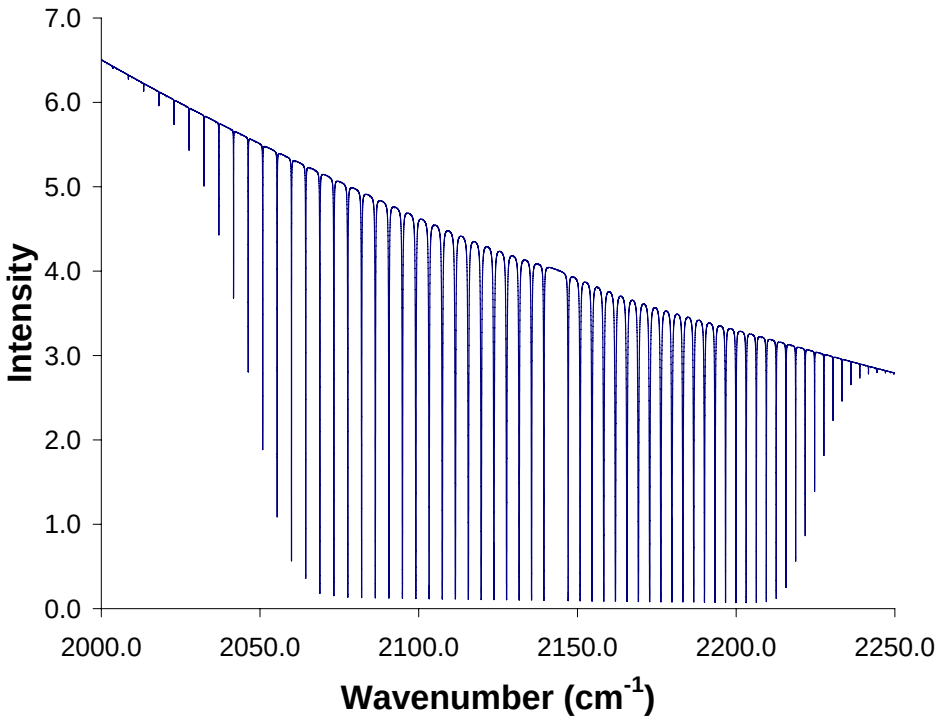

Figure 3.15: An outgoing CO absorption spectrum measured from a surface with a temperature of 300 K through multiple atmospheric layers of different temperatures. The intensity along the y-axis has units of ergs/s/cm^2/μm/ster.

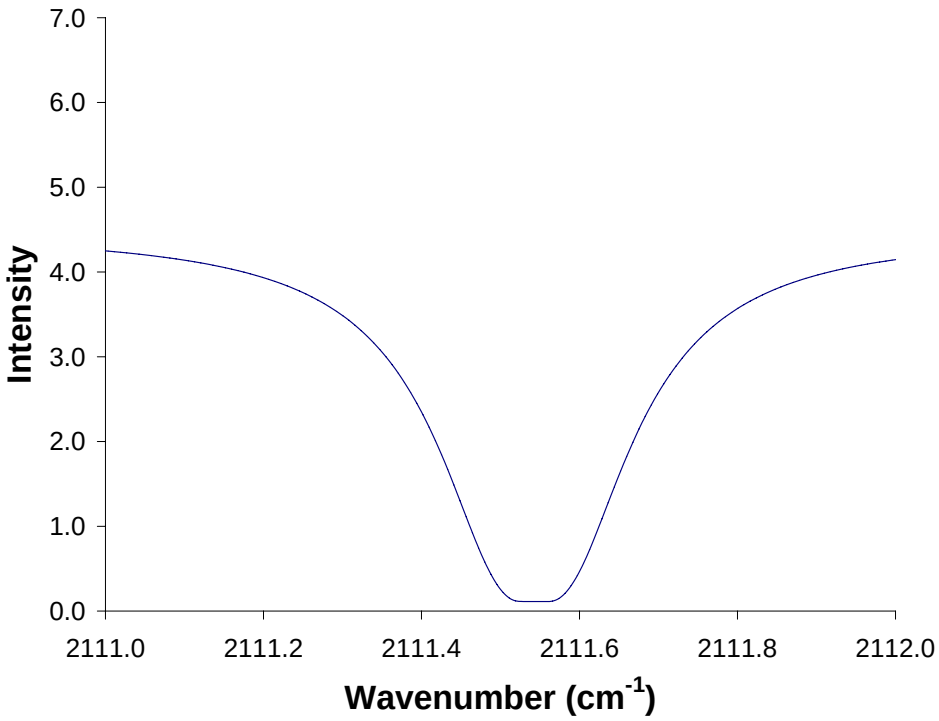

Figure 3.16: An outgoing CO absorption spectral line measured from a surface with a temperature of 300 K through multiple atmospheric layers of different temperatures. The intensity along the y-axis has units of ergs/s/cm^2/μm/ster.

Chapter 4

Correlation Spectroscopy

4.1 Introduction

MOPITT-A records a digital number (DN) representing the band integrated intensity of radiation incident upon the detector. This signal is the result of incident radiation passing through a bandpass filter and gas-cell within MOPITT and subsequent processing by the detector electronics. Given the transmission, $f(\nu)$, of a bandpass filter and the transmission of a single homogeneous layer, equation 3.13, then the recorded digital number can be written as the integral

$$DN = k \int_{\nu} f(\nu) \left[I(\nu) e^{-\tau(\nu)} + B(T_{gas}, \nu)(1 - e^{-\tau(\nu)}) \right] d\nu, \tag{4.1}$$

where $I(\nu)$ is the intensity incident on the MOPITT-A aperture, $\tau(\nu)$ is the optical depth of the gas-cell at wavenumber ν and $B(T_{gas}, \nu)$ is the Planck function evaluated at the gas-cell temperature. The constant, k, is associated with the electronic's gain and is used to convert the signal from radiance to digital number.

4.2 Correlation Spectroscopy Using MOPITT-A

The MOPITT-A system alternates measurements between two values of $\tau(\nu)$ using the *long path* and *short path* gas-cells as well as open and closed states of the optical chopper. The two digital numbers recorded when the shutter is open can be written as,

$$L_O = k \int_{\nu} f(\nu) \left[I(\nu) e^{-\tau_L(\nu)} + B(T_{gas}, \nu)(1 - e^{-\tau_L(\nu)}) \right] d\nu \tag{4.2}$$

and

$$S_O = k \int_\nu f(\nu) \left[I(\nu) e^{-\tau_S(\nu)} + B(T_{gas}, \nu)(1 - e^{-\tau_S(\nu)}) \right] d\nu, \tag{4.3}$$

where L_O is the digital number recorded for the open shutter, *long path* gas-cell, S_O is the digital number recorded for the open shutter, *short path* gas-cell, $\tau_L(\nu)$ is the optical depth of the *long* cell and $\tau_S(\nu)$ is the optical depth of the *short* cell.

Similarly, the two digital numbers recorded when the shutter is closed can be written as,

$$L_C = k \int_\nu f(\nu) \left[0 + B(T_{gas}, \nu)(1 - e^{-\tau_L(\nu)}) \right] d\nu \tag{4.4}$$

and

$$S_C = k \int_\nu f(\nu) \left[0 + B(T_{gas}, \nu)(1 - e^{-\tau_S(\nu)}) \right] d\nu, \tag{4.5}$$

where L_C and S_C are identical to L_O and S_O, respectively, apart from the shutter being in the closed state. The only difference between these equations and the previous two is that the atmospheric source terms has been set to zero as the optical chopper blocks out the atmospheric source in the closed position. The optical chopper is sufficiently small and cold that any thermal radiation emanating from its surface is negligible.

In summary, MOPITT-A measures four data states,

$$\begin{aligned} PathLong, ChopperOpen &\rightarrow L_O \\ PathLong, ChopperClosed &\rightarrow L_C \\ PathShort, ChopperOpen &\rightarrow S_O \\ PathShort, ChopperClosed &\rightarrow S_C. \end{aligned} \tag{4.6}$$

The four states have common terms due to the thermal glow of the gas in each gas-cell, $B(T_{gas}, \nu)(1 - e^{-\tau(\nu)})$. This term can be removed by subtracting the closed chopper signal from the open chopper signal for each gas-cell state,

$$L = L_O - L_C = k \int_\nu I(\nu) \left[f(\nu) e^{-\tau_L(\nu)} \right] d\nu \tag{4.7}$$

and

$$S = S_O - S_C = k \int_\nu I(\nu) \left[f(\nu) e^{-\tau_S(\nu)} \right] d\nu, \tag{4.8}$$

where L and S are the digital numbers in the *long path* and *short path* states solely due to incident atmospheric radiation propagating through the system. Proper analysis of these two, derived, signals enables inferences to be made about the spectral signature

of CO present in the incident atmospheric radiation. The subtraction of L from S results in the *Difference* signal, D, and is written as

$$D = S - L = k \int_{\nu} I(\nu) f(\nu) \left[e^{-\tau_S(\nu)} - e^{-\tau_L(\nu)} \right] d\nu. \tag{4.9}$$

The difference between the L and S signals is due to differences between the optical depth, $\tau_L(\nu)$ and $\tau_S(\nu)$ of the two gas-cell states. For convenience, we refer to the exponent of the optical depth of the *long* cell, $e^{-\tau_L(\nu)}$, as the long filter, F_L, the optical depth of the *short* cell, $e^{-\tau_L(\nu)}$, as the short filter, F_S and the difference of the two as the difference filter, F_D,

$$F_L(\nu) = e^{-\tau_L(\nu)} \tag{4.10}$$

$$F_S(\nu) = e^{-\tau_L(\nu)} \tag{4.11}$$

$$F_D(\nu) = F_S - F_L. \tag{4.12}$$

Finally, we can rewrite the equations for L, S and D using the above filter definitions as,

$$L = k \int_{\nu} I(\nu) f(\nu) F_L(\nu)\, d\nu \tag{4.13}$$

$$S = k \int_{\nu} I(\nu) f(\nu) F_S(\nu)\, d\nu \tag{4.14}$$

$$D = k \int_{\nu} I(\nu) f(\nu) F_D(\nu)\, d\nu. \tag{4.15}$$

Clearly, the behavior of F_L, F_S and F_D are key to interpreting MOPITT-A measurements. Figures 4.1 and 4.2 show both F_L and F_S for an LMC where the gas-cell pressure is 80 kPa and the long and short path-lengths are 2.0 and 0.4 cm, respectively. There is noticeably more absorption due to F_L in the *long* cell at spectral locations near the CO lines but, between the lines, F_L and F_S are essentially the same. This is emphasized when F_D is considered, as shown in Figure 4.3. It is evident that F_D is very low between the spectral lines when compared to the response of both F_L and F_S. When the atmospheric signal is passed through F_D all the information from spectral regions away from the CO lines is removed and this accentuates the importance of the atmospheric radiation that is mostly affected by the CO.

The variation of F_S, F_L and F_D over a narrow spectral range, covering one line, is shown in Figure 4.4, which better shows the differences between F_L and F_S and

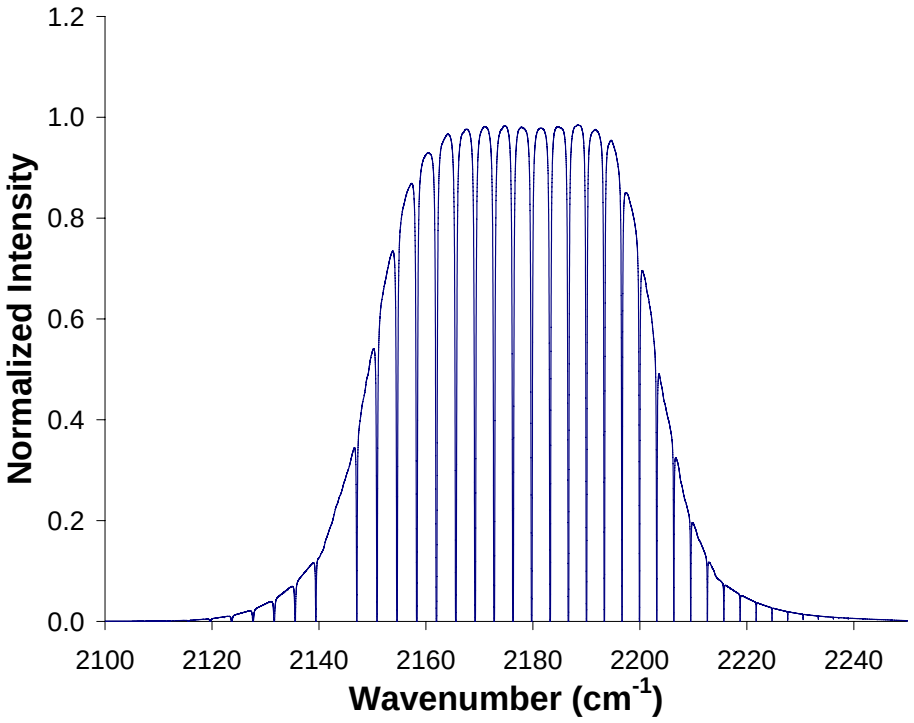

Figure 4.1: The modelled MOPITT-A signal of the LMC long path length state through the channel 5, pixel 1 filter ($f(\nu)e^{\tau_L(\nu)}$).

how these differences contribute to F_D. Both F_L and F_S, and therefore F_D are close to zero near the line center where the absorption is strongest. Outside of the line region both F_L and F_S are non-zero and almost identical, resulting in F_D being very close to zero. The small difference from zero is due to a small remnant absorption which is larger for F_L than F_S.

The essential difference between F_L and F_S is highlighted in Figure 4.4. The value of F_S is significantly higher than F_L in the edges of the lines, resulting in a F_D significantly different from zero. In essence, F_D transmits information relating to the edges of the lines. This is useful because the edges of the lines are the most sensitive to a change in CO concentration.

Rotational spectra of CO for volume mixing ratios (VMR) of 100 ppb and 250 ppb are shown in Figures 4.5 and 4.6, respectively. These signals, which were modelled using the multiple layer radiative transfer model outlined in Section 3.4, represent the signal that would enter MOPITT-A from the atmosphere.

The variation in F_D in a spectral region around a single CO line is shown in Figure 4.7 for the two atmospheric spectra shown in these figures. This comparison

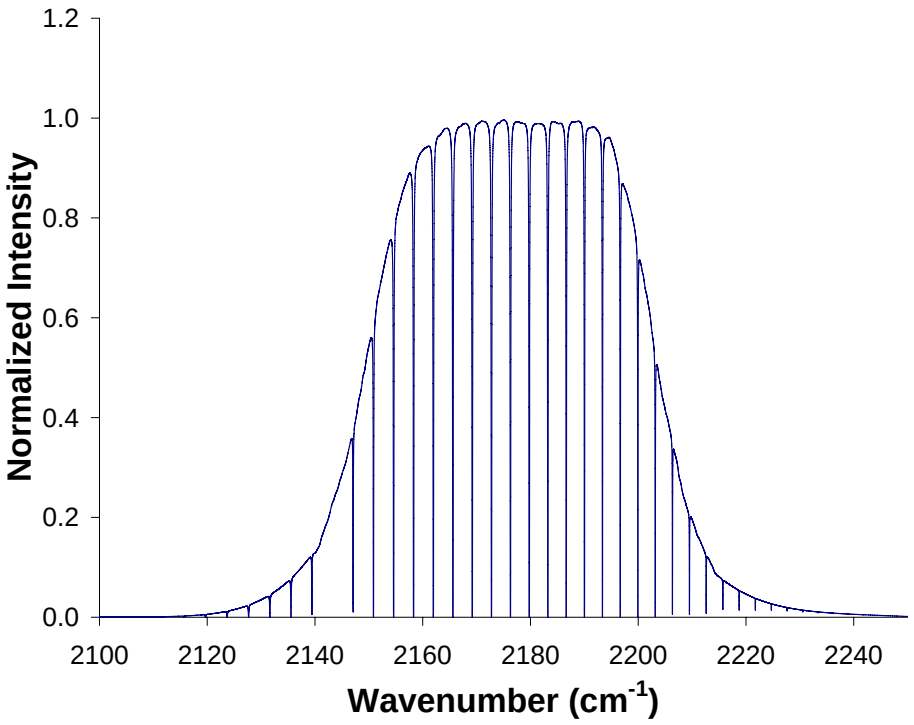

Figure 4.2: The modelled MOPITT-A signal of the LMC short path length state through the channel 5, pixel 1 filter ($f(\nu)e^{\tau_S(\nu)}$).

demonstrates how the correlation spectroscopy technique responds to the two different atmospheric spectra. The F_D was calculated for a gas-cell pressure of 20 kPa. It is quite apparent that the value of F_D is largest in the sides of the lines where the difference between the two atmospheric spectra is largest. Consequently, F_D efficiently transmits information to the difference signal, D, from spectral regions where the two input spectra have significant differences. Thus, MOPITT-A is sensitive to different CO volume mixing ratios present in the atmosphere.

Alternatively, if MOPITT-A did not use the techniques of correlation spectroscopy outlined above but simply employed a bandpass filter then measurements could be written as,

$$O = k \int_{\nu} I(\nu) f(\nu) d\nu \,. \tag{4.16}$$

This would result in a drastic decrease in sensitivity to a change in CO concentration. The reason for this is quite clearly shown in Figure 4.8. In this figure the same two spectral lines as seen in Figure 4.7 are shown with just a simple bandpass filter superimposed upon them. This filter is relatively uniform across the spectral region and does not transmit information preferentially in the spectral regions where

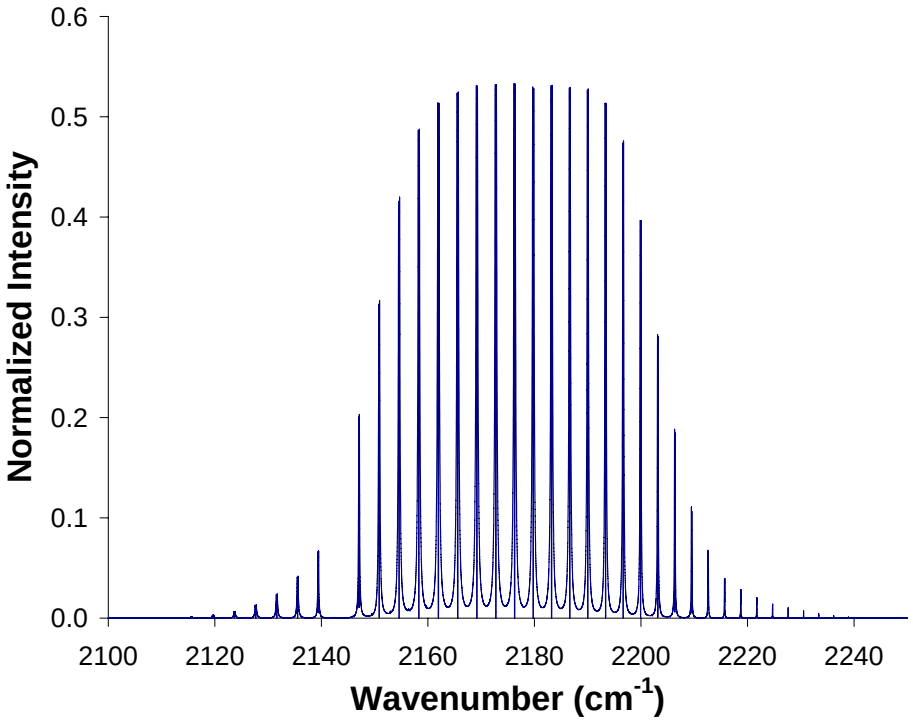

Figure 4.3: The modelled MOPITT-A signal of the difference filter through the channel 5, pixel 1 filter ($f(\nu)[e^{\tau_S(\nu)} - e^{\tau_L(\nu)}]$).

the signals are significantly different. Also, the regions far away from the line centers, where there is no significant CO absorption, are transmitted with exactly the same fractional response as the regions of interest. Measurements made with only a bandpass filter and no correlation cell results in limited rejection of the background signal.

4.3 Gas Pressure in the Length Modulated Cell

The difference signal, D, depends upon the pressure in the gas-cell. Equation 4.9 indicates how the shape of the difference filter weights the contribution of the incident intensity to the difference signal. Different gas-cell pressures result in different F_D shapes and therefore different difference signals. This section details how the wrong choice of gas-cell pressure can significantly decrease the sensitivity of the difference signal to atmospheric CO.

The variations of F_D for 80 kPa and 20 kPa gas-cells in the region of the a CO line are shown in Figure 4.9. The incident spectral line is also shown and all three

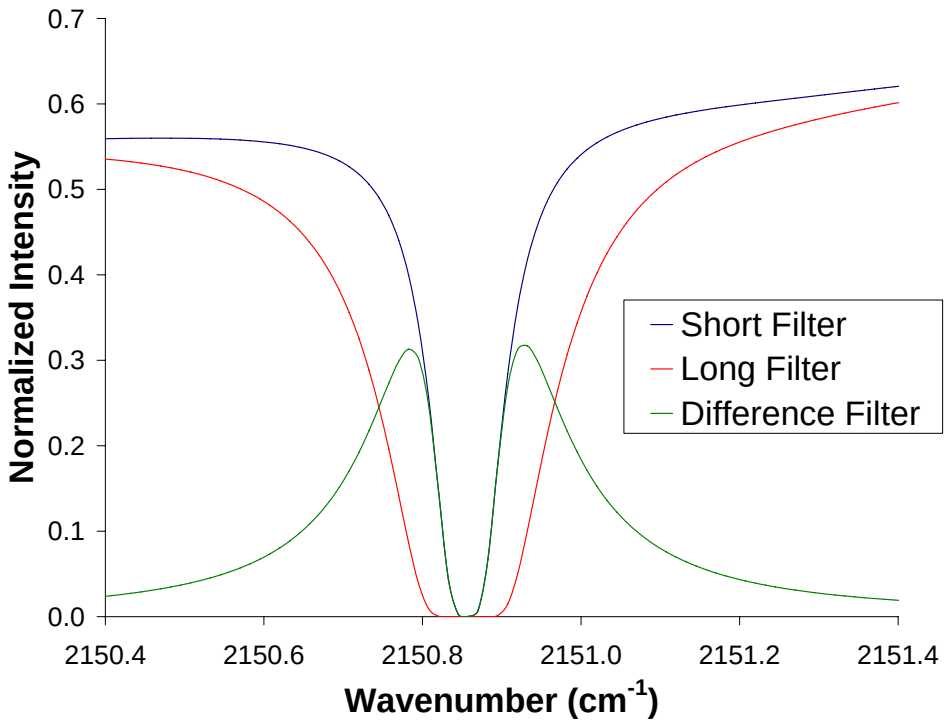

Figure 4.4: Comparison of the short (blue), long (red) and difference (green) filter spectral line centralized at 2150.85 cm^{-1}.

curves are normalized to fit on the same scale. The 20 kPa gas-cell has a F_D similar in width to the input atmospheric line while the F_D for the 80 kPa cell is much wider than the atmospheric line. The F_D for the 80 kPa cell has maximum transmission at wavelengths away from the atmospheric line, resulting in a strong attenuation of, and little sensitivity to, the CO signature in the atmospheric spectrum.

Conversely the F_D of the 20 kPa gas-cell has a width similar to that of the atmospheric line. Therefore, F_D is maximum at wavenumbers near the wings of the line, resulting in maximum sensitivity to changes in CO concentration. It is important to note that this example only pertains to the specific conditions used to generate the incident atmospheric spectra, which was a constant mixing ratio of CO from the ground up to 20 km. In reality, the width of atmospheric CO lines in the incident spectrum are highly dependent on the location of CO within the atmosphere. A large gas-cell pressure, for example 80 kPa, is more appropriate when the bulk of the atmospheric CO is at low altitudes and the incoming spectral lines are significantly broader. Smaller gas-cell pressures are best suited for CO located at higher altitudes where incoming atmospheric lines are narrower. For this reason

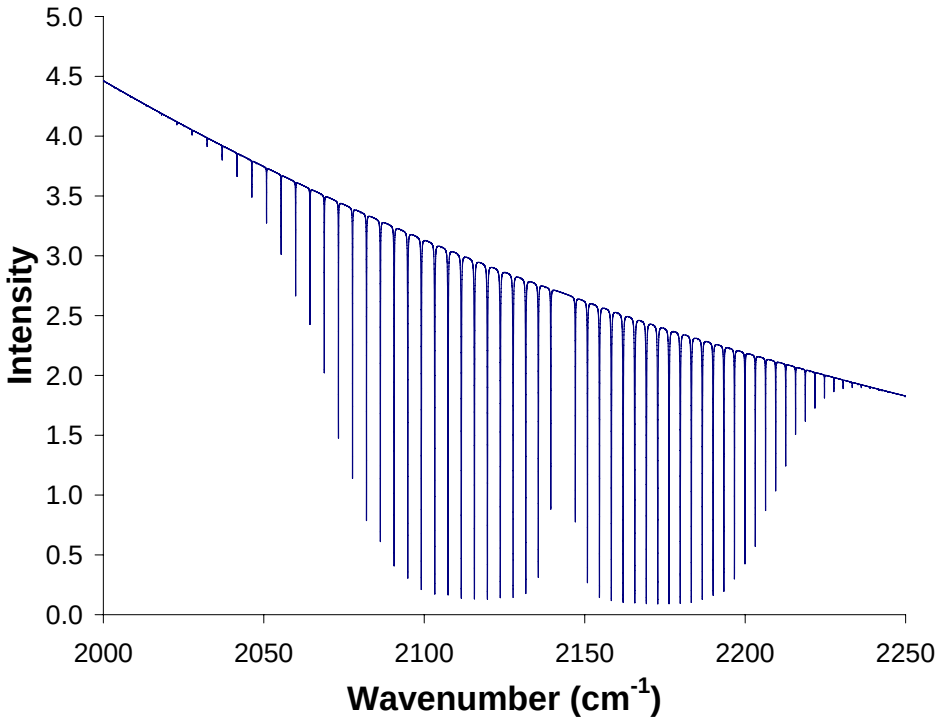

Figure 4.5: A modelled CO signature through a multi-layered atmosphere with a CO volume mixing ratio of 100 ppb and a surface temperature of 300 K. The intensity along the y-axis has units of ergs/s/cm^2/μm/ster.

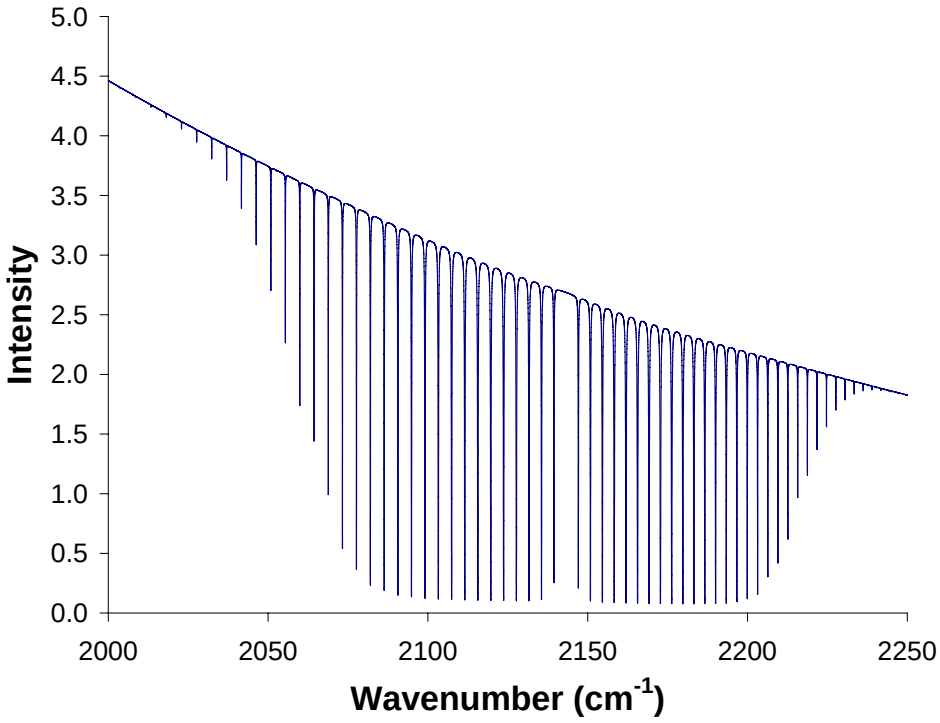

Figure 4.6: A modelled CO signature through a multi-layered atmosphere with a CO volume mixing ratio of 250 ppb and a surface temperature of 300 K. The intensity along the y-axis has units of ergs/s/cm^2/μm/ster.

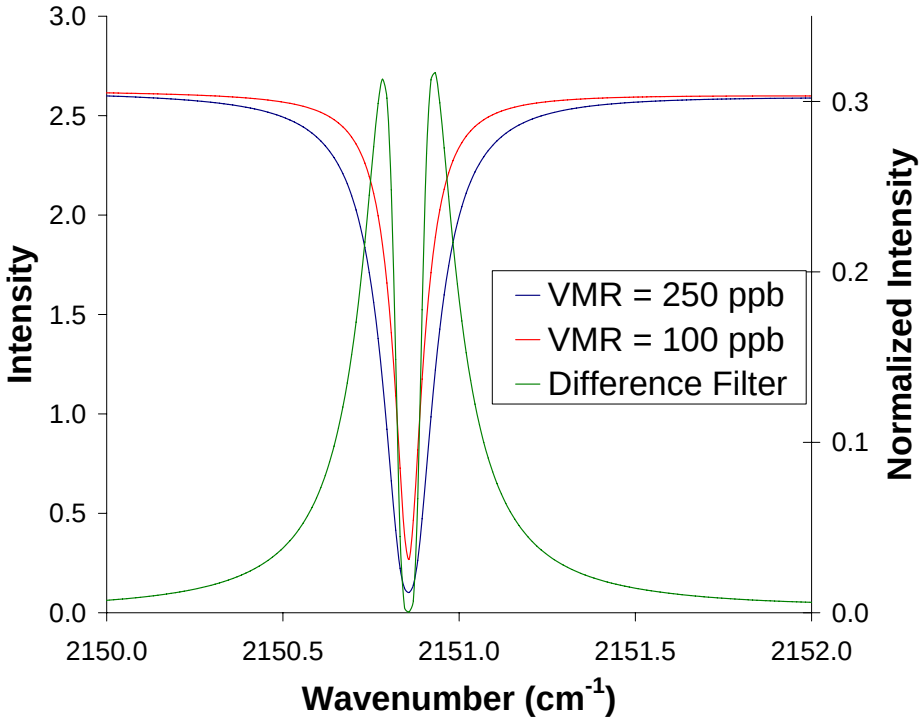

Figure 4.7: A CO spectral line centralized at 2150.85 cm^{-1} through a multi-layered atmosphere with a CO volume mixing ratio of 250 ppb (blue) and 100 ppb (red) compared with the instrument difference filter (green) calculated at a gas-cell pressure of 20 kPa. The intensity along the primary y-axis has units of ergs/s/cm^2/μm/ster.

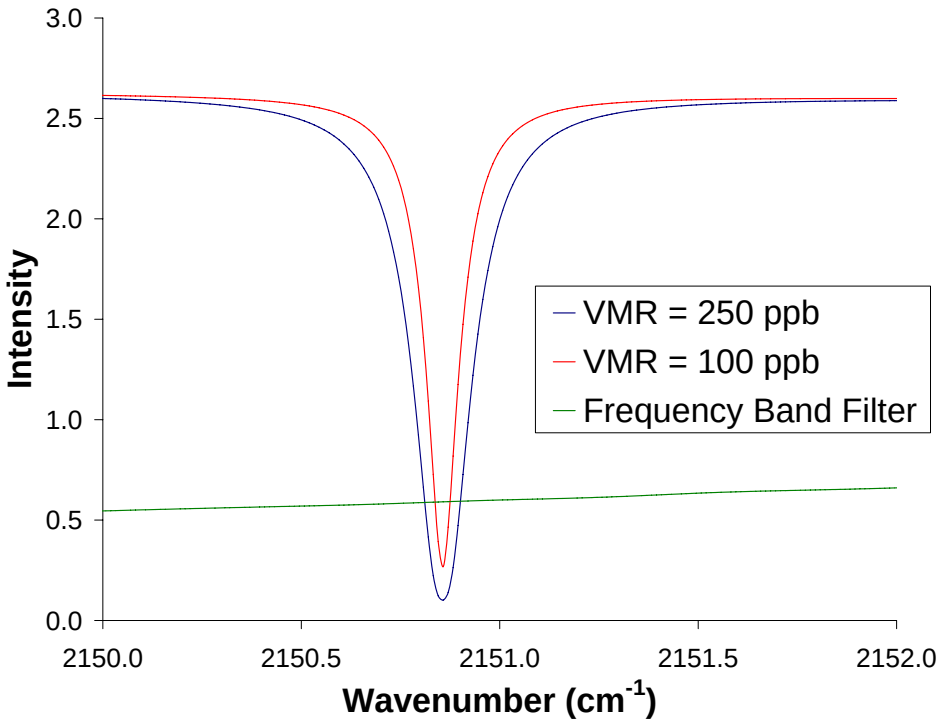

Figure 4.8: A CO spectral line centralized at 2150.85 cm^{-1} through a multi-layered atmosphere with a CO volume mixing ratio of 250 ppb (blue) and 100 ppb (red) compared with the frequency band filter ($f(\nu)$) of channel 5, pixel 1 (green). The intensity along the y-axis has units of ergs/s/cm^2/μm/ster.

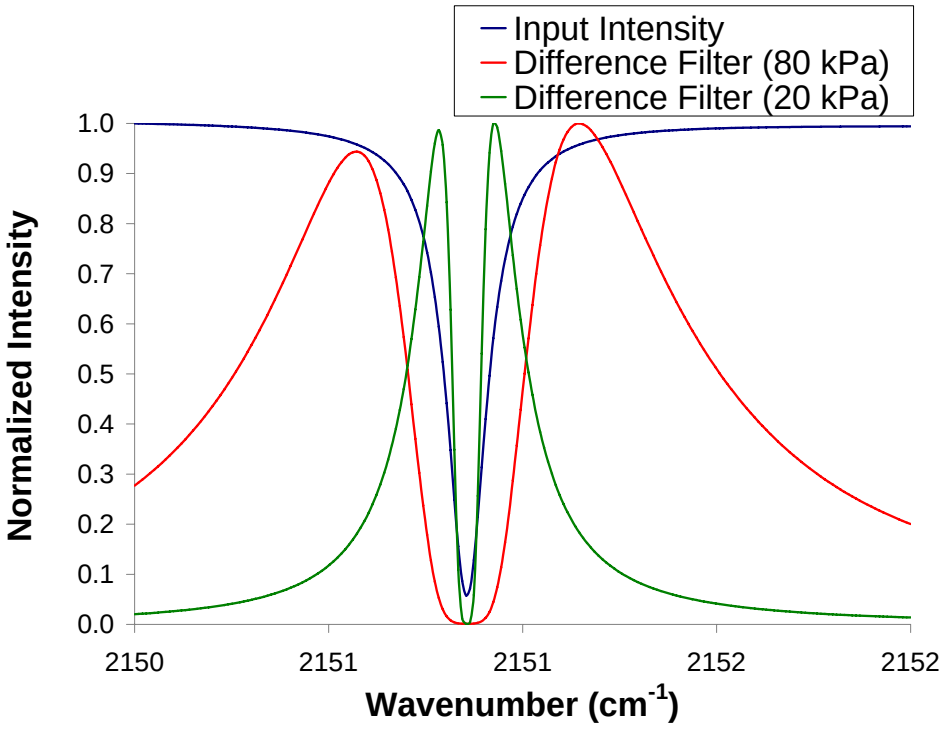

Figure 4.9: Comparison of an atmospheric CO spectral line centralized at 2150.85 cm^{-1} (blue) with the difference filter spectral line modelled at a gas-cell pressure of 80 kPa (red) and 20 kPa (green).

MOPITT and MOPITT-A have several gas-cells with different pressures which are used to preferentially sample CO at different altitudes.

4.4 Sensitivity to an Incorrect Knowledge of the Gas-Cell Pressure and the Gain

This section will demonstrate the importance of having a well calibrated MOPITT-A instrument. It will be shown that even a small error in the knowledge of the gas-cell pressure or the instrument gain could result in a significant error in the determination of the atmospheric CO concentration. A series of simulated incident spectra have been used for this analysis where the CO volume mixing ratio, which is constant at all altitudes, ranges from 100 ppb to 260 ppb in steps of 20 ppb.

Figure 4.10 shows three different curves where the difference signal, D, is modelled for the different volume mixing ratios of atmospheric CO. The middle curve is taken as the control situation, corresponding to a gas-cell pressure of 20 kPa and unity gain. The lower curve has been modelled for a situation where the gas-cell pressure has been decreased by 1% to 19.8 kPa but the gain is constant. Likewise, the upper curve has been evaluated for a situation where the instrument gain increased by 2% to 1.02 but the gas-cell pressure is unchanged.

Now consider the difference signal reported by the three instrument configurations for an atmosphere with a constant CO VMR of 200 ppb. The control configuration will properly report that the difference signal, D, is $1.50E10^{13}$ and correctly interpret this signal as a CO VMR of 200 ppb. However the configuration where the gas-cell pressure was reduced by 1% to 19.8 kPa will report a difference signal of $1.47E10^{13}$. When this difference signal is converted by the control curve to a CO VMR it produces a value of 220 ppb which deviates from the actual VMR by 10%. Similarly the configuration with a gain of 1.02 produces a difference signal of $1.53E10^{13}$ which is interpreted by the control curve as a CO VMR of 185 ppb, or 7% error.

Clearly, the interpretation of MOPITT-A measurements has a significant dependence on good knowledge of the gas-cell pressure and the instrument gain. Small errors in the knowledge of either of these instrument parameters can result in much larger errors in the actual inferred CO concentrations.

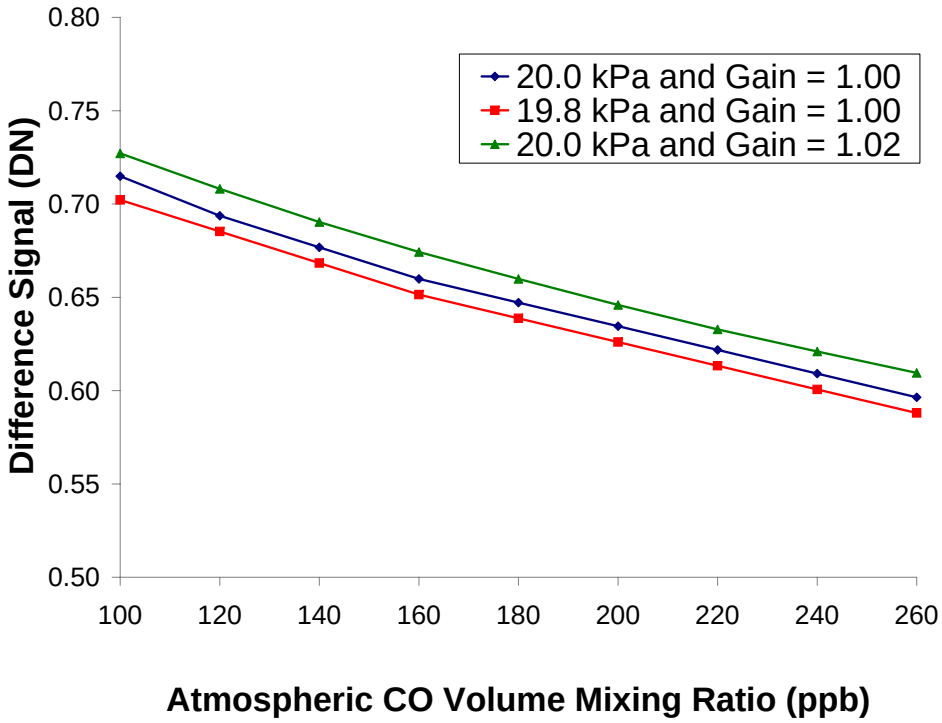

Figure 4.10: Comparison of modelled difference signal values for CO volume mixing ratios from 100 ppb to 260 ppb for slightly varying gas-cell pressures and detector gains to show the sensitivity to change of these parameters.

4.5 Summary

The technique known as correlation spectroscopy requires a set of four well calibrated measurements to accurately infer atmospheric CO concentrations. This technique enhances the CO information contained in the incident spectrum while decreasing the irrelevant background information contained with the spectrum. The significance of exact knowledge of the instrument characteristics was demonstrated in Section 4.4 and it is obvious that a good experimental setup and plan is required to properly validate MOPITT-A measurements.

Chapter 5

Laboratory Setup

5.1 Introduction

It was decided to recreate the MOPITT-A viewing geometry in the laboratory using controlled conditions. Measurements collected under these well known conditions would allow us to test the radiative transfer and correlation spectroscopy outlined in the previous chapters and better our understanding of the instrument's performance. The warm surface of the Earth used in nadir observations was simulated with an external black body source while the column of CO along the line of sight was simulated with an external gas-cell filled with CO.

An Electro Optical Industries Model 2503B Black body was used as the external black body source. This source was programmable and thermally stable between 50 C and 1250 C, permitting temperature adjustment over a large temperature range. The external black body was placed 131 cm from MOPITT-A, which was the largest distance the laboratory would conveniently allow. An aperture size for the black body of 0.508 cm diameter was selected such that the channel 5, pixel 1 output was just under the saturation value, $\sim 5.5 \times 10^6$ DN, when the external black body was at a temperature of 600C and aligned with the center of channel 5, pixel 1. A manual shutter system was built for the external black body which allowed the radiation from the black body to be blocked. The shutter was constructed out of aluminium, painted black and kept at the ambient room temperature. Care was taken to ensure that the shutter was not heated significantly when placed in front of the black body source.

The external black body was attached to a lab-jack which was secured between

two rails attached to the top of a solid table. The two rails permitted the black body to be moved horizontally, perpendicular to the MOPITT-A line of sight while the lab-jack permitted vertical movement. These two degrees of freedom allowed the external black body to be accurately aligned with the optical axis of individual detector pixels of MOPITT-A, as described below. A meter rule, which was physically attached to the rails, permitted the relative position of the external black body to be determined to better than 1 mm. The external black body setup is illustrated in Figures 5.2 and 5.3.

The external gas-cell was a sealed, hollow glass cylinder, 11.1 cm long and 15.2 cm in diameter. This gas-cell has CaF_2 optical windows and was sufficiently wide to cover the field of view of the channel 5 baffle. It was connected to a stand which was attached to the MOPITT-A instrument, as shown in Figure 5.1. A pumping station was connected to the external gas-cell which was was used to evacuate, purge or fill the cell with CO gas.

The pumping station consisted of a roughing pump, pressure transducer and gas tree connected to CO and nitrogen gas (N_2) tanks. The roughing pump, which was a Franklin Electronics Model 1101006418, was used to evacuate the detector nest, external gas-cell and LMC. The pressure transducer was an Omegadyne PX5500 Series connected to a stabilized 12 VDC power source and had a pressure range of 0-1 atm. The CO used in the external gas-cell and LMC was supplied by Matheson Gas and was guaranteed to be 99.99% pure.

The same external mirror, as used on the Golden B.C. campaign, was attached to MOPITT-A to permit illumination from a horizontal direction rather than the nadir direction normally required by the instrument.

5.2 Optics Alignment and Pixel Field of View

The ability to move the external black body in two dimensions perpendicular to the MOPITT-A line of sight permitted the shape and size of the 4 detector pixels in channel 5 to be mapped.

The external black body was set to a temperature of 500 C and allowed to stabilize. The approximate edges of the field of view of each pixel were quickly determined using visual feedback from the output displayed on the Instrument Control Computer monitor. The external black body was placed at the far edge of the field of view of

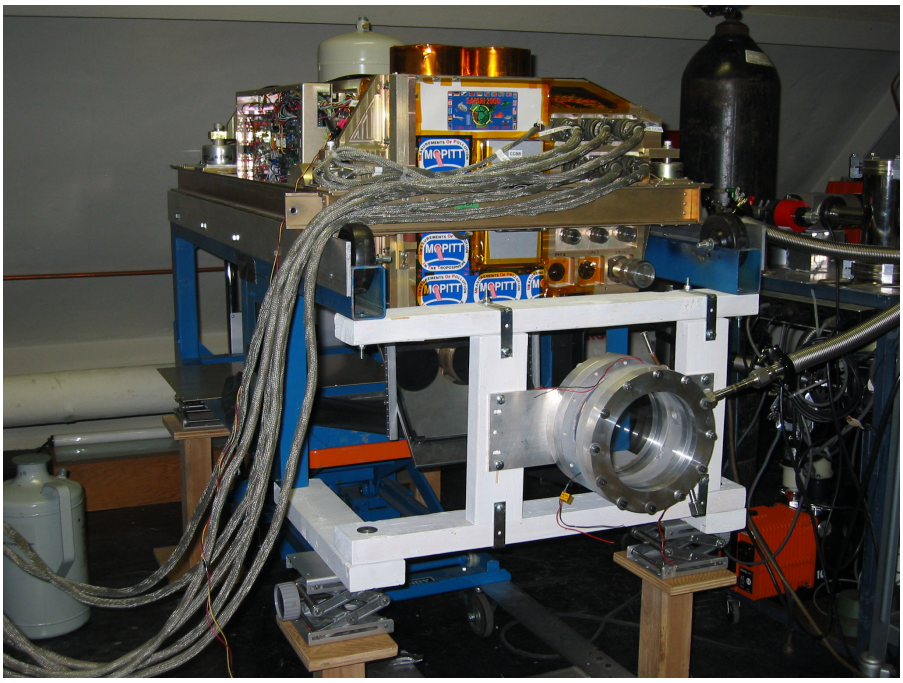

Figure 5.1: The MOPITT-A instrument in the ISAS Optics Laboratory with the external gas-cell shown attached to the front end of the system.

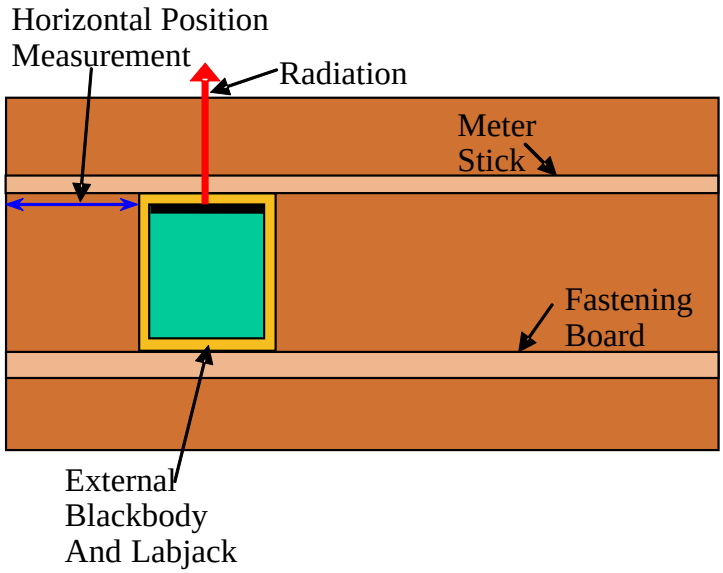

Figure 5.2: Top view of the laboratory set up of the external black body used as the source term for the experiments conducted.

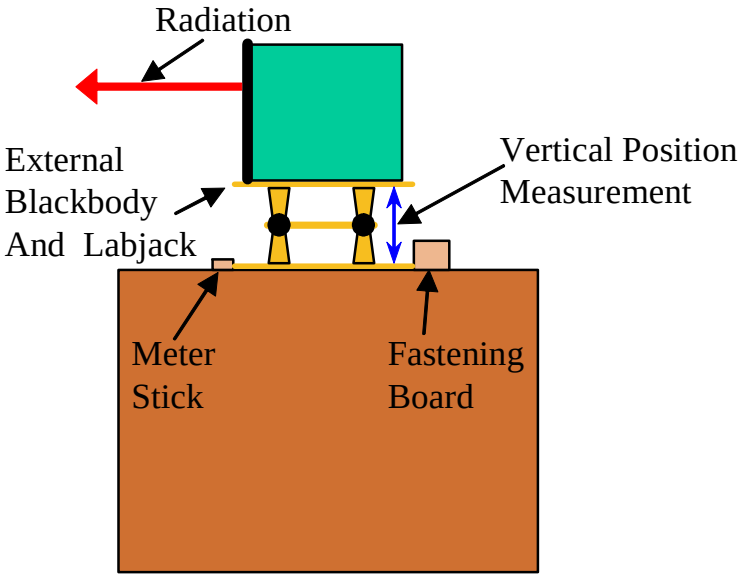

Figure 5.3: Side view of the laboratory set up of the external black body used as the source term for the calibration experiments.

MOPITT-A and the position noted. The external black body was moved horizontally through the field of view until the far edge of the pixel was found and the new position noted. The average of these two positions produced the approximate horizontal coordinate of the center of the pixel. The same procedure was applied to the vertical motion and provided the approximate vertical coordinate of the pixel center. The position of each pixel with respect to the vertical and horizontal positions of the external black body can be seen in Figure 5.4. Note that pixel 1 was mapped more extensively than the other pixels.

Detailed horizontal and vertical scans of channel 5, pixel 1, were performed. The external black body was scanned in the horizontal direction in steps of 0.5 cm along the rail system and 0.5 cm in the vertical direction. Data were collected for one minute at each position with the external black body shutter open and closed, and the difference between the two calculated. The results are shown in Figures 5.5 and 5.6, respectively. The center of channel 5, pixel 1 was at position 22.5 cm in the horizontal direction and 14.0 cm in the vertical.

It was determined from this data that the field of view of channel 5, pixel 1 mapped to a size of 7.5×7.5 cm in our metered rail system. Given that the external black body was 131 cm from MOPITT-A then the channel 5, pixel 1 field of view

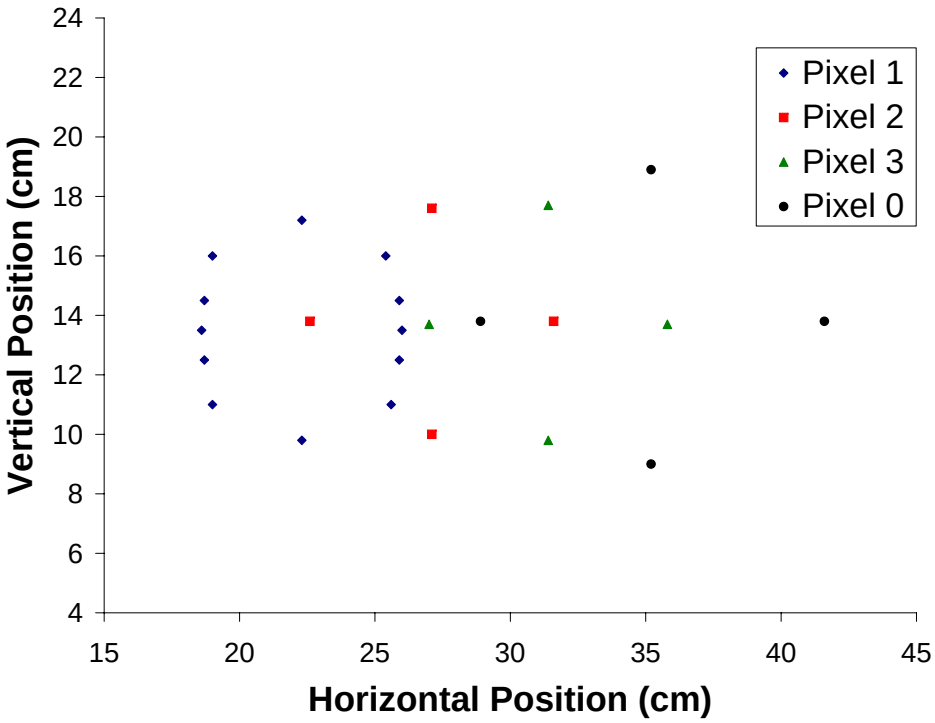

Figure 5.4: Positions of pixel 1 (blue), pixel 2 (red), pixel 3 (green) and pixel 0 (black) of channel 5 determined with respect to the vertical and horizontal position of the external black body.

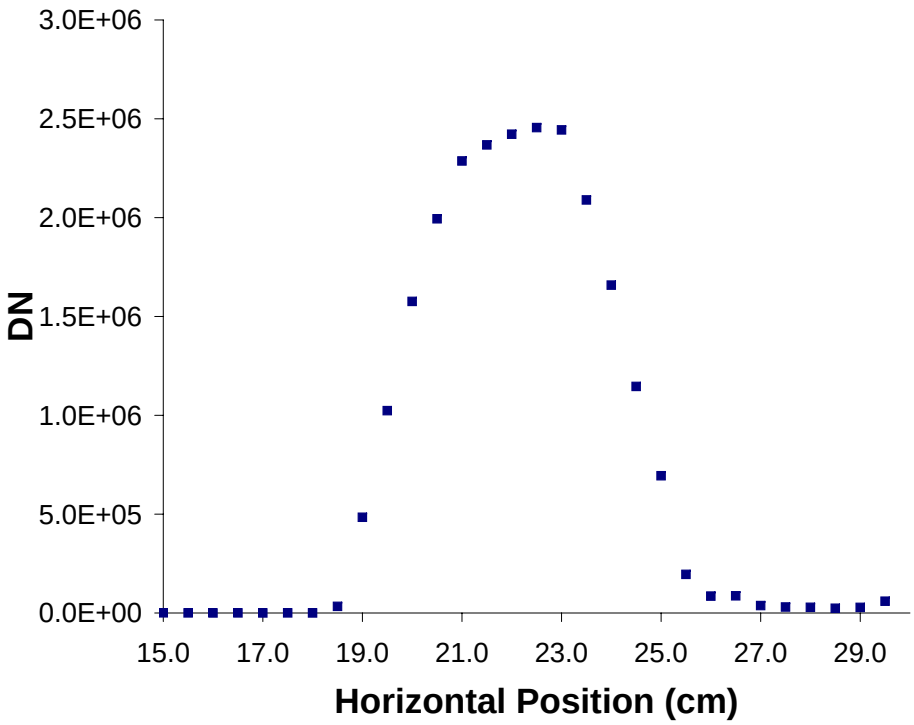

Figure 5.5: Measured horizontal cross section of pixel 1 on channel 5 with respect to the external black body. This was used to determine the central horizontal point of pixel 1.

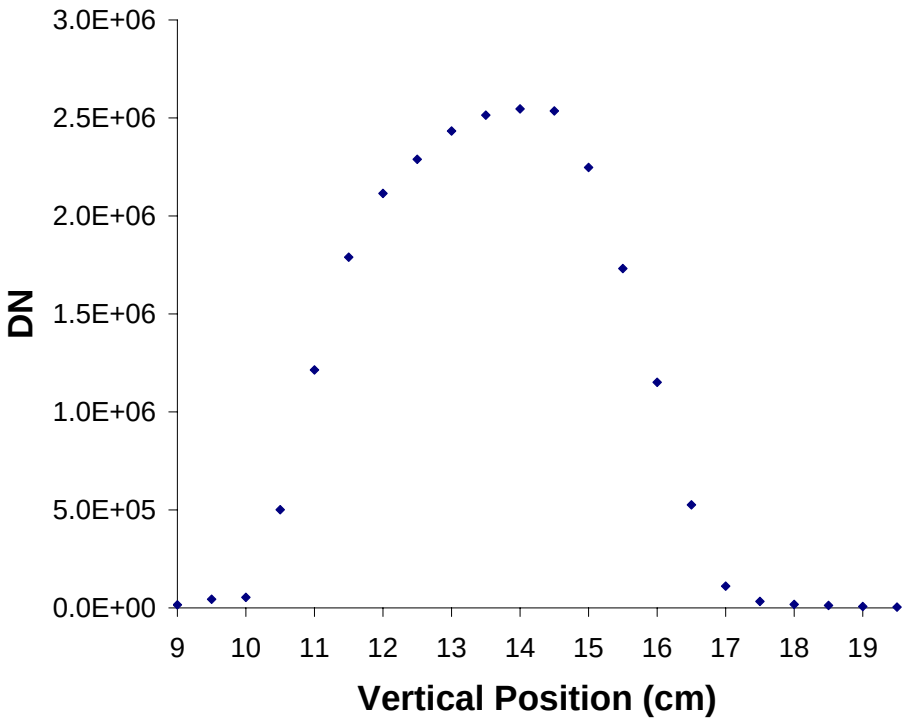

Figure 5.6: Measured vertical cross section of pixel 1 on channel 5 with respect to the external black body. This was used to determine the central vertical point of pixel 1.

is $1.64^\circ \times 1.64^\circ$. It is useful to note, at this time, that the external black body is a good approximation to a point source irradiance in this configuration. The area of the external black body circular aperture was 0.203 cm^2 while the area of the pixel in the metered rail system is 44.18 cm^2. Consequently the external black body only filled 0.46% of the field of view of pixel 1.

5.3 Calibration of The Pressure Transducer

The pumping station included an Omegadyne PX5500 pressure transducer to measure the pressure in either the LMC or the external gas-cell. While the transducer provides a quick and convenient way to monitor pressure in these components, it became evident that the device had significantly drifted away from its manufactured calibration specification. Consequently, the pressure transducer was calibrated against a mercury manometer. The manometer was connected to the same gas tree as the pressure transducer and both were evacuated. Air was slowly leaked into the system and readings taken from both the manometer and pressure transducer until the system reached atmospheric pressure. The difference in the right and left side of the Hg gauge, read from an attached meter stick, gave the correct pressure for each voltage read off the pressure transducer.

The measured calibration curve, as well as the manufacturer's calibration curve, are shown in Figure 5.7. Fitting a straight line to the data gave the following relationship,

$$V = 0.0064p + 0.3776, \tag{5.1}$$

where V is the voltage of the pressure transducer in volts, p is the pressure in torr. The manufacturer's nominal curve was,

$$V = 0.0064p + 0.0126. \tag{5.2}$$

This strongly suggests there was a constant offset voltage between the voltage predicted from the manufacturer's curve and the one measured with our sensor. Such a voltage might be caused by an additional unidentified resistance element somewhere within the pressure transducer. The transducer was occasionally checked against the mercury manometer but did not show any further variation with time.

The error in the voltage measurements from the pressure transducer was ± 0.003 V and the error in the manometer reading was ± 1.0 torr. These error bars are too

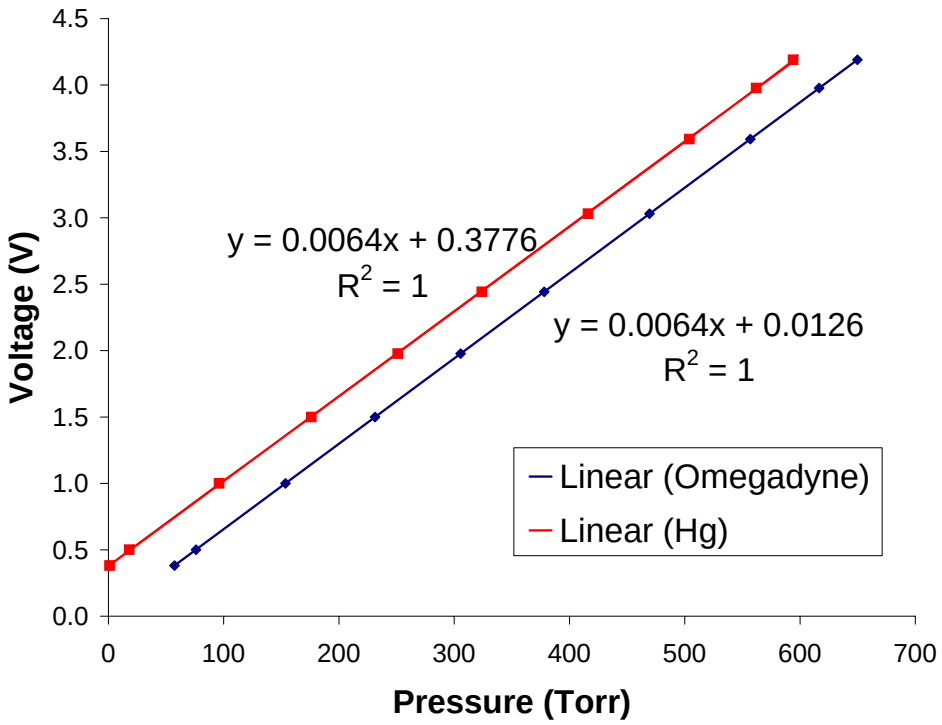

Figure 5.7: Comparison of the Omegadyne manufacturer calibration curve (blue) with the calibration curve determined in the laboratory (red) showing the pressure transducers change in response.

small to be seen in Figure 5.7. The resulting error of the fitted slope, m, was 0.00006 (0.94%). With the error of the response curve slope known, the error in the pressure could be determined from the response curve equation as

$$p = \frac{V - y_{int}}{m} \tag{5.3}$$

$$\Delta p = \frac{\Delta V}{m} + \frac{\Delta m(V - y_{int})}{m^2}, \tag{5.4}$$

where p is the pressure, V is the pressure transducer voltage, m is the slope of the response curve and y_{int} is the y-intercept of the response curve. Therefore, equation 5.4 can be written as,

$$\Delta p = 1.46484V - 0.08437. \tag{5.5}$$

This equation was used to determined the error in the pressure transducer measurements.

5.3.1 Ambient Thermal Radiation

The external black body only illuminates a small fraction of the MOPITT-A field of view. The remainder of the field of view is illuminated by the ambient thermal radiation present in the room. This contaminant signal can be readily detected by the MOPITT-A instrument and its behavior described. The external black body was centered on pixel 1, channel 5, turned off and allowed to reach ambient room temperature. A time sequence of measurements were collected for ~ 9 hours where the only source of illumination was the ambient thermal emission. The time series is shown in Figure 5.8. It is clearly seen that the ambient signal exhibits a 2.5% fluctuation from $\sim$ 2.37E10^6 DN to 2.43E10^6 DN with a periodicity of $\sim 1\frac{1}{2}$ hours.

The variation of MOPITT-A ambient signal with ambient room temperature is shown in Figure 5.9. It is readily evident that, as expected, the ambient thermal emission measured by MOPITT-A is well correlated with ambient room temperature, which is controlled by a standard air conditioning unit. There is significant hysteresis in the relationship suggesting slight time lags between the temperature variation of the thermistor measuring ambient room temperature and the primary sources of ambient thermal emission, e.g. the walls. The bottom half of the hysteresis curve contains points for increasing room temperature while the upper half contains points for a decreasing room temperature.

The signal due to ambient thermal emission was continuously monitored using the manual shutter attached to the external black body. When the shutter was

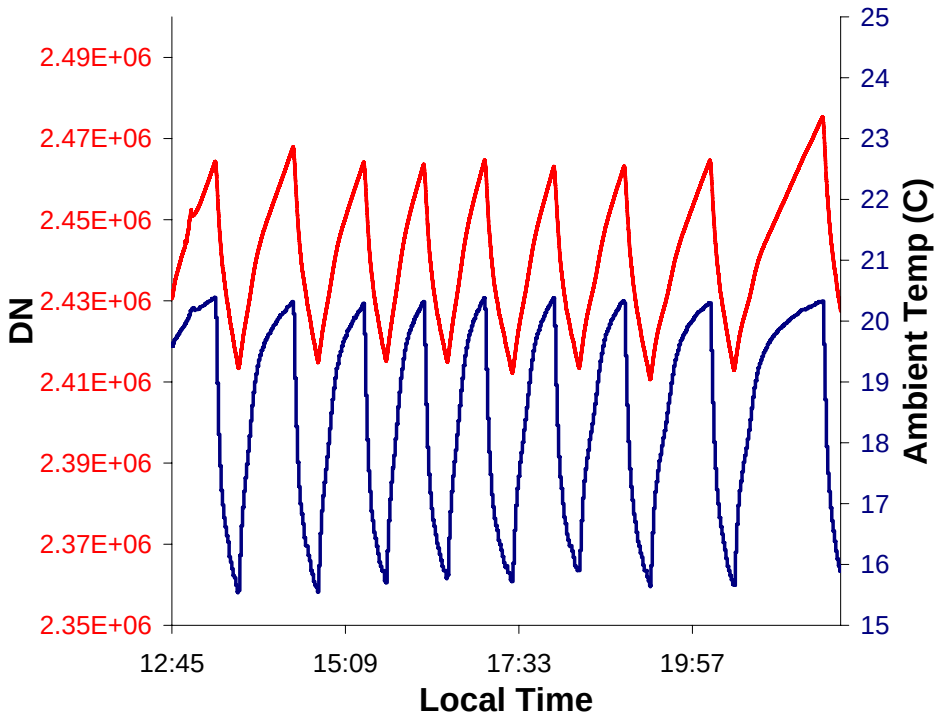

Figure 5.8: Comparison of the MOPITT-A measured background signal (red) and the optical laboratory ambient temperature (blue) to show the sensitivity of the measured signal to fluctuations in the surrounding temperature.

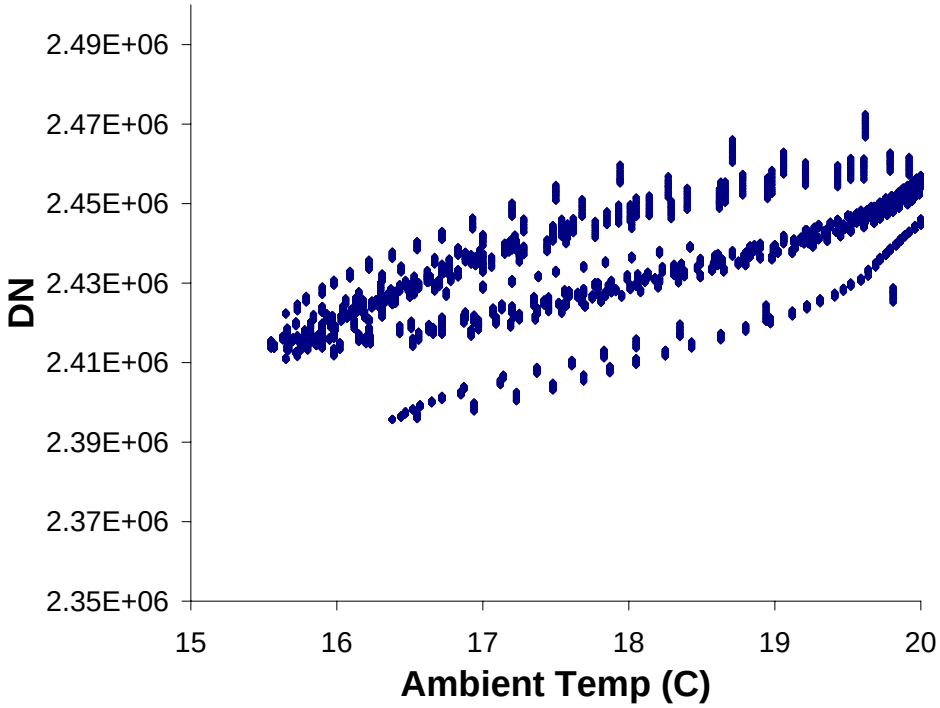

Figure 5.9: A hysteresis effect shown through comparison of the measured background signal with respect to the background temperature.

open, MOPITT-A observed signals from both the external black body which was an approximate point source, and the ambient thermal emission over the entire field of view. When the shutter was closed, MOPITT-A only observed radiation from the ambient thermal emission. The system normally alternated between external black body shutter open and shutter closed states in under two minutes, significantly shorter than the natural fluctuations in ambient emissions.

5.4 Data Reduction

A typical time series of raw, unprocessed MOPITT-A signals is shown in Figure 5.10. These data were collected on the afternoon of October 12, 2004 with a pressure of 60 kPa of CO in the LMC and 0 kPa in the external gas-cell. The external black body was stepped in 25 C increments from 150 C to 500 C over a period of three hours. Four separate curves can be identified in the figure that correspond to four different configurations of the instrument.

The lowest curve, curve 1, are measurements collected with the MOPITT-A chop-

per in the closed position. In this position no external radiation is allowed through the system. Ideally the output would be zero under these conditions but, in reality, internal thermal glow from the instrument and DC biases within the detector electronics produce a significant offset in the signal.

The second lowest curve, curve 2, are measurements collected with the MOPITT-A chopper open but the external black body shutter closed. In this configuration the MOPITT-A aperture is illuminated with ambient incident thermal radiation from the surrounding walls. The difference between curve 2 and curve 1 is a direct measure of the amount of ambient radiation passing through the system.

Curves 3 and 4 are measurements collected when the MOPITT-A chopper is open and the external black body shutter is open. The steady increases in measured signal correspond to steady increases in temperature of the external black body. The difference between these curves and curve 2 is a direct measure of the radiation passing through the system due to the external black body. There are a few points that are outliers to any of the 4 curves and these correspond to measurements collected while the external black body shutter was in transition between open and closed states.

The data reduction followed the outline described earlier in Chapter 4. Raw data are converted to long-path, L, and short-path, S, signals by subtracting the closed shutter signal from the open shutter signals, as seen in equations 4.7 and 4.8. A nearest neighbor technique was used to interpolate the closed shutter signals to the time of the open shutter signals, which introduces minimal error as we collect several measurements of each data set per second. The three curves derived from the analysis of the above data are shown in Figure 5.11, which for all intents and purposes are essentially the same as the raw data except for removal of a slowly varying, baseline offset.

The next stage of analysis produces a difference signal, D, by subtracting the long-path measurements from the short-path measurements, as seen in equation 4.9. Again, a nearest neighbor approach has been used to interpolate the data sets. The difference signal produced from the above data sets is shown in Figure 5.12. The lowest curve on this figure, which corresponds to the difference signal due to ambient radiation in the room, is not exactly zero, going slightly negative at times. This creates a paradox, if interpreted literally, as it requires the optical depth of the short path to be longer than the optical depth of the long path. It is assumed that the negative result is due to systematic effects within the system that are not yet fully

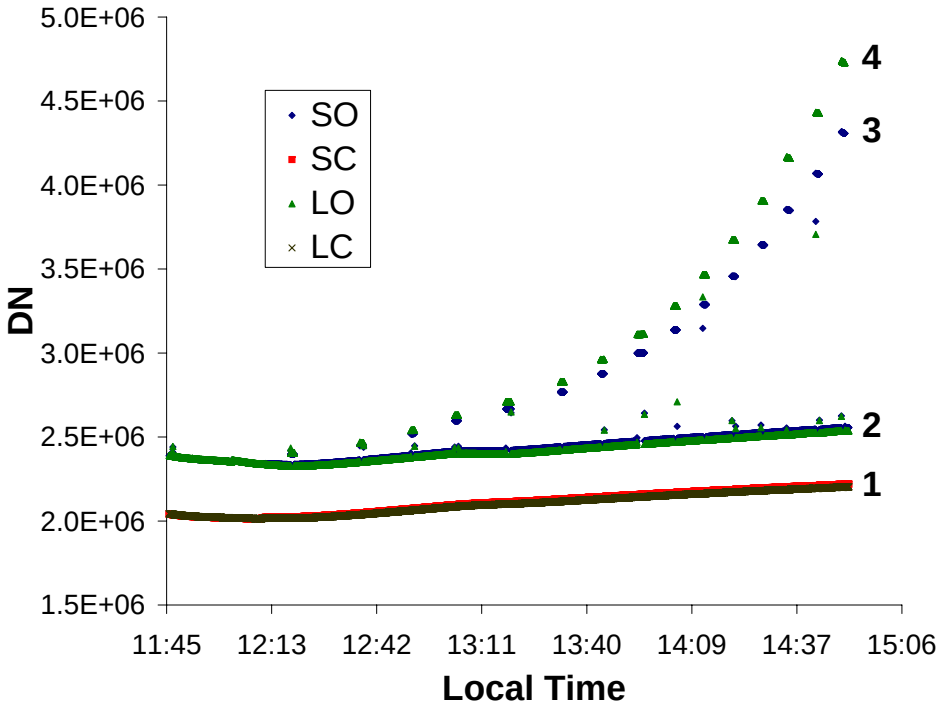

Figure 5.10: A typical data set gathered by MOPITT-A on October 12, 2004 for multiple external black body temperatures. The data states are determined by the LMC sector state and the chopper state and are shown as ShortOpen (blue), Short-Closed (red), LongOpen (green) and LongClosed (black). The curves represented by **1** are the chopper closed states, while curve **2** is the chopper open, black body shutter closed, and curves **3** and **4** are the chopper open, shutter open for the two LMC states.

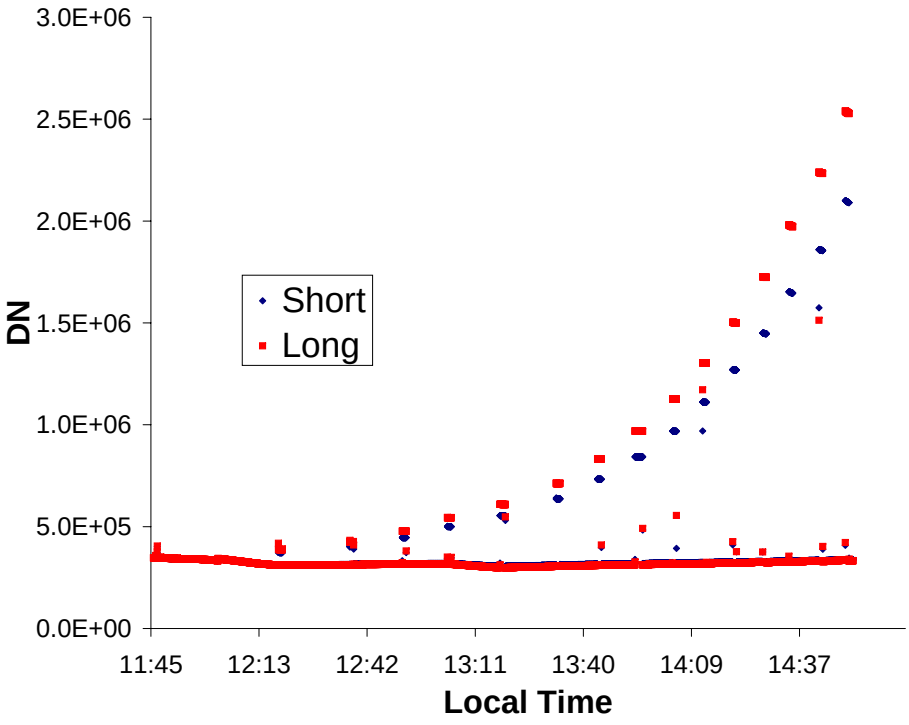

Figure 5.11: A typical data set of the Short (blue) and Long (red) states determined through subtraction of the data states with similar LMC states seen in Figure 5.10.

understood.

A single measurement of the difference signal at each temperature setting of the external black body was generated by averaging the entire set of data points collected at that temperature with the external black body shutter open. A corresponding difference signal was generated for the closed shutter position of the external black body by averaging one minute of closed shutter data, collected immediately after the shutter was closed. A corrected difference signal was generated by subtracting the closed shutter difference signal from the open shutter difference signal at each temperature setting. The three difference signals for the typical data set are shown in Figure 5.13.

5.4.1 Error Analysis

The error on the raw numbers output from the MOPITT-A is a combination of several effects: the voltage output from the detectors is a linear function of radiance incident upon the detector, the quantum efficiency, the voltage fed into the A/D convertors is a function of the electronic design and finally the number returned

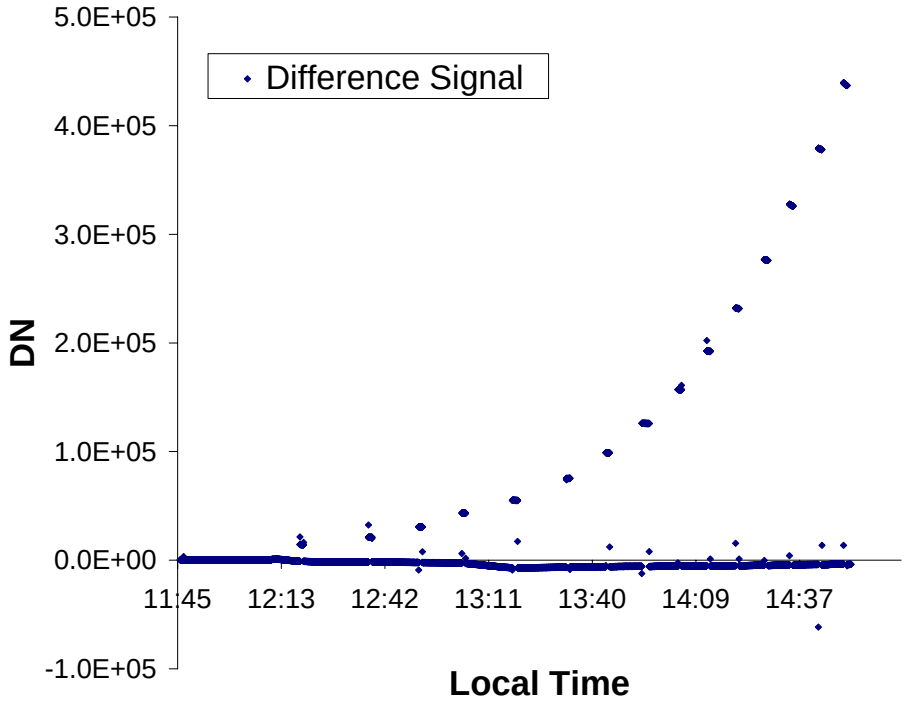

Figure 5.12: A typical data set of the Difference signal determined through subtraction of the states seen in Figure 5.11.

from MOPITT-A is, itself, an average of several individual samples quickly collected by the A-D sub-system and co-added. In principle, it would be possible to evaluate all of these terms and derive a theoretical error estimate for each raw measurement. In practice, it is sufficient look at the fluctuations of the raw data while looking at a steady source under under constant observing conditions.

A high resolution time series of raw data points from the MOPITT-A instruments are shown in Figure 5.14, which were collected over a 52 second period while the instrument was looking at the external black body at a temperature of 325 C. All the data points correspond to both the external black body shutter and MOPITT-A chopper in the open position. It can be seen that the raw signal varies from a minimum of 423869 DN to a maximum of 424161 DN, a spread of 292 DN. The standard deviation of the data points is 124.4 DN, corresponding to 0.03% of the average value.

A typical variation of the raw signal percentage error with external black body temperature is shown in Figure 5.15. Generally, the error tends to increase with increasing external black body temperature. A conservative estimate of the error in

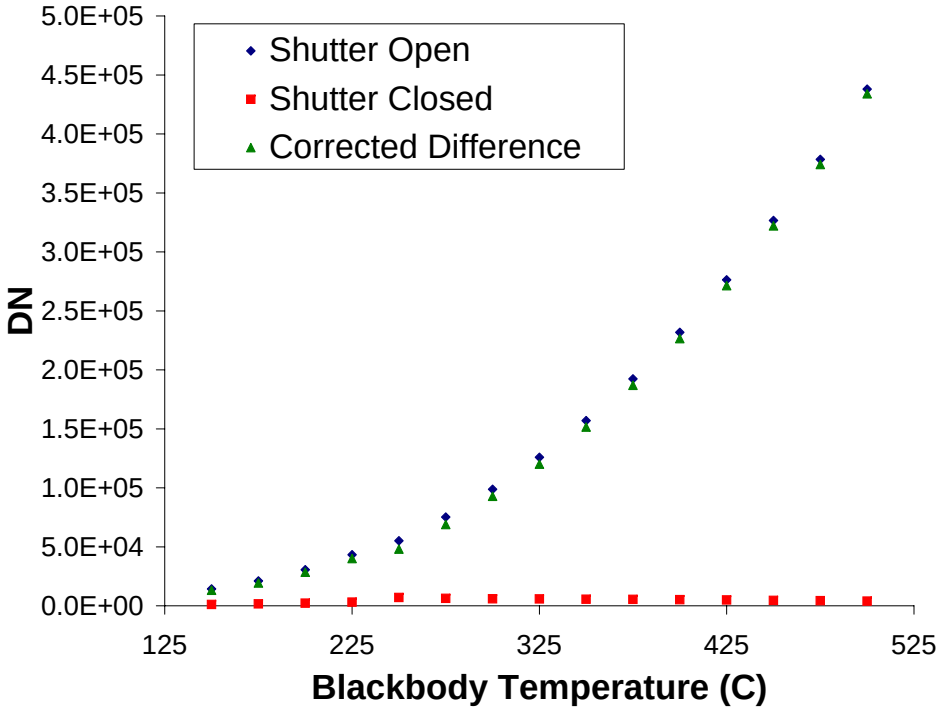

Figure 5.13: The averaged Difference signal with the black body shutter open data in blue and the shutter closed data in red. The subtraction of these data sets results in the average, background corrected Difference signal (green).

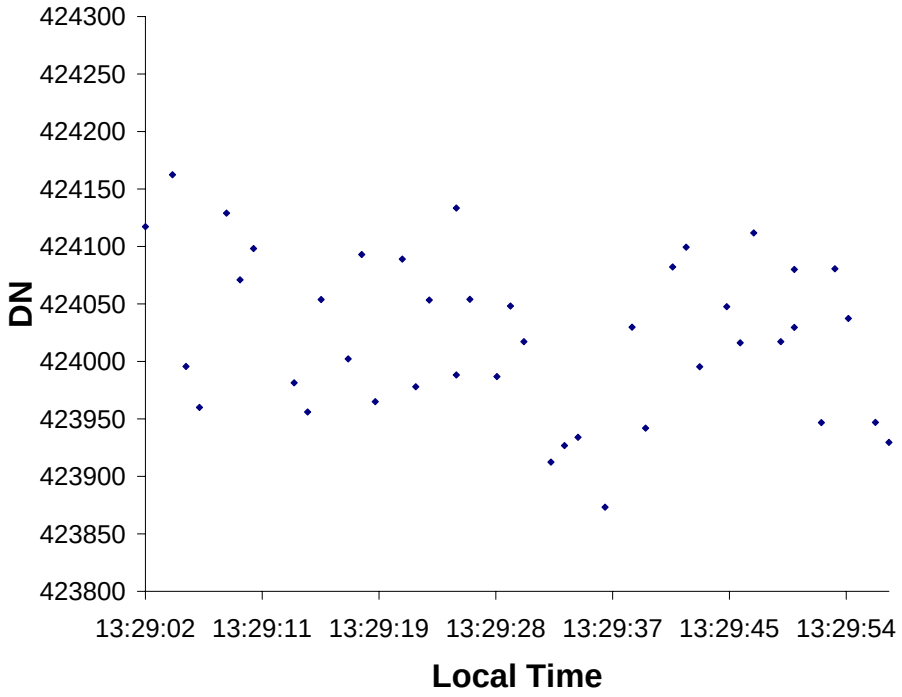

Figure 5.14: A typical measurement set of one black body temperature with the external black body shutter and optical chopper open.

any one measurement is 0.16%. It is a simple matter to evaluate the error on the corrected difference signal, described above, as it is generated from the subtraction of 8 raw signals. Consequently the error in the corrected difference signal, as given by standard error propagation, is $\sqrt{8} \times 0.16 = 0.45\%$. An error of 0.45% has been assigned to all of the corrected difference signal measurements.

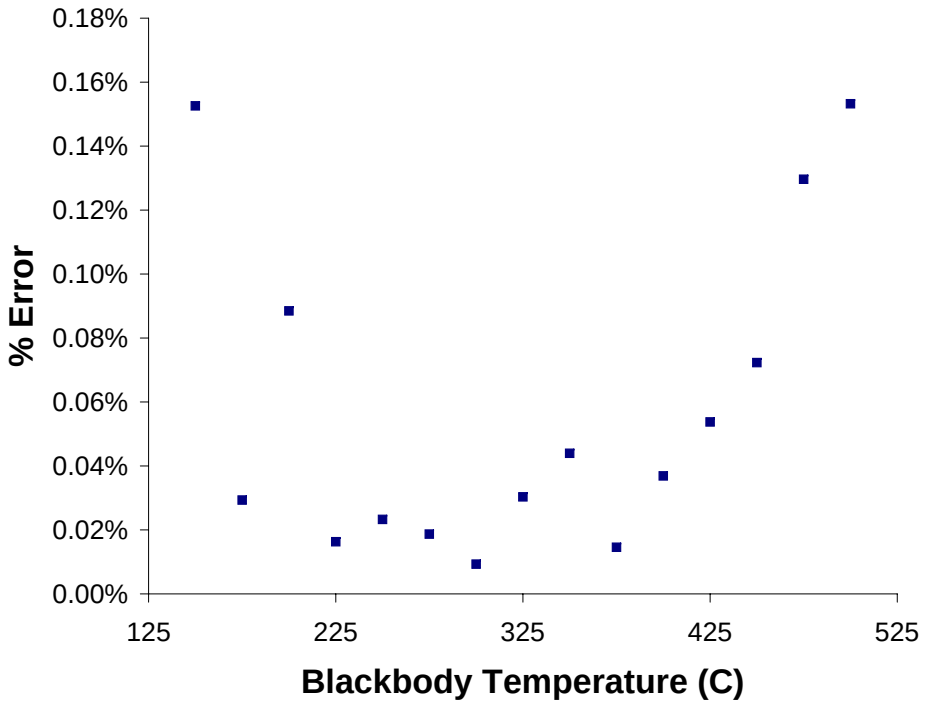

Figure 5.15: Typical percent errors in the average measured DN over a range of input temperatures.

Chapter 6

Calibration of MOPITT-A

6.1 Introduction

It has been shown in Chapter 4 that the raw signals measured by MOPITT-A can be reduced to a *long path* signal, L, a *short path* signal, S, and a difference signal, D. Theoretical consideration of the instrument allowed three equations to be developed that gave L, S and D as integrals of the incoming radiance, $I(\nu)$, the passband filter, $f(\nu)$ and the effective LMC gas-cell transmissions, $F_L(\nu)$, $F_S(\nu)$ and $F_D(\nu)$. This is seen in equations 4.7 to 4.9. In this section, the validity of this theoretical model is tested using controlled laboratory conditions.

6.2 Measurement of MOPITT-A Gain

The gain of the MOPITT-A instrument is defined as the constant, k, in equations 4.7 to 4.9. For convenience, the equation for the *long path* signal, L, is repeated here,

$$L = k \int_{\nu} I(\nu) f(\nu) F_L(\nu)\, d\nu. \tag{6.1}$$

It is additionally noted that the equations for S and D have a similar form. If there is no absorbing gas in the LMC gas-cell then F_L and F_S are unity at all wavenumbers while F_D is zero everywhere. Under these conditions we can write,

$$L = k \int_{\nu} I(\nu) f(\nu)\, d\nu. \tag{6.2}$$

When the external black body shutter is open the radiation incident upon MOPITT-A is a combination of the black body radiation $I_{BB}(\nu)$ and the ambient room radiation, $I_{amb}(\nu)$. When the external black body shutter is closed the incident radiation

is only $I_{amb}(\nu)$. Hence,

$$L_{open} = k \int_{\nu} [I_{BB}(\nu) + I_{amb}(\nu)] f(\nu)\, d\nu \tag{6.3}$$

$$L_{closed} = k \int_{\nu} [0 + I_{amb}(\nu)] f(\nu)\, d\nu \tag{6.4}$$

$$\Delta L = L_{open} - L_{closed} = k \int_{\nu} I_{BB}(\nu) f(\nu)\, d\nu, \tag{6.5}$$

where L_{open} is the *long path* signal with the external black body shutter open and L_{closed} is the *long path* signal with the shutter closed and ΔL is the difference between the two. The intensity of radiation exiting the external black body, I_{BB}, at any specific wavenumber is readily calculated for a given temperature using the Planck function while the transmission of the pass-band filter, $f(\nu)$, has been measured. Therefore equation 6.5 can be rewritten as,

$$\Delta L = kR(T), \tag{6.6}$$

where

$$R(T) = \int_{\nu} I_{BB}(\nu, T) f(\nu)\, d\nu. \tag{6.7}$$

The function $R(T)$ is only a function of temperature and can be evaluated numerically using high resolution trapezoidal integration across the passband filter, $f(\nu)$. Equation 6.6 indicates that there should be a straight line relationship between ΔL and $R(T)$ with the MOPITT-A gain, k, as the gradient of the line. This equation provides the basis for measurement and validation of the MOPITT-A gain.

The LMC gas-cell was purged with nitrogen gas and evacuated using the roughing pump, guaranteeing that the cell contained no absorbing gas. The external gas-cell was left at atmospheric pressure and was assumed to contain insignificant amounts of CO. The external black body was aligned with the center of pixel 1 of channel 5. Measurements were acquired as the external black body was slowly stepped from 150 C to 500 C in increments of 25 C. The external black body was allowed sufficient time, of approximately 15 minutes, to stabilize at each temperature setting before the shutter was opened and measurements acquired for approximately 1 minute. Closed shutter measurements were acquired at all other times. The entire process required about 3-4 hours to measure one curve, most of which was spent waiting for the external black body to stabilize. The MOPITT-A raw signals were processed, as outlined in Section 5, to produce *long path*, L, and *short path*, S, signals. The ΔL signals were generated from the L signals by subtracting the closed shutter

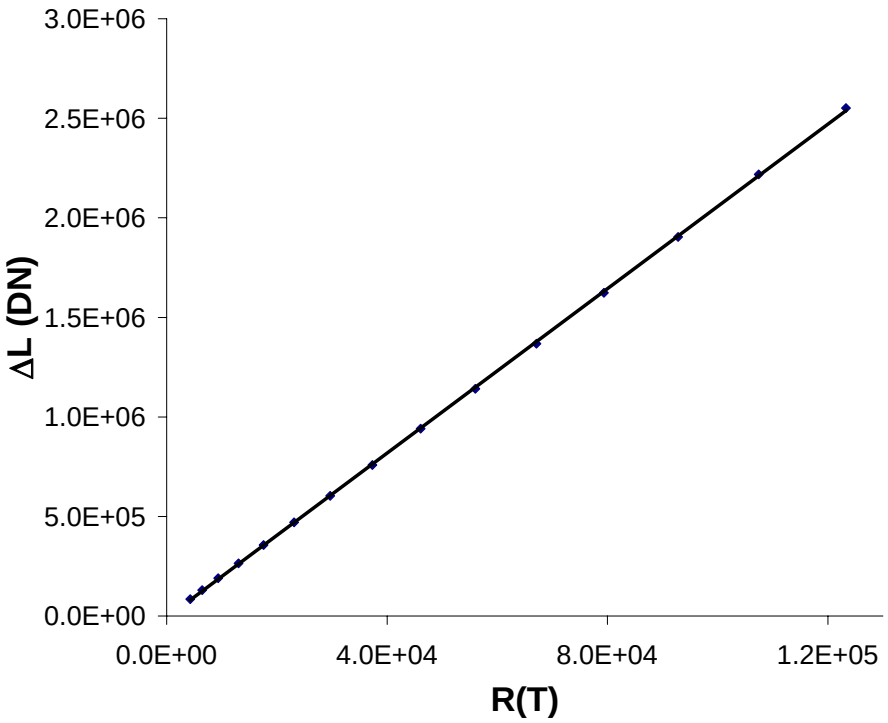

Figure 6.1: MOPITT-A observed data (Δ L)plotted against the modelled output (R(T)). The gradient of the linear fit represents the system gain, k.

measurements from the open shutter measurements. A typical plot of measured ΔL against $R(T)$ is shown in Figure 6.1. A least-squares fit of a straight line to the data, which is also shown in Figure 6.1, produces a gradient, k, of 20.654 and a y-intercept of -8092.9. Clearly, the straight line fit is in good agreement with the measurements. Thus, the theoretical description of the instrument for conditions when there is no absorbing gas in the LMC or external gas-cell, equation 6.6, appears to be satisfactory.

The same data points are shown in Figure 6.2 where the best fit, straight line trend has been removed from the measurements. This reveals a small systematic variation on the order of 1% of the total signal which is slightly larger than the error on the measurements. The source of this systematic variation is unknown but might be due to small residual errors in the external black body design and operation as well as small, time-dependent, variations in the MOPITT-A instrument. For example, the external black body may not be as stable at higher temperatures.

The de-trended graph clearly identifies one region to the left of the minimum and another to the right where the gradient is noticeably different. This variation in

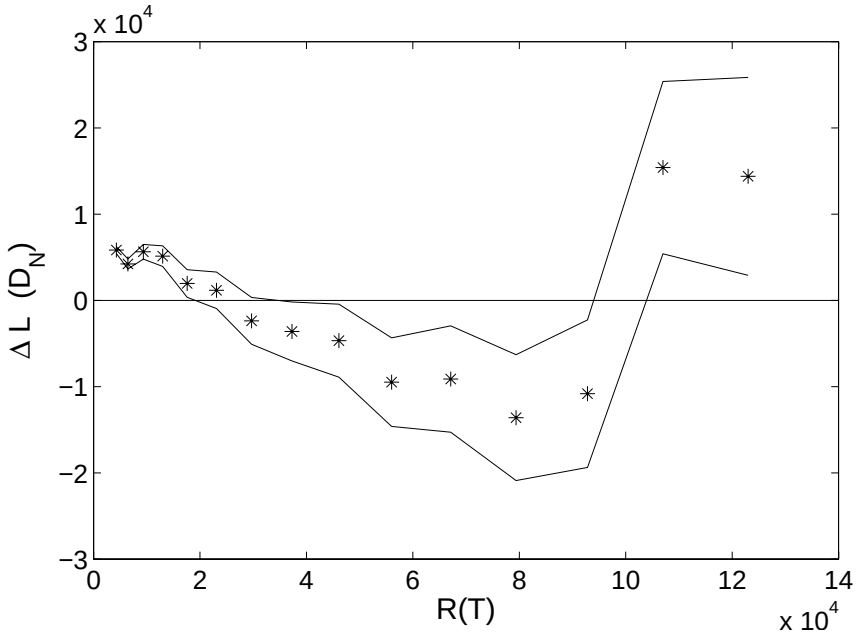

Figure 6.2: The variability of the MOPITT-A gain around a least-squares linear fit, along with the corresponding point errors.

gradient has been used to estimate the true error in the estimate of the gradient, k, by fitting one straight line to the first seven data points and another straight line to the last 6 data points. The first curve yielded a slope of 20.373 while the seconded gave a slope of slope of 20.848, a difference in slope of 0.475. If is is assumed this represents the maximal range in gradient value then the error in the nominal gradient is half of this value. Therefore, it is concluded that the value of gain, k, derived from this experiment was 20.654 ± 0.237.

This procedure was repeated again a few days later and resulted in a gain value of 20.414 ± 0.229, a change of 1.1% which is just within the error bars of the previous measurement. While this seems to suggest that the MOPITT-A gain is relatively stable, other measurements presented in later sections suggest otherwise. Consequently, a suitable calibration plan for MOPITT-A would include the measurements presented in this section to measure the instrument gain, k, in isolation from other artifacts.

6.3 Instrument Response with CO in LMC

In the previous section we developed and tested a theory of the MOPITT-A instrument with no gas in either the LMC or external gas-cell. In this section we introduce CO gas into the LMC and test the instrument theory under these new conditions. Inserting an absorbing gas into the LMC, differentiates the *long path* signal from the *short path* signal and the difference signal, D, is no longer zero. This can be seen mathematically in equation 4.9, which is repeated here,

$$D = k \int_{\nu} I(\nu) f(\nu) F_D(\nu)\, d\nu, \tag{6.8}$$

where the difference filter, $F_D(\nu)$, as given by equation 4.12, is

$$F_D(\nu) = e^{-\tau_S(\nu)} - e^{-\tau_L(\nu)}. \tag{6.9}$$

A new set of measurements were collected in similar manner to those from the previous section. The external black body was located at the center of pixel 1. The external gas-cell was filled with air at atmospheric pressure and assumed to be devoid of absorbing gas. The LMC was initially purged with nitrogen to scrub any residual gases and promptly filled with CO to the required pressure. For each pressure setting in the LMC, the external black body was stepped from 150 C to 500 C in 25 C increments. After the external black body temperature had stabilized, MOPITT-A measurements were collected for one minute with the external black body shutter open. All other measurements were made with the external black body shutter closed. The corrected difference signal, D, was created using the data reduction scheme described in Chapter 5. The pressure in the LMC was monitored with the calibrated pressure transducer while the temperature of the LMC was monitored with a MOPITT-A housekeeping thermistor. The CO pressure in the LMC was stepped from 40 kPa to 80 kPa in 10 kPa increments, resulting in 5 discrete data sets.

The optical depths, τ_S and τ_L in equation 6.9, were determined using the measured LMC temperature and pressure as well as the known LMC cell geometry and CO molecular absorption cross-sections. The temperature and pressure were combined via the ideal gas-law to give the molecular number density in the cell. The molecular absorption cross-sections were taken from the HITRAN database and combined with the pressure and temperature information to yield line-broadened spectra. The cell-geometry was known from the instrument design. Consequently,

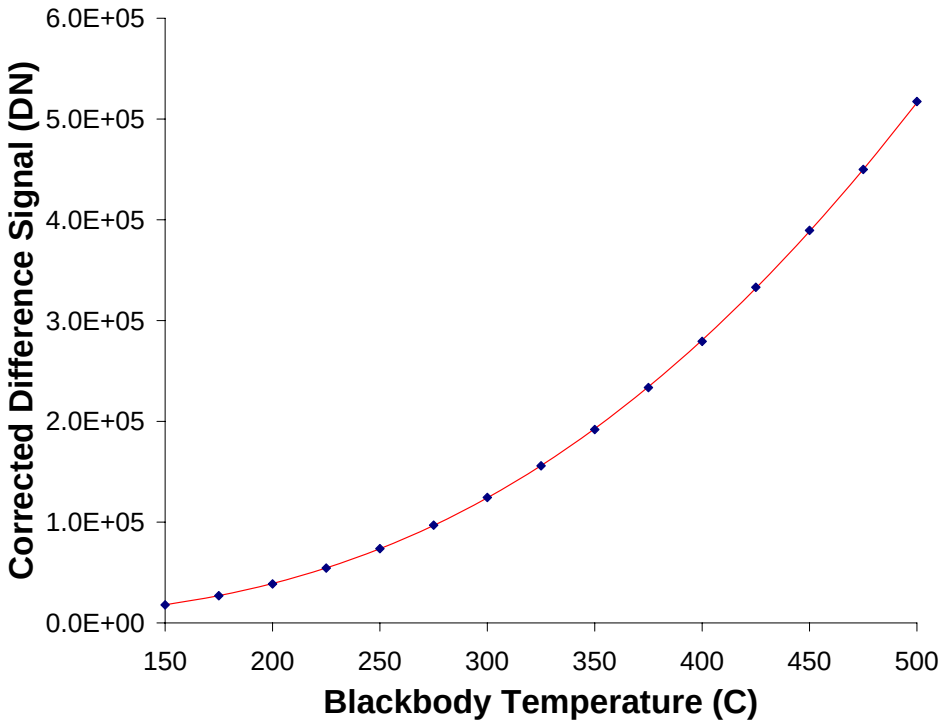

Figure 6.3: The variation of the corrected difference signal, D (blue), with temperature as measured by MOPITT-A on October 13, 2004. The LMC pressure was 70 kPa. The solid line shows the best fit curve derived with an instrument gain of 21.608 and an LMC pressure of 70.0 kPa.

it was possible to evaluate $F_D(\nu)$ for a given LMC pressure and temperature at any wavenumber.

The theoretical value for the corrected difference signal was derived by numerically integrating equation 6.8 across the bandpass filter using high resolution trapezoidal integration. It was quickly determined that good agreement between measurements and modelled results could not be achieved unless the value of instrument gain, k, was fitted to each set of temperature scan measurements. It was also found that a significantly better fit, in a least-squares sense, could be achieved by slight modification of the pressure value used in the LMC. Consequently, an algorithm was built to search the parameter space of instrument gain, k and LMC pressure, p, for the best least squares fit of the theoretical model to the corrected difference signal. The pressure transducer reading was taken as the initial estimate of the LMC pressure for the search algorithm while the initial estimate of instrument gain was the average value of the measured corrected difference signal divided by the integral in equation 6.8.

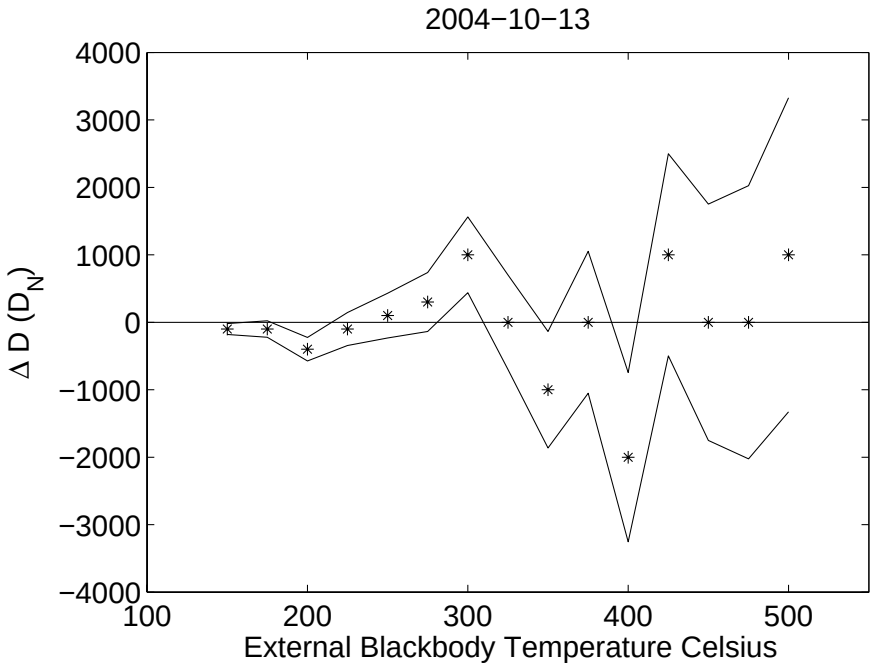

Figure 6.4: The MOPITT-A instrument response residual with corresponding error from the data set measured on October 13, 2004.

A typical example of a measured, corrected difference curve is shown in Figure 6.3 together with the least squares fitted curve. It is readily apparent that the fitted curve is in excellent agreement with the measurements. This is confirmed when the residuals of the measurements of the curve are compared to the measurement error bars, seen in Figure 6.4. The majority of the measurement points are within one error bar from the fitted curve, suggesting that the fit is free from systematic error. In reality, minor systematic errors exist in the measurement of the MOPITT-A state parameters such as LMC pressure, temperature and instrument gain as well as the HITRAN absorption cross-sections. However, it appears that all of these minor systematic effects, which are difficult to quantify, can be adjusted for by searching the least-squares space for the best fit parameters.

The above least squares algorithm was applied to all five sets of corrected difference signals, collected for different pressures of CO in the LMC gas-cell. A summary of the results is shown in Table 6.1. The results show that the LMC pressure occasionally required minor adjustment by the least squares algorithm, on the order of 0.5 kPa, but frequently required no modification at all, suggesting that the pressure transducer and other instrument state measurements were well calibrated. On the other hand, the instrument gain shows considerable fluctuation varying from 20.787

Date	Parameter	Initial Value	Fitted Value
2004/10/12	LMC Pres	60.0	60.5
	Gain	21.321	20.821
2004/10/13	LMC Pres	70.0	70.0
	Gain	21.808	21.608
2004/10/14	LMC Pres	40.0	40.0
	Gain	22.048	21.548
2004/11/22	LMC Pres	50.0	50.0
	Gain	21.187	20.787
2004/11/23	LMC Pres	80.0	79.0
	Gain	22.183	22.283

Table 6.1: Measured and modelled results for the MOPITT-A instrument response experiments.

to 22.283, corresponding to a 7.2% variation.

The exact cause of this variation has not been fully diagnosed but it is suspected that ice buildup on the detector surface may be playing a significant role. Curiously, the instrument gain appears to be stable during any particular set of measurements, each lasting 3 to 4 hours in duration, but shows significant variation from one day to the next. This may be due, in part, to the fact that the detector nest was always evacuated with the pumping station prior to each experiment, thus changing the conditions in the nest from one experiment to the next. At the current time more work would be required to fully diagnose this situation.

In this section we have shown that it is possible to accurately model the behavior of the MOPITT-A instrument when the LMC gas-cell is filled with an absorbing gas and the front aperture is illuminated with a black body source. It has been shown that an algorithm that searches the least squares space can readily find parameters for instrument gain and LMC pressure that provide an accurate description of the actual measurements.

6.4 Instrument Response with a Simulated Atmospheric Signal

The previous two sections have shown that the theoretical model of the MOPITT-A instrument can successfully predict and calibrate the measured response of the instrument when it is illuminated with a black body source. While these measurements are sufficient for calibration purposes, it is interesting to extend the measurement set and investigate the accuracy of the model when the instrument is illuminated, not with a black body source, but a simulated, atmospheric CO absorption signal.

The simulated atmospheric signal was generated by passing black body radiation through the external gas-cell which was filled with CO at selected pressures. The CO gas in the external gas-cell imposed absorption features onto the spectrum before entering the MOPITT-A, effectively simulating an atmospheric signal. Four pressures of pure CO in the external gas-cell were investigated, 20 kPa, 40 kPa, 60 kPa, and 80 kPa. The MOPITT-A corrected difference signal, D, was measured as a function of black body temperature for each pressure setting in the external gas-cell by stepping the black body temperature from 200 C to 500 C in steps of 100 C. The LMC was purged with nitrogen, evacuated and promptly filled with CO to a pressure of 80 kPa which was chosen to simulate observations probing the lower troposphere.

Theoretical modelling of the difference signal, D, still required numerical integration of equation 6.8. However, the radiation incident upon the instrument aperture, $I(\nu)$, was no longer a pure black body Planck function, as used in earlier sections, but a Planck function propagated through a homogeneous, absorbing layer, as described in equation 3.13. The optical depth of the external gas-cell filled with CO was readily computed using the physical dimensions of the cell, the measured pressure and temperature and the HITRAN absorption cross-section database.

Similar to the previous section, it was found that the fit could be significantly improved if the least squares space was searched for optimal parameters. In this case there were three parameters to search: instrument gain, LMC pressure and external gas-cell pressure. However, it was found sufficient to hold the pressure of the LMC fixed at 80 kPa and only search the least squares space for instrument gain, k, and external gas-cell pressure.

The four curves of instrument response to simulated atmospheric signal are shown in Figure 6.5. It is seen that the corrected difference signal systematically decreases

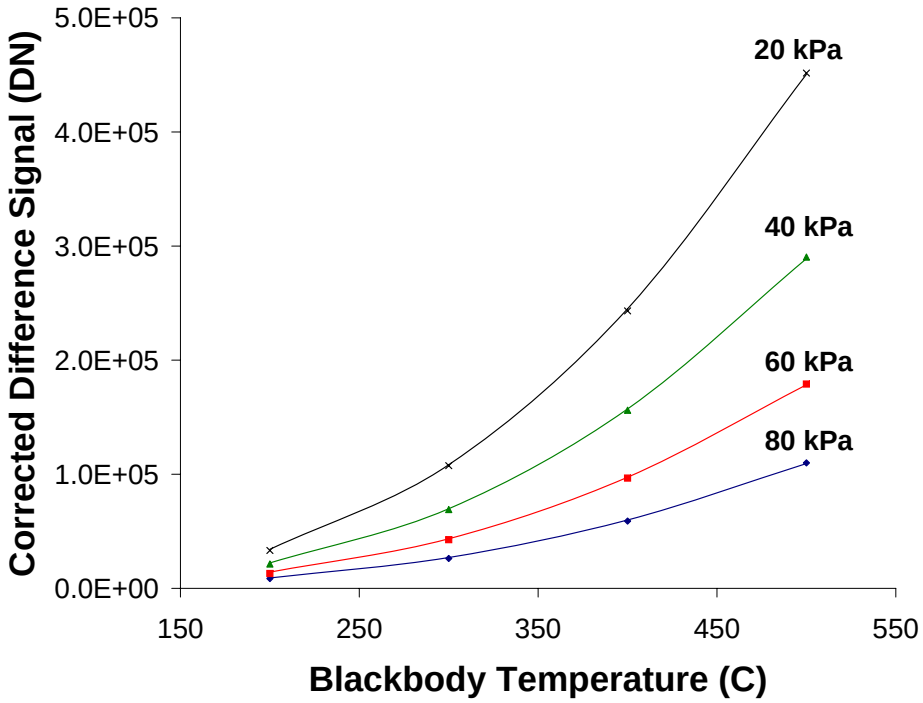

Figure 6.5: The MOPITT-A response to simulated atmospheric signals. The variation of corrected difference signal with black body temperature is shown for 4 different pressures of pure CO in the external gas-cell. The markers indicate the measured difference signal while the solid lines indicate the modelled instrument response.

as the pressure of CO in the external gas-cell is increased. This is consistent with the external gas-cell being cooler than the hot black body source and absorbing radiation from the beam. The fitted, modelled signal is also shown and is seen to be in good agreement. The fitted values of instrument gain and external gas-cell pressure for each curve are tabulated in Table 6.2.

Similar to the previous section, it can be seen that the fitted value of pressure is quite close to the measured value while the instrument gain shows considerable variation from data set to data set. However, the instrument model does seem to provide an accurate description of the instrument as long as the proper values for gain and pressure are used.

Date	**Parameter**	**Initial Value**	**Fitted Value**
2004/11/29	EGC Pres	80.0	80.0
	Gain	25.748	25.448
2004/11/30 01	EGC Pres	60.0	61.0
	Gain	24.735	25.135
2004/11/30 02	EGC Pres	40.0	39.5
	Gain	23.862	23.362
2004/11/30 03	EGC Pres	20.0	20.0
	Gain	22.631	22.531

Table 6.2: Measured and modelled results for the MOPITT-A atmospheric response experiments.

Chapter 7

Summary and Conclusions

7.1 Summary of Present Work

This work has shown that controlled laboratory measurements collected by the MOPITT-A instrument are consistent with a theoretical model, as long as a few key instrument parameters are adjusted to fit the data. This verifies that the MOPITT-A instrument continues to work within acceptable operational limits and indicates that constant calibration of the system is an essential component of routine operations.

The theoretical model was developed by combining the theories of radiative transfer and correlation spectroscopy. Radiative transfer theory was used to calculate the propagation, absorption and emission of light through the atmosphere, or in the case of the laboratory setup, an external gas-cell. A single layer model, suitable for the external gas-cell or small atmospheric altitude range, was developed by application of Beer's Law, the principle of detailed balance and the Schwarzschild equation. The propagation of signal through an extended altitude range was modelled by stacking multiple single layers in succession to mimic a multiple layer atmosphere. The hot surface of the Earth was used as the initial light source when modelling atmospheric signal while the temperature of an external black body was used when modelling the laboratory conditions.

The theory of correlation spectroscopy was developed and it was shown that the raw MOPITT-A measurements could be split into long path and short path signals. This allowed a difference signal to be determined which was related to the magnitude of CO spectral signature in the incoming atmospheric signal. Controlled laboratory measurements were made using an external gas-cell to emulate the atmospheric signal

and an external black body as a controlled light source. The inferred difference signals were in excellent agreement with theory as long as we adjusted the MOPITT-A gain for a good fit. Acquisition of high quality, difference signals required careful analysis of the raw data collected for different LMC gas cell states, optical chopper states and black-body shutter states.

A controlled laboratory environment was constructed to ensure that specific measurement conditions were repeatable. A custom table was built for the external black body that permitted precise movement in both the horizontal and vertical directions. Mounting brackets were constructed for both the external gas-cell and external mirror, ensuring precise positioning of these items. The pressure transducer, used to measure the pressure in various components within the system, was calibrated using a mercury manometer, which provided pressure measurements considerably more accurate than the manufacturer's calibration curve. The instrument's field of view was mapped out and the black body precisely placed at the centre of one of the detector's pixels. The gain of the MOPITT-A system was inferred from several sets of measurements which were collected after all absorbing gases (CO) had been removed from both the external gas-cell and LMC. Each set of measurements were in good agreement with the theoretical model and allowed a precise measurement of the instrument gain. Curiously, the inferred MOPITT-A gain changed value between different sets of measurements but was constant during any given set, as implied by the good agreement with theory.

The performance of the MOPITT-A instrument under operational conditions was evaluated using the external black body as a light source and the external gas-cell to simulate atmospheric absorption. Again there was very good agreement between the MOPITT-A measurements and the theoretical model, as long as the gain of the instrument used in the theoretical model was allowed to vary from one set of measurements to another. The pressure employed in the least squares fit was also allowed to vary but this normally required very minor correction and usually returned a result very close to the pressure transducer reading.

It was readily apparent that the MOPITT-A instrument was consistent with the theoretical model but the gain of the system detector varied from one set of measurements to another. The source of the gain variation was not identified and is left as a task for future work. At the current time it is suspected that the variation of gain may be due to frosting on the detector's front surface. The variation in gain due

to this phenomenon would be attributed to the fact that the detector nest was always evacuated with the rouging pump prior to any given set of measurements, inherently changing the conditions within the nest. Frosting effects were also suggested by the SAFARI campaign team as a possible source of signal contamination. It is noted that the gain appears to be constant for any given set of measurements. If it was not constant then we could not get good agreement between theory and measurement. This probably excludes the notion of gain variation due to variability of the pre-amps and A/D system as these components would have no inherent synchronization with the different sets of measurements.

7.2 Recommendations for Future Works

The largest issue found while evaluating the MOPITT-A performance was the variability of the detector gain. Therefore, an in-depth analysis to determine the cause of the variability in the gain is recommended. Hopefully, this study would both determine the cause and offer a solution to the variability. In the meanwhile, it is absolutely essential that the MOPITT-A gain be constantly monitored during any operational measurements. This should be possible using the three internal BOMEM black bodies as long as it can be ensured that they are stable, a significant issue during the SAFARI campaign. It is also recommended that the external gas-cell and black body be used both before and after a set of measurements to validate the instrument gain.

One of the major drawbacks associated with the data gathering completed in this thesis was the large amount of time required for the external black-body to stabilize at each temperature. The ability to rapidly change between several known, fixed radiances would decrease the acquisition time of one set of measurements from several hours to a few minutes. In addition, it is recommended that a pressure transducer be supplied exclusively for the LMC. This would provide continuous pressure measurement during data gathering, which would permit more accurate modelling and diagnostics.

References

Andreae, Meinrat O., Fishman, Jack, Lindesay, Janette: The Southern Tropical Atlantic Region Experiment (STARE): Transport and Atmospheric Chemistry near the Equator-Atlantic (TRACE A) and Southern African Fire-Atmosphere Research Initiative (SAFARI): An introduction, *Journal of Geophysical Research*, **101**, D19, 23519, 1996.

Bailak, George V., Davis, Gary R., Drummond, James R., Jounot, Loic, Mand, Gurpreet, Philips, Andre, Tolton, Boyd T.: MOPITT airborne validation instrument: MOPITT-A, Department of Physics, University of Toronto, Toronto, Canada, 1999 http://www.atmosp.physics.utoronto.ca/MOPITT/MOPmorePublications.htm.

Bowman, Kenneth P.: Transport of carbon monoxide from the tropics to the extratropics, *Journal of Geophysical Research*, **111**, D02107, 2006.

Chamberlain, Joseph W., Hunten, Donald M.: Theory of Planetary Atmospheres An Introduction to Their Physics and Chemistry Second Edition, Academic Press Inc., 1987.

Drummond, James R.: The Engineering Qualification Model (EQM) Signal Processing Module (SPM), Department of Physics, University of Toronto, Toronto, Canada, 2000.
http://www.atmosp.physics.utoronto.ca/MOPITT/MOPmorePublications.htm.

Drummond, James R., Abbatt, Jonathan, Degenstein, Doug, Edwards, David, Gille, John, Hackett, John, McConnell, Jack, Michelangeli, Diane, Menard, Richard, Shepherd, Ted, Strong, Kimberly: The Successor To Measurements of Pollution In The Troposphere MOPITT-2, Department of Physics, University of Toronto, Toronto, Canada, 2003.
http://www.atmosp.physics.utoronto.ca/MOPITT/MOPmorePublications.htm.

Drummond, J.R., Brasseur, G.P., Davis, G.R., Gille, J.C., McConnell, J.C., Peskett, G.D., Reichle, H.G. Jr., Roulet, N.: Measurement Of Pollution In The Troposphere (MOPITT) Mission Description Document, Department of Physics, University of Toronto, Toronto, Canada, 1993.
http://www.atmosp.physics.utoronto.ca/MOPITT/MOPmorePublications.htm.

Edwards, D.P., Emmons, L.K., Gille, J.C., Chu, A., Attié, J.-L., Giglio, L., Wood, S.W., Haywood, J., Deeter, M.N., Massie, S.T., Ziskin, D.C., Drummond, J.R.: Satellite-observed pollution from Southern Hemisphere biomass burning, *Journal of Geophysical Research*, **111**, D14312, 2006

Edwards, D.P., Halvorson, C.M., Gille, J.C.: Radiative transfer modeling for the EOS Terra satellite Measurement of Pollution in the Troposphere (MOPITT) instrument, *Journal of Geophysical Research*, **104**, D14, 16755, 1999.

Edwards, D.P., Petron, G., Novelli, P.C., Emmons, L.K., Gille, J.C., Drummond, J.R.: Southern Hemisphere carbon monoxide interannual variability observed by Terra/Measurement of Pollution in the Troposphere (MOPITT), *Journal of Geophysical Research*, **111** D16303, 2006

Fleagle, Robert G., Businger, Joost A.: An Introduction to Atmospheric Physics Second Edition, Academic Press Inc., 1980.

Francis, G.L., Edwards, D.P., Gille, J.C.: Channel radiance calculations for MOPITT forward modeling and operational retrievals, Department of Physics, University of Toronto, Toronto, Canada, 1999,
http://www.atmosp.physics.utoronto.ca/MOPITT/MOPmorePublications.htm.

Hanel, R.A., Conrath, B.J., Jennings, D.E., Samuelson, R.E.: Exploration of the Solar System by infrared remote sensing, Cambridge University Press, 1992.

Holloway, Tracey, Levy, Hiram II, Kasibhatla, Prasad: Global distribution of carbon monoxide, *Journal of Geophysical Research*, **105**, 12123, 2000.

Houghton, J.T.: Climate Change, Cambridge University Press, 1992.

Houghton, J., Smith, S.D.: Infra-red Physics, Oxford University Press, 1966.

Hyer, Edward J., Kasischke, Eric S., Allen, Dale J.: Effects of source temporal resolution on transport simulations of boreal fire emissions, *Journal of Geophysical Research*, **112**, D01302, 2007.

Janssen, Micheal A.: Atmospheric Remote Sensing By Microwave Radiometry, John Wiley and Sons Inc., 1993.

Jounot, Loic J., Drummond, James R.: Measurement of Pollution In The Troposphere - Aircraft (MOPITT-A). IEEE International Geoscience and Remote Sensing Symposium, 2002.

Lamarque, J.-F., Edwards, D.P., Emmons, L.K., Gille, J.C., Wilhelmi, O., Gerbig, C., Prevedel, D., Deeter, M.N., Warner, J., Ziskin, D.C., Khattatov, B., Francis, G.L., Yudin, V., Ho, S., Mao, D., Chen, J., Drummond, J.R.: Identification of CO plumes from MOPITT data: Application to the August 2000 Idaho-Montana forest

fires, *Geophysical Research Letters*, **30**, 13, 1688, 2003.

Mand, Gurpreet S., Bailak, George V., Yu, Zhen Z., Tolton, Boyd T., Mak, Nikolai N., Drummond, James R.: An Early Look At "Near Real" MOPITT Data, 1999, http://www.atmosp.physics.utoronto.ca/MOPITT/MOPmorePublications.htm.

Nichitiu, Florian, Drummond, James R., Zou, Jiansheng, Deschambault, Robert: Solar particle events seen by the MOPITT instrument, *Journal of Atmospheric and Solar-Terrestrial Physics*, **66**, 1797, 2004.

Picone, J.M., Hedin, A.E., Drob, D.P., Aikin, A.C.: NRLMSISE-00 empirical model of the atmosphere: Statistical comparisons and scientific issues, *Journal of Geophysical Research*, 107(A12), 1468, 2002.

Pradier, Stéphanie, Attié, Jean-Luc, Chong, Michel, Escobar, Juan, Peuch, Vincent-Henri, Lamarque, Jean-François, Khattatov, Boris, Edwards, David: Evaluation of 2001 springtime CO transport over West Africa using MOPITT CO measurements assimilated in a global chemistry transport model, *Tellus*, **58B**, 163, 2006.

Reif, F.: Fundamentals of Statistical and Thermal Dynamics, McGraw-Hill Book Company, 1965.

Rothman, L.S., Rinsland, C.P., Goldman, A., Massie, S.T., Edwards, J.-M., Perrin, A., Camy-Peyret, C., Dana, V., Mandin, J.-Y., Schroeder, J., McCann, A. Gamache, R.R., Wattson, R.B., Yoshino, K., Chance, K.V., Jucks, K.W., Brown, L.R., Nemtchinov, V., Varanasi, P.: The HITRAN Molecular Spectroscopic Database and HAWKS (HITRAN Atmospheric Workstation): 1996 Edition, *Journal of Quantitative Spectroscopy and Radiative Transfer*, **60**, 665-710, 1998.

Summers, M. E., Conway, R. R., Siskind, D. E., Stevens, M. H., Offerman, D., Riese, M., Preusse, P., Strobel, D. F., Russel, J. M. III: Implications of Satellite OH Observations for Middle Atmosphere H_2O and Ozone, *Science*, **277**, 1967, 1997.

Thompson, A. M.: The Oxidizing Capacity of the Earth's Atmosphere: Probable Past and Future Changes, *Science*, **256**, 1157, 1992.

Tolton, Boyd T., Drummond, James R.: Characterization of the Length-Modulated Radiometer, *Applied Optics*, **36**, 22, 5409, 1997.

Wang, Jinxue, Deeter, Merritt N., Gille, John C., Bailey, Paul L.: Retrieval of Tropospheric Carbon Monoxide Profiles from MOPITT: Algorithm Description and Retrieval Simulation, 1999,
http://www.atmosp.physics.utoronto.ca/MOPITT/MOPmorePublications.htm.

Young, Thomas: Photoelectomagnetic Effect in Bismuth, *Physical Review*, **117**, 5, 1244, 1960.

Yurganov, L.N., Duchatelet, P., Dzhola, A.V., Edwards, D.P., Hase, F., Kramer, I., Mahieu, E., Mellqvist, J., Notholt, J., Novelli, P.C., Rockmann, A., Scheel, H.E., Schneider, M., Schulz, A., Strandberg, A., Sussmann, R., Tonimoto, H., Velazco, V., Drummond, J.R., Gille, J.C.: Increased Northern Hemispheric carbon monoxide burden in the troposphere in 2002 and 2003 detected from the ground and from space, *Atmospheric Chemistry and Physics*, **5**, 563, 2005.